Friedrich-Schiller-Universität Jena
Physikalisch-Astronomische Fakultät
Thüringer Landessternwarte Tautenburg

Diffuse Radio Emission at Low Frequencies in Merging Galaxy Clusters

Dissertation

zur Erlangung des akademischen Grades
Doctor rerum naturalium (Dr. rer. nat.)

vorgelegt dem Rat der Physikalisch-Astronomischen Fakultät
der Friedrich-Schiller-Universtität Jena

eingereicht von **Dipl.-Phys. Alexander Drabent**
geboren am 02.11.1986 in Leinefelde

Name: Alexander Drabent
Geboren: 02. November 1986 in Leinefelde
Matrikelnummer: 90192

1. Gutachter: Prof. Dr. Artie Hatzes
Thüringer Landessternwarte Tautenburg
2. Gutachter: Prof. Dr. Matthias Kadler
Universität Würzburg
3. Gutachter: apl. Prof. Dr. Katharina Schreyer
Friedrich-Schiller-Universität Jena

Tag der Disputation: 20. April 2017

Meinem Sonnenschein

Zusammenfassung

Ausgedehnte diffuse Radioquellen, sogenannte Radiohalos, Radiorelikte und Radiominihalos sind bisher in ungefähr 100 Galaxienhaufen bekannt. Diese Radioquellen werden durch Synchrotronstrahlung der relativistischen Elektronen im Magnetfeld des Haufengases verursacht. Über die Beschleunigungsmechanismen der Elektronen auf relativistische Energien ist nur wenig bekannt. Beobachtungen bei niedrigen Radiofrequenzen ermöglichen es, Rückschlüsse auf die Verteilung der bereits gealterten relativistischen Elektronen zu ziehen. Dies erlaubt Einblicke in die Herkunft relativistischer Elektronen im Haufengas und ihrer Rolle in der Entwicklungsgeschichte von Galaxienhaufen. In dieser Arbeit wurden zehn Galaxienhaufen, bei denen sowohl klassifizierte als auch nicht klassifizierte diffuse Radioquellen bekannt sind, im Rahmen des WSRT 346 MHz Legacy Surveys, untersucht. Mit der Himmelsdurchmusterung konten in den Galaxienhaufen drei Radiorelikte und fünf Radiohalos bestätigt werden. In einem Galaxienhaufen wurde der Radioreliktkandidat als Radiogalaxie klassifiziert. Desweiteren wurde bisher unklassifizierte diffuse Radioemission mit bemerkenswerter Morphologie in Abell 2069 entdeckt.

Abell 2069 ist ein Galaxienhaufen, der aus zwei Komponenten besteht, die im Röntgenbereich ein jeweils eigenes Helligkeitsmaximum zeigen. In der Hauptkomponente des Galaxienhaufens ist ein Radiohalo sichtbar, während die zweite Teilkomponente eine ausgedehnte Radioemission unbekannten Ursprungs mit sehr steilem Spektrum aufweist. Daher wurden im Rahmen dieser Arbeit tiefe Beobachtungen dieses Galaxienhaufens mit LOFAR im Frequenzbereich von 120 bis 180 MHz und dem GMRT bei 322 MHz und 608 MHz durchgeführt. Die Untersuchungen wurden mit Archivdaten des Röntgensatellits Chandra ergänzt.

Durch die Analyse der Daten konnte der Radiohalo in der Hauptkomponente von Abell 2069 bestätigt und die Radioemission in der Teilkomponente als Radiominihalo klassifiziert werden. Dabei finden sich Hinweise für die Existenz fossilen Plasmas eines ehemalig aktiven galaktischen Kerns. Eine Diskontinuität im Haufengas („cold front“) der Teilkomponente deutet auf Schwappen des Haufengases („gas sloshing“) hin, das zu großräumiger Umverteilung von fossilem Plasma und Turbulenz führen kann. Dabei kann das fossile Plasma auf relativistische Energien beschleunigt werden.

Diese Arbeit zeigt, dass Radiobeobachtungen bei niedrigen Frequenzen ein gutes Instrument sind, um die internen Prozesse im Haufengas von Galaxienhaufen zu studieren.

Abstract

Extended diffuse radio features, so-called radio halos, radio relics and radio mini-halos, are found in about 100 galaxy clusters. The radio emission originates from relativistic electrons suffering synchrotron losses in the magnetized intra-cluster medium. Little is known about the mechanisms how electrons in the intra-cluster medium get accelerated to relativistic energies. Observations at low radio frequencies permit the analysis of the distribution of the population of aged relativistic electrons. This provides insights into the origin of the relativistic electrons and their role in the galaxy cluster's evolution.

In this work, we analyzed, in the context of the WSRT 346 MHz Legacy Survey, ten galaxy clusters with already known diffuse radio sources and yet unclassified sources. We confirm radio relics in three clusters, radio halos in five clusters, and classified a radio relic candidate as a radio galaxy. Furthermore, we revealed radio features with remarkable morphology in the galaxy cluster Abell 2069.

Abell 2069 is a complex merging galaxy cluster, which shows two distinct X-ray peaks. The main cluster component evidently possesses a radio halo and the subcomponent exhibits ultra-steep spectrum diffuse radio emission of uncertain nature. We conducted follow-up observations on Abell 2069 with LOFAR in the frequency range from 120 to 180 MHz. We complemented our investigation of Abell 2069 with GMRT observations at 322 MHz and 608 MHz as well as with archival Chandra X-ray data. Our analysis confirms the presence of a radio halo in the main cluster component. Furthermore, we classify the diffuse radio emission in the subcluster as radio mini-halo. We detected signatures of fossil plasma ejected during a former active phase of an Active Galactic Nuclei in the subcluster. A cold front in the subcomponent suggests the presence of internal gas sloshing, which could have induced bulk motions and turbulence in the subcluster. Both mechanisms together may have redistributed and re-accelerated the fossil plasma and caused the diffuse radio emission.

This work shows that deep radio observations at low frequencies are a powerful tool for shedding light on the intrinsic dynamics of the intra-cluster medium in galaxy clusters.

Contents

List of Figures

List of Tables

Acknowledgments:

Hiermit möchte ich mich bei allen Menschen bedanken, die mich während meiner Zeit als Doktorand an der Thüringer Landessternwarte in Tautenburg begleitet und unterstützt haben. Allen voran danke ich Dr. Matthias Hoeft, der in den letzten Jahren mit viel Zeit, Geduld, Wissen, Erfahrung und unermüdlichem Engagement in besonderem Maße zum Gelingen dieser Arbeit beigetragen hat. Ganz besonders möchte ich mich auch bei meinen Freunden und Kollegen in der Radioastronomie Jakob Gelszinnis, Cosmos Dumba und Kamlesh Rajpurohit für das Durchlesen des Manuskripts und die vielen hilfreichen Gespräche und Diskussionen bedanken, die mir stets Anregungen für meine Arbeit gaben.

Die Arbeit an der Thüringer Landessternwarte in Tautenburg war für mich stets etwas ganz Besonderes. Mein Dank gilt meinen Arbeitskollegen und Freunden Daniel Sebastian, Sebastian Schmidl, Dr. Станислав Мельников, Volker Beimborn, Frank Pertermann, Michael Hartmann und Dr. David Alexander Kann, die mir unter anderem bereits seit meiner Diplomarbeit jederzeit konstruktiv zur Seite standen. Für die angenehme, ruhige und unkomplizierte Arbeitsatmosphäre bedanke ich mich bei allen Mitarbeitern der Thüringer Landessternwarte in Tautenburg, insbesondere dem technischen Personal, dem Direktor Prof. Dr. Artie Hatzes, dem stellvertretenden Direktor Prof. Dr. Helmut Meusinger, der Verwaltung und der Familie Fuhrmann, die oft mit Kleinigkeiten das Arbeiten an der Sternwarte bereicherten. Dabei danke ich besonders Bernd Fuhrmann für all die Mühen bei der Bereitstellung, Wartung und der Installation der notwendigen Computerhardware und -software. Diese Zuverlässigkeit und Schnelligkeit, oft im Wochenrhythmus, waren eine unschätzbare Hilfe bei der Bewältigung der sehr großen Datenmengen, die bei meinen Beobachtungen angefallen sind.

Zu guter Letzt danke ich meiner gesamten Familie und meinen Freunden, insbesondere meinen Eltern und meiner Verlobten Larissa, die mich in den Jahren meiner Promotion immer begleitet, motiviert und mir den Rücken gestärkt haben.

This research has made use of data obtained from the Chandra Data Archive and the Chandra Source Catalog, and software provided by the Chandra X-ray Center (CXC) in the application packages CIAO, ChIPS, and Sherpa. Funding for SDSS-III has been provided by the Alfred P. Sloan Foundation, the Participating Institutions, the National Science Foundation, and the U.S. Department of Energy Office of Science. SDSS-III is managed by the Astrophysical Research Consortium for the Participating Institutions of the SDSS-III Collaboration.

1 Introduction

Clusters of galaxies are the largest gravitationally bound systems in the Universe. The study of their history and their evolution is crucial for the understanding of the hierarchical structure formation in the Universe.

Some galaxy clusters show spectacular diffuse synchrotron emission with low surface brightness, observed at radio wavelengths, and extended up to Megaparsec scales. These diffuse synchrotron sources are not related to any galaxy and are associated with the intracluster medium (ICM). Depending on their morphology, size, and location with respect to the possessing galaxy cluster, these sources are classified as radio halos, radio mini-halos, and radio relics. They indicate the existence of magnetic fields and relativistic electrons in the ICM. The presence of diffuse radio sources in galaxy clusters caused a lively debate on their origin. Interestingly, these sources do not appear to be common in galaxy clusters. In total, only about one hundred diffuse radio sources have been discovered so far.

Present theoretical models suggest that radio halos and radio mini-halos originate from re-acceleration of mildly relativistic seed electrons to highly relativistic energies due to turbulence in the ICM. In contrast, radio relics trace shocks producing relativistic electrons in the ICM. Turbulence as well as shocks in the ICM are induced by galaxy cluster mergers. Thus studies at radio wavelengths of galaxy clusters are a powerful instrument to get insights into the conversion of gravitational energy into non-thermal energy. Since the observing frequency constrains the visible energy regime of the relativistic electrons, the spectrum of the diffuse radio sources is a fundamental observable. It provides information about the origin of the synchrotron radiation emitting relativistic electrons. Unfortunately, obtaining a reliable spectrum of diffuse sources at different frequencies spread over at least one order of magnitude is quite challenging and therefore only available for a few bright diffuse sources so far. Most of the diffuse radio sources have been discovered at a frequency of 1.4 GHz and 610 MHz thanks to exhaustive observational campaigns with the Very Large Array (VLA) and Giant Metrewave Telescope (GMRT), respectively. Hence, not much is known about the properties and the frequency of occurrence of diffuse radio sources at frequencies far below 1.4 GHz.

At low frequencies, radio observations allow deeper insights into the distribution of the population of aged relativistic electrons, i.e. electrons which already suffered synchrotron and inverse Compton losses. Therefore, measuring flux densities and constraining morphologies of diffuse radio sources at low frequencies will help to test current models. Due to low resolution a proper analysis of the flux density of extended sources at low frequencies is difficult, i.e., many sources suffer from confusion with embedded sources like active galactic nuclei (AGN) or radio galaxies. In re-acceleration models radio halos and radio mini-halos are more common than presently observed. Therefore, a population of so-called ultra-steep spectrum radio halos, if they exist, e.g., in case of less violent merger events, have been highly missed by current observations. The investigation of galaxy clusters in the low frequency radio regime is thus necessary to complement the fundamental picture of the origin of relativistic particles in the ICM and their role in the galaxy cluster's evolution.

In this work, we investigate a large sample of galaxy clusters with known but only little studied diffuse radio sources at low radio frequencies and analyze their spectrum and their morphology with respect to observations conducted at higher frequencies. We aim for a proper classification of these diffuse radio sources in order to discuss them in the context of the current picture of the dynamics in galaxy clusters.

2 Diffuse radio emission in galaxy clusters

To understand the origin of diffuse radio sources observed in galaxy clusters, a large variety of aspects needs to be considered, ranging from large-scale structure formation to plasma phenomena. First, the properties of galaxy clusters, their dynamical state, and the processes related to the ICM, e.g., shock fronts and turbulence (Sec. 2.1), set the scene and thus play a key role in the understanding of the origin of the diffuse radio emission. Secondly, the spectrum and the morphology of the diffuse radio emission represents the energy and the spatial distribution of the cosmic ray electron population (Sec. 2.2), respectively. This is a powerful instrument to constrain the current models of the origin of diffuse radio sources.

The subdivision of the diffuse radio emission in galaxy clusters into radio halos (Sec. 2.3.1), radio relics (Sec. 2.3.2), and radio mini-halos (Sec. 2.3.3) is based on the morphology and the location of these sources. The diversity of the diffuse radio sources is an expression of the complexity of the physics present in the ICM. It is suggested that the different classes of diffuse radio emission reflect different mechanisms of their origin. Therefore, it is necessary to work out the particular characteristics of each type of diffuse radio emission in order to confirm or falsify present models. The currently favoured model for radio relics, the diffusive shock acceleration (DSA) model (Sec. 2.4.1), as well as the models for radio halos and radio mini-halos, the turbulent re-acceleration model (Sec. 2.4.3), and the hadronic collision model (Sec. 2.4.2), address this challenge, whereas a set of major questions is still left open (Sec. 2.5).

2.1 The intracluster medium

Galaxy clusters are the largest gravitationally bound systems in the Universe and show a typical diameter of 1 to 10 Mpc. They consist of up to hundreds of galaxies (e.g., Abell, 1958; Abell et al., 1989) and their mass ranges from 10^{13} to $10^{15} M_{\odot}$. Only ~20% of the mass is in the form of baryonic matter which is composed of hot ionized gas, the ICM (~15%), and condensed matter in galaxies (~5%), e.g., stars. Dark matter, which contributes to ∼80% of the total mass, provides the dominant gravitational potential of any galaxy cluster. Dark matter filaments govern the structure of the Universe on the largest scales. The gravitational attraction of the dark matter filaments leads to the formation of the "cosmic web" (Jöeveer et al., 1977; Springel et al., 2005). Galaxy clusters reside at the nodes or intersections of the dark matter filaments and are formed by hierarchical structure formation processes (Kravtsov and Borgani, 2012). They evolve through accretion of galaxies and merging with smaller or larger groups of galaxies or clusters. Major mergers of galaxy clusters are among the most energetic events in the Universe (Sarazin, 2002) with typical collision velocities of the order of $2000\,\mathrm{km\,s^{-1}}$. They generate shock waves which subsequently heat the ICM and may inject turbulence in the ICM (Ryu et al., 2008). This dissipation heats the ICM up to temperatures of 10^6 to $10^8\,\mathrm{K}$. At such high temperatures the ICM is almost fully ionized and thermal bremsstrahlung is dominating the emission in the X-ray regime, with integrated luminosities of $L_\mathrm{X} \sim 10^{43} \ldots 10^{45}\,\mathrm{ergs\,s^{-1}}$ (see, e.g., Sarazin, 2008, for a review). The X-ray radiation from the thermal bremsstrahlung is the main process for cooling the ICM. The X-ray volume emissivity I_X along the line of sight scales with the product of the electron and ion particle density. Assuming a galaxy cluster with a uniform temperature distribution and a uniform metal abundance, and thus a constant electron to proton ratio, the X-ray volume emissivity j_X traces the particle number density of the ICM n_ICM

$$j_\mathrm{X} \propto n_\mathrm{ICM}^2. \tag{2.1}$$

The particle number density of the ICM is decreasing with increasing distance from the cluster's core, ranging from $10^{-4}\,\mathrm{cm^{-3}}$ at the cluster outskirts to $10^{-2}\,\mathrm{cm^{-3}}$ at the cluster's core.

Galaxy cluster mergers still occur in our present and observable Universe. Recent merger episodes are indicated by a disturbed X-ray surface brightness distribution as well as a complex X-ray temperature distribution (Honda et al., 1998; Rossetti et al., 2004).

In our nearby Universe ($z \lesssim 0.5$) the majority of galaxy clusters found appear to be in a "relaxed" state, so-called cool core clusters (see, e.g., Mann and Ebeling, 2012). They show an enhanced X-ray luminosity peak at the center and a significant drop in the temperature distribution (De Grandi and Molendi, 2001). This is due to the high density in the core which substantially shortenes the radiative cooling time t_cool (see, e.g., Bharadwaj et al., 2014). This causes a severe and more rapidly accelerating energy loss of the ICM ("cooling flow") which needs to be balanced out (Fabian, 1994).

At the bottom of the relaxed galaxy cluster's potential well a brightest cluster galaxy (BCG) is settled. The BCG is usually a very massive elliptical galaxy which is believed to grow in the galaxy cluster's core from galaxy mergers through cannibalism due to dynamical friction (Ostriker and Hausman, 1977). AGN activity of the BCG (so-called "AGN feedback") in the cool core cluster is a candidate to provide sufficient amount of energy for heating the ICM and to balance the cooling (see, e.g., Voit, 2005; Böhringer and Werner, 2010).

2.2 Cosmic rays and synchrotron emission

It is believed that a small fraction of the energy dissipated from matter accretion during structure formation is channeled into non-thermal ICM components, e.g., relativistic particles, in the following called cosmic rays (see, e.g., Brunetti and Jones, 2014, for a review). Faraday Rotation Measure (RM) analysis of polarized galaxies inside or behind the galaxy cluster (Govoni and Feretti, 2004) revealed the presence of magnetic fields in galaxy clusters. The magnetic field strength is estimated to be around 0.1 to 1 μG (Ryu et al., 2008) and might reach values of about 10 μG in the center of cool core clusters (Carilli and Taylor, 2002).

The synchrotron emission is caused by cosmic ray electrons spiralling around magnetic field lines. The synchrotron spectrum of a single particle is a continuum which peaks close to its critical angular frequency ω_c

$$\omega_\mathrm{c} = \frac{3\gamma^2 q B \sin\eta}{2m}, \tag{2.2}$$

where $\gamma = \sqrt{1-\beta^2}^{\,-1}$ $(\beta = v\,c^{-1})$ is the Lorentz factor of a cosmic ray particle, q its charge, m its mass, and η the pitch angle between the direction of the magnetic field $\vec{B}$ of the ICM and the particle's velocity $\vec{v}$ (see, e.g., Govoni and Feretti, 2004; Feretti and Giovannini, 2008). So, with increasing magnetic field strength B less-energetic cosmic ray particles mostly contribute to the synchrotron emission at a given observing frequency. Typically, cosmic ray electrons with a Lorentz factor $\gamma > 10^4$ are observed at radio frequencies between $\nu \sim 10^2$ and 10^4 MHz in galaxy clusters with a magnetic field strength in the regime of ∼μG. In the case of a power-law energy distribution, the number density n of cosmic ray electrons in the energy regime between γ and $\gamma + d\gamma$ is given as

$$n\left(\gamma\right) d\gamma \propto \gamma^p d\gamma, \tag{2.3}$$

where p is the index of the cosmic ray electron population. The spectral flux density

S_ν in the frequency range between ν and $\nu + d\nu$ varies with

$$S_\nu \propto \nu^\alpha, \tag{2.4}$$

where the spectral index α is related to the index of the electron population.

$$\alpha = \frac{p+1}{2}. \tag{2.5}$$

A constant spectral index of the observed synchrotron emission over a larger frequency range thus implies a power-law energy distribution of the cosmic ray particles over the corresponding range in energy. The total emitted power P of an accelerated charged cosmic ray particle strongly depends on its Lorentz factor, the magnetic field strength of the ICM, and the particle's mass

$$P \propto \frac{\gamma^2 B^2}{m^2}. \tag{2.6}$$

Furthermore, highly-relativistic electrons also suffer from Inverse Compton (IC) scattering with cosmic microwave background (CMB) photons

$$P_{\mathrm{IC}} \propto \gamma^2 U_{\mathrm{CMB}}, \tag{2.7}$$

where U_{CMB} denotes the energy density of the CMB. Higher energetic particles are thus cooling significantly faster than those of lower energy. This process is called "particle aging" and is visible through spectral breaks at frequencies higher than the corresponding "cutoff frequency" or it is visible as a curved spectrum. Thus, in case of a magnetic field strength of the order of $\sim$ µG, spectra of highly relativistic electrons (with energies of $\sim$ GeV) should become curved if there is no continuous particle injection at timescales of ~ 0.1 Gyr (Enßlin et al., 2011). Intrinsically, synchrotron emission of a power-law cosmic ray electron population in a uniform magnetic field is linearly polarized to a degree of

$$\Pi = \frac{1-p}{\frac{7}{3}-p} \tag{2.8}$$

integrated over all frequencies and electron energies. A typical spectral index for synchrotron sources is $\alpha \approx -0.8$ (see, e.g., Williams et al., 2016) and therefore $p \approx -2.6$ which corresponds to a high degree of intrinsic polarization of $\Pi \approx 73\%$.

2.3 Observational classification of diffuse radio sources

2.3.1 Radio halos

Radio halos are diffuse extended radio sources which often show a regular and smooth shape with an extent of about ~ 1 Mpc centered at the associated galaxy cluster, see, e.g., the radio halo in Abell 2163 in the upper panel of Fig. 2.1. Radio halos are not significantly polarized. Only upper limits for the degree of polarization down to a few percent have been derived (Feretti et al., 2001; Bacchi et al., 2003). Feretti et al. (2012) reported 42 radio halos and Yuan et al. (2015) published the most comprehensive list of 59 radio halos. For galaxy clusters with radio halos, the more X-ray luminous galaxy clusters, and therefore the more massive galaxy clusters, tend to possess more powerful radio halos (Cassano, 2010; Cassano et al., 2013). This is called the "radio - X-ray luminosity correlation" and is usually given for radio luminosities at a reference frequency of 1.4 GHz, see lower panel in Fig. 2.1. Furthermore, there are only a few faint galaxy clusters known that possess radio halos (Giovannini et al., 2009, 2011; Brown et al., 2011a). The spectra of radio halos follow a power-law and are thus believed to resemble synchrotron emission caused by a power-law energy distribution of cosmic ray electrons. The spectral indices of radio halos vary greatly, but are always steep ($\alpha \lesssim -1$). Some of them even show ultra-steep ($\alpha \lesssim -1.7$) spectra (see, e.g., Feretti et al., 1997a; Bacchi et al., 2003; Dallacasa et al., 2009) and are less luminous than expected from the radio - X-ray luminosity correlation at a reference of 1.4 GHz (Venturi, 2011). Because of a lack of integrated spectra measured over a larger frequency range, especially above 1.4 GHz and below 400 MHz, the spectral properties of radio halos are only marginally known (Feretti et al., 2012). More radio halos, in particular ultra-steep ones, are expected to be discovered with the advent of high-sensitivity low frequency radio telescopes like the Low Frequency Array (LOFAR). For only a few radio halos so far a spatially resolved spectral index analysis was performed, because of the need of high sensitivity observations at several frequencies at the same resolution to perform it. These spectral index maps allows one to reveal the existence of patches of steeper (see, e.g., radial steepening in Giovannini et al., 1993; Feretti et al., 2004b) and flatter spectra, reflecting areas in which the radiating particles significantly lose or gain energy, respectively (Pizzo and de Bruyn, 2009). Feretti et al. (2004a) and Orrú et al. (2007) found evidence that the spectrum of the radio emission is flatter in case of a hotter ICM and is thus related to the amount of energy dissipated in the ICM. Another evidence for the direct connection between the thermal and the non-thermal components of the ICM is the spatial correlation

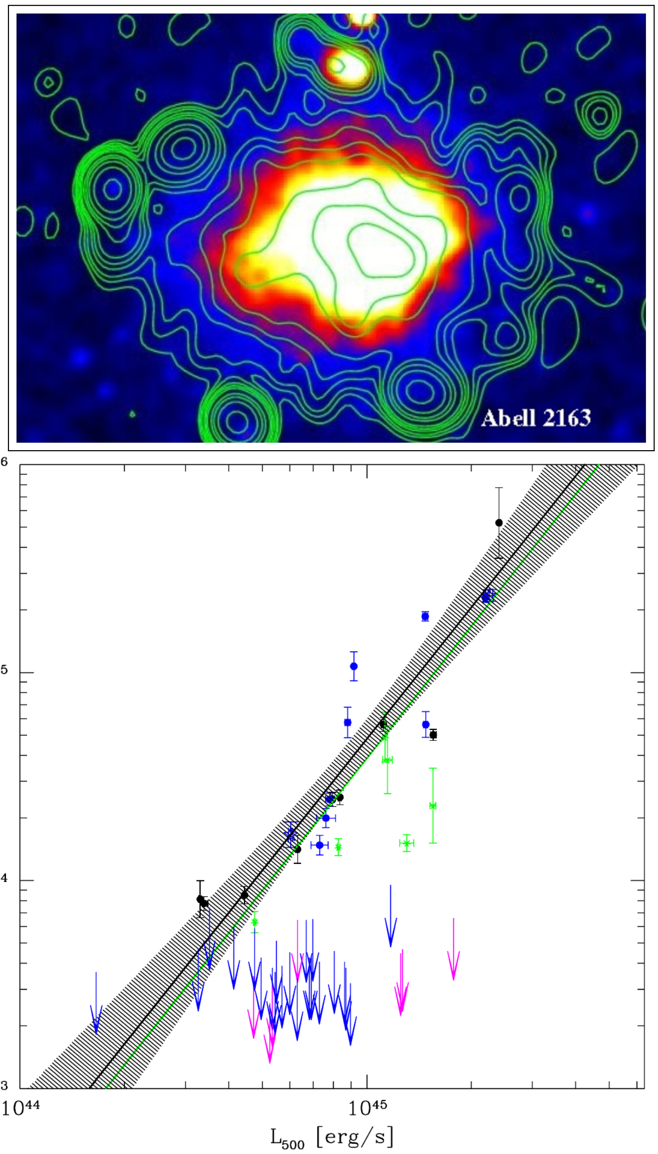

Figure 2.1: *Upper panel:* Map of the radio halo in Abell 2163 as observed with the VLA at 1.4 GHz. The radio contours are overlaid on the XMM-Newton image in colorscale (Feretti et al., 2001; Arnaud, 2008). *Lower panel:* Radio halo power at 1.4 GHz $P_{1.4\,\mathrm{GHz}}$ versus X-ray luminosity L_{500} adapted from Cassano et al. (2013). Black dots indicate radio halos, blue dots indicate radio halos from the Extended GMRT Radio Halo Survey (EGRHS) (Kale et al., 2013), and green asterisks indicate ultra-steep spectrum radio halos. The arrows indicate the upper limits of non-detections, where cool core clusters are shown in magenta. The solid black (green) line represents the best fit (including ultra-steep spectrum radio halos). The dashed area represents the 95% confidence region.

between the X-ray and radio surface brightness of radio halos (Govoni et al., 2001a, 2009).

The existence of radio halos raised the question about their origin. Especially, the origin of the highly relativistic electrons and the origin of the cluster's large-scale magnetic field play a key role in understanding the creation of radio halos. The fact that no significant polarization has been detected in radio halos suggests the presence of internal depolarization along the line-of-sight (LoS) or beam depolarization, which means that the magnetic field lines are disordered on scales smaller than the observing beam (Feretti and Giovannini, 1996). Moreover, relativistic electrons are suffering Coulomb losses ($\gamma \lesssim 10^4$) as well as synchrotron and IC scattering losses with the CMB photons ($\gamma \gtrsim 10^4$). The radiative lifetime is estimated to be of the order of $\sim 10^8$ yr at typical energies of ~ 1 GeV (visible at $\sim$ GHz frequencies) and $\sim$ μG magnetic field strengths (Sarazin, 1999). On the other hand, relativistic electrons need about the Hubble time to diffuse on Mpc-scales of galaxy clusters (Blasi et al., 2007). Therefore, it can be ruled out that the radiating electrons are produced at a certain location of the cluster and propagate through the entire cluster volume (Feretti et al., 2012) ("diffusion problem").

Observations have shown that radio halos are found in dynamically disturbed galaxy clusters that recently undergo a major merger (Cassano et al., 2010; Akamatsu et al., 2012). On the other hand, radio halos are not present in all merging galaxy clusters (Russell et al., 2011). Bonafede et al. (2014b) reported about the cool core cluster CL1821+643 as a first potential candidate for a radio halo in a relaxed system. The dichotomy of the merging galaxy cluster population in terms of the occurrence of radio halos ("radio halo dichotomy") is not well understood.

2.3.2 Radio relics

Radio relics are also steep spectrum ($\alpha \lesssim -1$) diffuse extended radio sources with low surface brightness and a largest linear size (LLS) of about ~ 1 Mpc. In contrast to radio halos, radio relics are usually located at the periphery of galaxy clusters, typically at distances between 0.5 and 1.5 Mpc to the galaxy cluster center. They often show an elongated morphology, where the semimajor axis is roughly perpendicular to the direction of the galaxy cluster center. Typically, their surface brightness profile shows a sharp edge outwards. Therefore, radio relics probe the ICM and the magnetic fields of galaxy clusters in the low-density environment of the galaxy cluster outskirts. Feretti et al. (2012) have reported 50 radio relics in 39 galaxy clusters. About every fourth radio relic system is a double radio relic system where the radio relics are typically located on opposite sides of the galaxy cluster (see, e.g., Rottgering et al., 1997). Shock fronts with moderately high Mach numbers $\mathcal{M} \sim 1 \ldots 3$, detected as X-ray surface brightness and temperature jumps, propagating outwards to the cluster's periphery have been detected in merging galaxy clusters (Markevitch et al., 2002; Russel, 2010; Owers et al., 2014). Hereby, the Mach number is defined as $\mathcal{M} = v_{\text{shock}} \cdot c_{\text{sound}}^{-1}$, where v_{shock} denotes the speed of the shock front and c_{sound} the upstream sound speed. Often those shock fronts coincide with radio relics (Finoguenov et al., 2010; Ogrean et al., 2013; Botteon et al., 2016b) seen roughly edge-on, suggesting a direct connection between the injection of cosmic ray electrons with their corresponding shocks. Nevertheless, there are also shock fronts detected without the presence of a radio relic (Russell et al., 2011). Furthermore, radio relics show a high degree of polarization (up to $\sim 50\%$) often perpendicular to the radio relic's elongation (see, e.g., Clarke and Ensslin, 2006; van Weeren et al., 2010). Observations also provide evidence for spectral steepening towards the cluster center (Giacintucci et al., 2008; van Weeren et al., 2012), indicating a population of freshly injected cosmic ray electrons at the outer edge of the radio relic. They are aging while the shock front is further traveling outwards. The radio relic in the galaxy cluster CIZA J2242.8+5301 (van Weeren et al., 2010) is a "textbook example" of a radio relic (see Fig. 2.2).

2.3.3 Radio mini-halos

Radio mini-halos are steep spectrum ($\alpha \lesssim -1$) low surface brightness diffuse extended radio sources which are also associated to the ICM. They have these properties in common with radio halos. In contrast to radio halos, they are less extended ($\lesssim 500\,\text{kpc}$), comparable to the size of the galaxy cluster core. Feretti et al. (2012) reported 11 radio mini-halos and Yuan et al. (2015) listed 19 radio mini-halos.

The fact that they are typically discovered in cool core galaxy clusters rather than in merging galaxy clusters challenges the idea that radio mini-halos are just a "small version" of a radio halo. Interestingly, cold fronts have been detected in some galaxy clusters that show a radio mini-halo (Mazzotta and Giacintucci, 2008). Cold fronts are sharp contact discontinuities between hot gas and colder, denser gas with both sides being in pressure equilibrium (see, e.g., Forman et al., 2002). There is evidence of large-scale motion of the cold gas in the core regions in cool core galaxy clusters (see, e.g., Sanders et al., 2009). The cool core cluster could have been disturbed through minor or off-axis cluster mergers (Ascasibar and Markevitch, 2006) where the cool core has survived partially (Markevitch et al., 2000; Vikhlinin et al., 2001; Churazov et al., 2003). Such mergers might displace the dark matter core from the cool gas and initiate

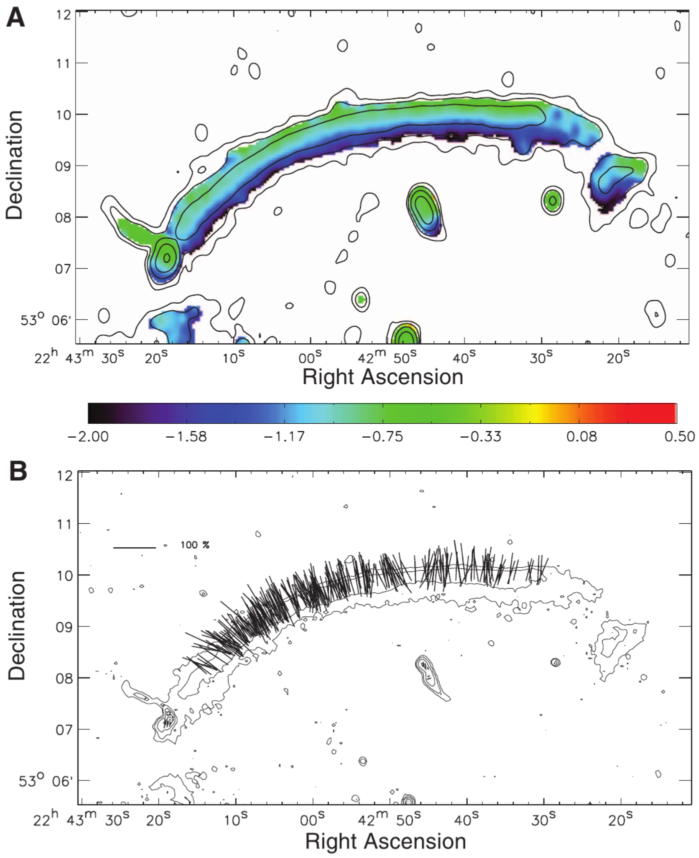

Figure 2.2: The radio relic in CIZA J2242.8+5301 (van Weeren et al., 2010). *Upper panel:* Spectral index map (van Weeren et al., 2010). *Lower panel:* Polarization map showing the $\vec{E}$-field distribution.

the so-called spiral-shaped “gas sloshing” (Markevitch and Vikhlinin, 2007), which is also detected in some galaxy clusters possessing radio mini-halos (Clarke et al., 2004; Sanders et al., 2009). In some cases the edge of the radio mini-halo emission agrees with the cold front (Giacintucci et al., 2014).

Murgia et al. (2009) have introduced and measured the volume-averaged radio emissivity for several radio halos and radio mini-halos (see equation 5.6). In their work, radio mini-halos show a wide span of the observed synchrotron emissivity, whereas radio halos show a rather constant radio emissivity, see Fig. 2.3. It is discussed whether the central AGN might power radio mini-halos (Govoni et al., 2009; Giacintucci et al., 2014). Fujita et al. (2007) argued that the wide span of the observed synchrotron emissivity for radio mini-halos could be explained by the central AGNs powering the radio mini-halos. All galaxy clusters possessing radio mini-halos known so far host central powerful AGNs.

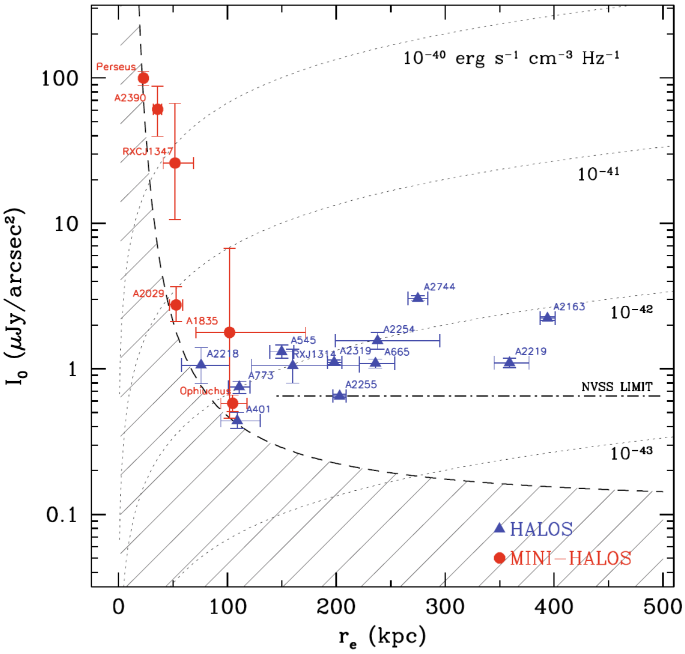

Figure 2.3: Fitted central brightness I_0 of radio halos (blue triangles) and radio mini-halos (red dots) versus the fitted e-folding radius r_e adapted from Murgia et al. (2009), see also equation 5.7. The dotted curves indicate regions of constant emissivity. The comparison is done by assuming a redshift of $z = 0.18$ and a spectral index of $\alpha = -1$. The dashed line represents the detection limit at $z = 0.18$ observed with a beam of 25 arcsec and a sensitivity level of 25 μJy beam^{-1} and the dot-dashed line represents the 3σ level of the NRAO VLA Sky Survey (NVSS).

But still, even radio mini-halos with a size of $\sim 50\,\mathrm{kpc}$ suffer from the diffusion problem (see Sec. 2.3.1), since the highly magnetized high density central region of cool core clusters shows a large diffusion time for cosmic ray electrons (Giacintucci et al., 2014). Therefore, radio mini-halos can not be simply explained with outflows of strong AGNs that have been diffused into the ambient medium.

Furthermore, radio mini-halos should not be confused with AGN outflows which create large cavities in the ambient ICM, the so-called "radio bubbles" (see, e.g., Blanton et al., 2011).

2.4 Origin of cosmic ray electrons

2.4.1 Diffusive shock acceleration

Fermi (1949) presented a theory where cosmic rays are produced by collisions of charged particles against moving magnetic fields in a collisionless plasma, i.e., particles diffusing through an area of randomly moving magnetized "clouds" are more likely to experience a "head-on" encounter than a "head-tail" encounter, which thus leads to net acceleration. Since the energy gain per particle per scattering in this scenario is scaling with the magnetized cloud velocity $\propto \beta_{\mathrm{cloud}}^2$, this process is called "second-order Fermi acceleration". Shocks propagating through the galaxy cluster, e.g., as a consequence of merger activities or matter accretion, also permit such kind of diffusive acceleration (Blandford and Eichler, 1987; Gabici and Blasi, 2003). The infall velocities of the subclusters are comparable to their escape velocities, i.e., the kinetic energy of the infalling subclusters is slightly larger than the gravitational potential. This results in moderately supersonic shocks in merging galaxy clusters (Sarazin, 2008). Shocks then compress and heat the "downstream" area. Charged particles diffusing across the shock are temporarily trapped in a converging flow and repeatedly reflected between the "upstream" and the "downstream" area, yielding to a gain in energy with every reflection $\propto \beta_{\mathrm{shock}}$, until they eventually escape into the downstream area (Baring, 1997). The DSA model is a "first order Fermi acceleration" model. According to the DSA model, shock fronts are able to accelerate electrons to relativistic energies (Enßlin et al., 1998; Hoeft et al., 2008; Kang and Ryu, 2013) with a power-law energy spectrum of the injection index p_{inj}

$$p_{\mathrm{inj}} = 2\frac{1+\mathcal{M}^2}{1-\mathcal{M}^2}, \tag{2.9}$$

compress magnetic field lines, and align them with the shock front (Brüggen et al., 2012), as suggested from polarization measurements of radio relics (see Sec. 2.3.2). Thus, the spectral index of the leading edge of a radio relic ("injection spectral index") is a direct measure of the shock front's Mach number (see equation 2.5). For a simple planar shock model, where the electron cooling time is much shorter than the lifetime of the shock, the volume integrated spectral index is steeper than the injection spectral index $\alpha_{\text{int}} = \alpha_{\text{inj}} - \frac{1}{2}$ (Ginzburg and Syrovatskii, 1969). For strong shocks $\mathcal{M} \rightarrow \infty$ the flattest observed integrated spectrum is thus limited to $\alpha_{\text{int}} = -1$. The short radiative lifetime of cosmic ray electrons leads to a steepening of the radio spectrum in the downstream area with increasing distance to the shock front. The maximum travel distance from the shock limits the transverse size of radio relics to $\sim 100\,\text{kpc}$ (Brunetti and Jones, 2014).

Applying the DSA model to the radio spectra, the inferred Mach number is much higher than typically measured from X-ray data (see, e.g., Pinzke et al., 2013; Vazza and Brüggen, 2014; van Weeren et al., 2016a), i.e. for the DSA model the production of cosmic ray electrons from the thermal pool is much less effective, especially for weak shocks. It is thus speculated that AGNs in radio galaxies might provide a pool of relativistic seed electrons, which are re-accelerated at the shock. Following this line of reasoning, Bonafede et al. (2014a) proposed a physical connection between lobes of a radio galaxy and radio relics.

2.4.2 Hadronic collisions

In the "hadronic" model (see, e.g., Dennison, 1980; Blasi and Colafrancesco, 1999) secondary relativistic electrons, causing the observed power-law synchrotron emission, are injected into the ICM after a decay chain produced by inelastic collisions of cosmic ray protons with thermal nuclei of the ambient ICM:

$$\mathrm{p}^{+} + \mathrm{p}^{+} \rightarrow \pi^{0} + \pi^{\pm} + \dots . \tag{2.10}$$

The neutral pion π^0 is immediately decaying into gamma rays, whereas the charged pions $\pi^{\pm}$ decay into a set of neutrinos and relativistic electrons (Pfrommer and Enßlin, 2004). The cosmic ray protons also need to be injected during the structure formation history of the cluster, e.g., due to merger and accretion shocks (Colafrancesco and Blasi, 1998), AGNs (Enßlin et al., 1997) or star formation (Völk et al., 1996). Since cosmic ray protons are of higher mass than electrons, synchrotron (see equation 2.6) and IC scattering losses are negligible. They mainly lose energy via hadronic collisions (Blasi et al., 2007) of protons with energies $\gtrsim 1\,\text{GeV}$. Thus, their radiative lifetime is of the order of the Hubble time (Berezinsky et al., 1997). Therefore, the population of cosmic ray protons should have been accumulated over cosmological timescales and are able to diffuse on galaxy cluster scales (Enßlin et al., 2011).

Thus radio halos should be present in virtually all galaxy clusters without a spatial dependence of the spectral index (Feretti et al., 2012). This is ruled out by the presence of the radio halo dichotomy. The density of cosmic ray protons in galaxy clusters can be directly measured through the γ-ray flux density. Current upper limits of the γ-ray emission in nearby galaxy clusters severely challenge the hadronic scenario (Brunetti, 2009; Ackermann et al., 2010, 2014; Brunetti et al., 2012; Zandanel and Ando, 2014).

The hadronic model is still discussed for radio mini-halos. Here, recent simulations show that gas sloshing in cool core clusters (see Sec. 2.3.3) might be able to amplify the magnetic field significantly (ZuHone et al., 2015), i.e. the amount of secondary relativistic electrons needed to cause radio mini-halo emission of a certain flux density is less than expected. Therefore, the expected γ-ray emission from hadronic collisions is lower than the current FERMI-limits (Pfrommer and Enßlin, 2004).

2.4.3 Turbulent re-acceleration

Radio halos occur in merging galaxy clusters, see Sec. 2.3.1. Simulations show that a signifcant fraction ($\gtrsim 10\%$) of the energy dissipated in the ICM during a merger is injected in turbulence (Cassano and Brunetti, 2004). In the turbulent reaccleration scenario, cosmic ray electrons are re-accelerated to highly relativistic energies (up to $\gamma \sim 10^5$) via magnetohydrodynamic (MHD) turbulence present on Megaparsec scales driven by major mergers (mass ratio roughly similar or less than two) of galaxy clusters (Brunetti et al., 2001; Cassano and Brunetti, 2005). Turbulent re-acceleration is a second order Fermi process and is efficient for a pool of mildly relativistic electrons ($\gamma \sim 10^3$) (Fujita et al., 2003; Petrosian and East, 2008). These seed electrons ("primary electrons") need to be injected, e.g., during the cluster formation history or from AGN and star formation activities like supernova remnants (Blasi et al., 2007). Since the electron cooling time at such energies is rather short ($\sim 0.1\,\mathrm{Gyr}$) (Enßlin et al., 2011) the radio halo emission should be connected to recent ongoing merger events (up to $\sim 1\,\mathrm{Gyr}$) (Kuo et al., 2004) and should show a steepening of the synchrotron spectrum at high frequencies (Petrosian, 2001; Brunetti, 2004). If radio halo emission emerges from turbulence one would expect a complex spatial spectral index distribution of radio halos where hotter parts of the ICM are connected to regions of flatter spectral indices. The presence of ultra-steep spectrum radio halos can be explained by the re-acceleration scenario in cases where the turbulent energy has decreased, so that the efficiency of the electron re-acceleration drops significantly.

Simulations show that MHD turbulence can also be produced in the inner sloshing cores of cool core galaxy clusters (Fujita et al., 2004; ZuHone et al., 2011). In combination with magnetic field amplification turbulent re-acceleration in sloshing cores can cause radio mini-halos strictly confined within the sloshing core's boundaries (ZuHone et al., 2013).

However, the turbulent reaccleration scenario relies on the presence of a cluster-wide population of mildly relativistic seed electrons. It has not been demonstrated yet that structure formation shocks provide the necessary abundance of seed electrons (Pinzke et al., 2015). On the other hand, "hybrid models" claim that major mergers of galaxy clusters can accelerate primary and secondary electrons (Miniati et al., 2001) which subsequently serve as seed electrons (Brunetti and Lazarian, 2011).

2.5 Open questions

There has been much progress in the last decades regarding the investigation of the origin of radio halos, radio relics, and radio mini-halos.

Thanks to a larger sample of objects and more sensitive observations the distinction between different types of diffuse radio emission and their characterization has significantly improved. The connection of radio halos with ongoing merger events is very well established and ultra-steep radio halos have been discovered. This strongly favors the turbulent re-acceleration model for the origin of radio halos (see Sec. 2.4.3). There is evidence that radio relics are created at shock fronts through DSA in the ICM in the aftermath of a merger. Radio mini-halos are often significantly smaller than radio halos and are found in cool core clusters. The presence of cold fronts in some of the galaxy clusters with radio mini-halos suggests the scenario of turbulent re-acceleration in the sloshing motion of the core.

Still many questions remain. The turbulent re-acceleration scenario for radio halos needs cluster-wide mildly relativistic seed electrons for the re-acceleration process. Their origin is still debated. Furthermore, Donnert et al. (2013) suggested that the radio halo dichotomy resembles different evolutionary states of radio halos. The gap in the transient region of the radio - X-ray correlation should be slowly filled by the detection of radio halos, especially of ultra-steep spectrum objects, at low radio frequencies (Knowles et al., 2016). The Mach number derived from radio relics at shock fronts is much higher than the Mach number derived from X-ray observations. This discrepancy raised the question whether there is the need of a pool of mildly relativistic electrons that are re-accelerated through DSA (see Sec. 2.4.1) at the location of the radio relic. In case of radio mini-halos in cool core clusters the origin is basically unknown. Mini-halos might be primarily of hadronic origin, whereas radio halos could experience a transition from a central hadronic emission state to a re-acceleration state where the seed electron population is of hadronic and fossil origin (Zandanel et al., 2014). Nevertheless, a hadronic emission should be present in all galaxy clusters at some level (Brown et al., 2011b), but this has not been detected yet by current instruments. Moreover, since most observational efforts were put on X-ray luminous galaxy clusters, not much is known about less massive systems.

Low radio frequency observations will help to trace the older electron population, and hence complement the current picture of diffuse radio sources. To confirm these models wideband high sensitivity and multi-resolution radio observations of a large sample of targets are needed.

2.6 Basic cosmological quantities

Since galaxy clusters are located at cosmological distances we need to take into account the effects of the expanding Universe in order to determine the spectral luminosity L_ν and the transverse size $\tilde{d}$ of the X-ray and the radio emission in the galaxy cluster's frame. The luminosity distance D_L is defined as

$$S_0 = \frac{L}{4\pi D_L^2}, \tag{2.11}$$

where L is the bolometric luminosity in the galaxy cluster's frame and S_0 is the measured bolometric flux density in the observer's frame. Measuring the flux density within a finite bandwidth, the frequency band $\Delta\nu_0$ in the observer's frame is shifted with respect to the frequency band $\Delta\nu$ of the emission in the galaxy cluster's frame

$$S_{0,\nu}\Delta\nu_0 = \frac{L_\nu \Delta\nu}{4\pi D_L^2} = \frac{L_\nu \left(1+z\right)\Delta\nu_0}{4\pi D_L^2}, \tag{2.12}$$

where $S_{0,\nu}$ is the spectral flux density in the observer's frame and L_ν the spectral luminosity in the galaxy cluster's frame.

For a radio source with a power-law spectrum (see equation 2.4) of a spectral index α we finally get

$$L_\nu = 4\pi D_L^2 \left(1+z\right)^{-(1+\alpha)} S_{0,\nu}. \tag{2.13}$$

For small angles $\sin\vartheta \approx \vartheta$ the measured angular size of an astronomical object ϑ is

$$\vartheta = \frac{\tilde{d}}{D_A}, \tag{2.14}$$

where D_A is the angular size distance. For nearby sources ($z \ll 1$) the luminosity distance and the angular size distance correspond to the geometric distance in an Eucledian space.

The luminosity distance and the angular size distance are functions of redshift and the chosen cosmological model. The current cosmological standard model is the Lambda Cold Dark Matter (ΛCDM) model. It is a Big Bang cosmology that incorporates the cosmological constant Λ, leading to an accelerated expansion of the Universe (usually referred to as "dark energy"), and the presence of dark matter which is said to be "cold" referring to its non-relativistic speed (for a comprehensive overview see, e.g., Schneider, 2015). In this model the distance of objects are computed through dimensionless parameters describing the energy density Ω_k of a certain species k at the present day. The total energy density of a spatially flat Universe is set to 1. A recent determination of cosmological parameters have been performed with *Planck* through mapping the CMB at high resolution and high sensitivity (Planck Collaboration et al., 2016). The observations confirm that the Universe is essentially flat and dominated by the total matter energy density $\Omega_\mathrm{m} = 0.308 \pm 0.012$ and the dark energy density $\Omega_\Lambda = 0.692 \pm 0.012$. The Hubble constant has been determined to be $H_0 = 67.8 \pm 0.9\,\mathrm{km\,s^{-1}\,Mpc^{-1}}$.

The density at which the Universe is flat is called the critical density ρ_c. Often the X-ray luminosity of galaxy clusters is only integrated up to the radius within which the mean over-density of the cluster is 500 times the critical density ρ_c at the cluster redshift. We denote this luminosity as L_{500}.

Throughout this work we assume a ΛCDM cosmology with the Hubble constant $H_0 = 70\,\mathrm{km\,s^{-1}\,Mpc^{-1}}$, $\Omega_\mathrm{m} = 0.3$, and $\Omega_\Lambda = 0.7$.

3 Observations and data reduction

Radio halos, radio mini-halos, and radio relics are sources of low surface brightness ($\sim \mu\mathrm{Jy\,arcsec^{-2}}$), steep spectrum, and often with a large extent ($\sim 1 \ldots 10\,\mathrm{arcmin}$). Single-dish radio telescopes like the Green Bank Telescope (GBT) or the 100-m Effelsberg telescope are therefore well suited to investigate diffuse radio emission with a large extent. Since individual compact radio sources are often embedded in the diffuse radio emission, it is necessary to isolate and subtract them in order to properly measure the flux density, the morphology and even the steep spectrum of a diffuse radio source. Unfortunately, single-dish radio telescopes are often limited by a high confusion due to their large beam size. It might prevent a proper discrimination between compact and extended sources. The drawback of the high confusion of single-dish radio telescopes is even more serious at low frequencies ($\nu < 1.4\,\mathrm{GHz}$), since the beam size increases with longer wavelengths. Radio interferometers (Sec. 3.1) provide a much higher resolution than single-dish radio telescopes, but always have a largest angular scale they can recover.

For the purpose of the analysis of diffuse radio sources a radio interferometer should provide high sensitivity for extended low surface brightness emission as well as high resolution imaging to identify individual sources. In the case of radio interferometers, this is realized by using broadband receivers to increase sensitivity and a sufficient amount of short baselines to increase the largest angular scale the telescope is sensitive to.

The Westerbork Synthesis Radio Telescope (WSRT) (Sec. 3.2.1) was able to offer high quality radio observations in the low frequency regime at $\sim 346\,\mathrm{MHz}$ for quite a while. The low frequency receivers of the WSRT were decommissioned in 2013. Thus, deep observations of ten galaxy clusters with already known or not yet classified diffuse radio sources were performed (Sec. 3.2.2). With respect to the total amount of known sources (~ 100) the analysis of this large sample of galaxy clusters at low frequency allows us to gather new information on these diffuse radio sources.

During this analysis, the galaxy cluster Abell 2069, as introduced in Sec. 5, showed previously undetected diffuse radio features. That's why a dedicated follow-up campaign with the GMRT (Sec. 3.3.1) and the LOFAR High Band Antennas (HBA)

(Sec. 3.3.2) was initiated (Sec. 3.3.3). The LOFAR telescope is part of a new generation of radio telescopes. It is capable of imaging at very high resolution ($\lesssim$ arcsec) at very low frequencies ($\sim 150\,\mathrm{MHz}$) with an unprecedented sensitivity to large-scale emission using as one of the first telescopes a broad frequency range (fractional bandwidth of $\sim 50\%$) and a dense core of short baselines.

The main caveat is that in order to analyze and create maps out of radio interferometer data, one needs to apply the synthesis imaging technique (Sec. 3.4). Since a radio interferometer consists of a finite amount of antennas, the information the instrument provides is always incomplete. Therefore synthesis imaging can only provide one possible interpretation of the sky which matches the observed data.

The data from classical radio telescope interferometers like the WSRT and the GMRT can be basically analysed with a set of well established basic tools for the mitigation of radio-frequency interference (RFI), calibration and imaging (Sec. 3.5). Since LOFAR is a broadband instrument with a large field of view (FoV) and consists of phased arrays without any moving components, calibration and imaging is challenging (Sec. 3.6.1). In particular, an imperfect modelling of the direction- and time-dependent LOFAR beam causes amplitude variations over the entire FoV. Furthermore, at low frequencies the phase distortions of radio signals penetrating the earth's ionosphere become severe in the LOFAR wavelength regime. This requires the development of new calibration strategies (Sec. 3.6.2 and 3.6.3).

Moreover, we complemented our analysis by using Chandra Advanced CCD Imaging Spectrometer (ACIS)-I archival data in order to compare the diffuse radio sources with the extended X-ray emission of the ICM (Sec. 3.7).

3.1 Fundamentals of radio interferometry

The "two-element interferometer" is the simplest realization of a radio interferometer, consisting of two receiving elements ("antennas") separated by the baseline $\vec{b}$, see Fig. 3.1. If both antennas receive a signal from the direction $\vec{s}$ of an infinitely distant radio source, this signal experiences a geometric delay $\tau_{\mathrm{g}} = b \cos\theta \cdot c^{-1}$ at the second antenna with respect to the first antenna, where b is the baseline length and θ the angle between the source and the normal to the baseline vector $\vec{b}$. For simplicity we assume very narrow-band receivers at the frequency ν. Both signals are amplified and their voltage outputs are then multiplied with each other. Afterwards the signal is averaged in time t, typically to the order of seconds. This process is called "correlation" and its output is the "response" $r\left(\tau_{\mathrm{g}}\right)$ of the system. The geometric delay varies slowly while the earth rotates or rather the source is moving across the sky and leads to a fringe

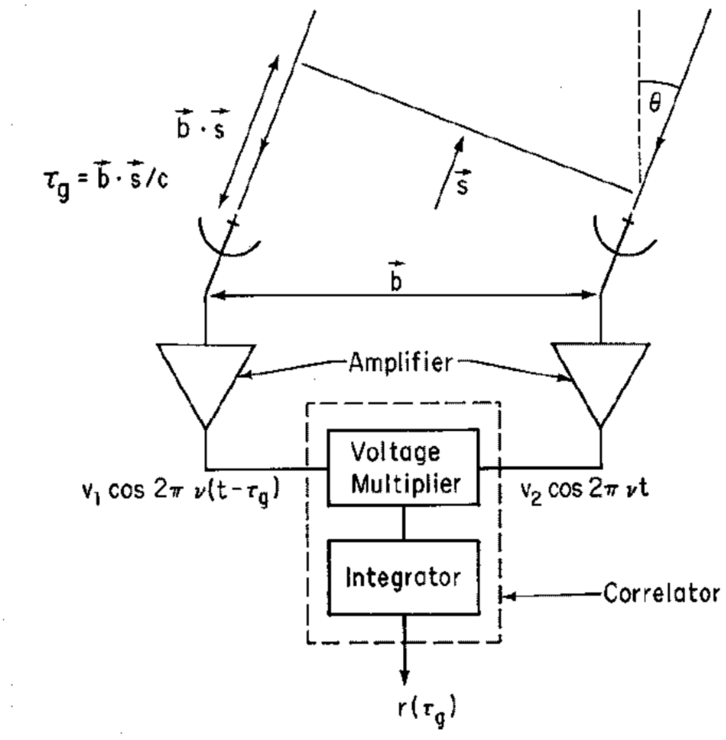

Figure 3.1: Sketch of a two-element radio interferometer adapted from Taylor et al. (1999).

pattern of the correlator response. In order to keep the geometric delay constant for a particular reference position in the sky, another constantly adjusted delay τ_i is introduced in one of the signal paths, regardless of the fact that the receivers have a finite bandwidth and signals are averaged in time. This direction is referred to as the "phase reference center" $\vec{s_0}$. This final processed system response is then called "visibility" (see, e.g., Wilson et al., 2013, for a comprehensive overview). A typical radio interferometer ("array") is composed of spatially separated and often identical antennas and can be decomposed into several two-element interferometers. For an ideal interferometer the visibility $V_{jk}\left(u,v,w\right)$ depends on the sky brightness distribution, $I\left(l,m\right)$, according to

$$V_{jk}\left(u,v,w,t\right) = \iint\limits_{-\infty}^{\infty} I\left(l,m\right) \frac{\sqrt{A_j\left(l,m,t\right)A_k\left(l,m,t\right)}}{\sqrt{1-l^2-m^2}} e^{-2\pi i\left[ul+vm+w\left(\sqrt{1-l^2-m^2}-1\right)\right]} \mathrm{d}l\mathrm{d}m, \tag{3.1}$$

where l,m are the direction cosines in the plane of sky measured from the phase reference center with respect to the u,v axes, and $A_j\left(l,m,t\right)$ is the time-dependent reception pattern (“primary beam”) of antenna j. The baseline between antenna j and antenna k is projected into a coordinate system with the dimensionless components (u,v,w), where the u-component points to the east and the v-component points to the north. The (u, v)-plane is orthogonal to the direction of the phase reference center, i.e. the w-component of a baseline can be derived as

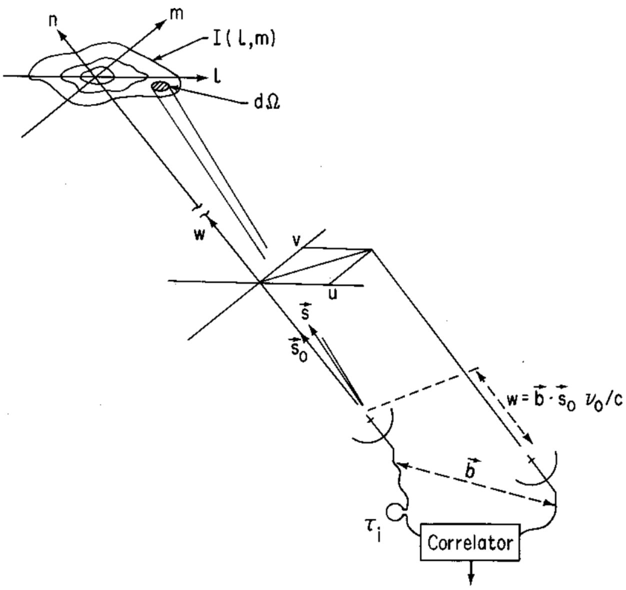

Figure 3.2: Sketch of the (l, m, n) and (u, v, w) coordinate systems in order to parameterize the baselines of the interferometer array and the sky brightness distribution with respect to the phase reference center, respectively. A surface element in the (l, m, n) coordinate system is denoted with $d\Omega$. The sketch is adapted from Taylor et al. (1999).

$$w = \frac{\vec{b} \cdot \vec{s}_0}{\lambda}, \tag{3.2}$$

where λ is the observational wavelength. An arbitrary direction in the sky is described in the (l, m, n) coordinate system of direction cosines, where $n = \sqrt{1 - l^2 - m^2}$. In Fig. 3.2 both coordinate systems are illustrated.

In case of a small FoV (l,$m \ll 1$) and a time-independent primary beam $A_j\,(l,m)$ close to the phase reference center, the relation between sky brightness distribution and visibility data becomes a Fourier transform $\mathcal{F}$

$$V_{jk}\,(u,v) \ \xleftrightarrow{\mathcal{F}} \ I\,(l,m)\,. \tag{3.3}$$

Since a real radio interferometer has a finite number of antennas, the (u,v)-plane is only sparsely sampled. In order to increase the coverage of the (u,v)-plane radio signals are integrated at different times, because the (u,v)-components of every baseline change with the hour angle H of the phase reference center, i.e. the (u,v) coordinate system rotates as earth rotates with time. This is called "earth rotation synthesis". Since $\bar{V}_{jk}\,(u,v) = V_{jk}\,(-u, -v)$, the maximal sampling of the (u,v)-plane is already achieved after 12 hours. Measuring at different wavelengths λ, e.g., with a large bandwidth or observing at more than one frequency, also helps to fill up the (u,v)-plane, see equation 3.2. To recover the sky brightness distribution it is assumed that the flux density of the radio emission is neither frequency nor time dependent. The (u,v)-plane sampling can be denoted with a function $B\,(u,v)$, which is 1 for (u,v)-coordinates whose visibilities are actually measured and 0 otherwise. This corresponds to masking the visibilities of a radio interferometer $V_{jk}\,(u,v)$ by the "uv-coverage" $B\,(u,v)$. The convolution theorem can be applied

$$V_{jk}\,(u,v) \cdot B\,(u,v) \quad \overset{\mathcal{F}}{\longleftrightarrow} \quad I\,(l,m) * \mathcal{B}\,(l,m)\,, \tag{3.4}$$

where the Fourier transform of the uv-coverage $\mathcal{B}\,(l,m)$ can be interpreted as the point spread function (PSF) of the radio interferometer, in the following denoted as "synthesized beam" or "dirty beam". Hence, the brightness distribution obtained after the Fourier transform is the convolution, indicated by $*$, of the true sky brightness distribution with the synthesized beam. Since a radio interferometer does not measure at baseline lengths of zero, the dirty image $(I\,(l,m) * \mathcal{B}\,(l,m))$ has also zero total flux.

The advantage of observing with a radio interferometer rather than with a single-dish telescope is to overcome the angular resolution limit Θ set by the single-dish aperture

$$\Theta \propto \frac{\lambda}{D}, \tag{3.5}$$

where D is the size of the aperture. In order to achieve a similar theoretical resolution as an optical telescope ($\lambda \sim 500\,\mathrm{nm}$) using a mirror with a diameter of 2 m one would need to build a radio dish with a size of $\sim 850\,\mathrm{km}$ if observing at $\lambda = 21\,\mathrm{cm}$. The "size of the aperture" of a radio interferometer is defined by the longest baseline. On the other hand, a radio interferometer is not sensitive to structures larger than

$$\theta_{\mathrm{max}} \sim \frac{1}{2u_{\mathrm{min}}} = \frac{\lambda}{2b_{\mathrm{min}}}, \tag{3.6}$$

where b_{min} is the length of the shortest baseline ("short spacing problem").

3.2 The WSRT 346 MHz Legacy Survey

3.2.1 The Westerbork Synthesis Radio Telescope

The WSRT is a radio interferometer located near the village Westerbork in the Netherlands. Its antennas are aligned along the east-west direction. The interferometer consists of 14 equatorially mounted parabolic dish antennas with a diameter of 25 meters each and is equipped with linear feeds ('X' and 'Y'). The equatorial mount and the source tracking capability of the array simplifies the reconstruction of the sky brightness distribution (see equation 3.1), since the resulting primary beam pattern is time-independent and identical for each pair of antennas. In Fig. 3.3 the configuration of the array is depicted[1]. Ten dishes have a fixed separation of 144 meters, while two remaining dish-pairs at the eastern end of the array are movable on 300 meter (first pair) and 100 meter (second pair) long railtracks. The shortest adjustable baseline is thus 36 meters whereas the longest baseline is fixed to 2.7 km. The WSRT is therefore able to operate with different shortest baselines, e.g., in the 36M (36 meter), the 60M (60 meter) and the 84M (84 meter) mode. Currently, the WSRT is equipped with different receivers measuring in wavelengths of $\lambda \sim 3.6 \ldots 92$ cm. According to equation 3.6, the largest angular scale recovered at a frequency of $\nu \sim 346$ MHz (P-band) is $40'$ for 36M, $24'$ for 60M, and $17'$ for 84M, respectively. The highest possible resolution according to equation 3.5 is about $1'$. Combining a target observation using those different array configurations allows one to fill the (u,v)-plane. The FoV due to primary beam attenuation ranges from $2.6°$ at $\lambda = 92$ cm down to $0.1°$ at $\lambda = 3.6$ cm.

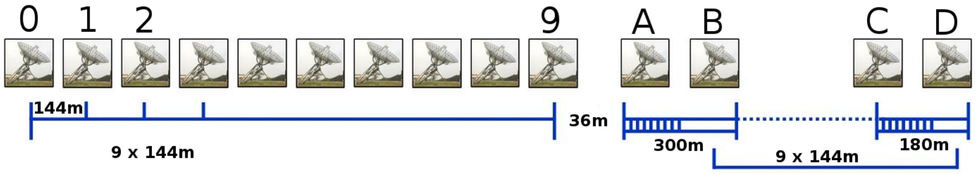

Figure 3.3: Geometry of the WSRT array[1].

Since the WSRT is a one-dimensional array it needs a 6 hour earth rotation synthesis observation to be sensitive to all spatial directions and a 12 hour earth rotation synthesis to maximize the uv-coverage. Every single antenna is able to be individually directed at any point on the sky. After each single integration the WSRT performs a measurement of a calibrated noise source at the receiver ("system temperature"). This

---

[1] www.astron.nl/radio-observatory/astronomers/wsrt-guide-observations/3-telescope-parameters-and-array-configuration

measurement helps to track the gain of the receiving unit with time and is used to correct for possible amplitude variations during the observational run.

3.2.2 The observational campaign

The WSRT Legacy Survey aimed for deep observations of the Milky Way, and a large sample of galaxies and galaxy clusters at low frequencies. Here, we present the observational campaign of the galaxy clusters part only. Ten galaxy clusters with already known diffuse radio sources and unclassified sources have been selected to study their morphology and flux density at low frequencies. All observations have been performed in between summer 2011 and spring 2012, before the P-band receivers of the WSRT were planned to be decommissioned in 2013. We observed every target for 36 h in P-band within the frequency range from 311 to 381 MHz, with a central frequency of 346 MHz and a spectral resolution of 78.125 kHz. Each observation of a galaxy cluster was carried out at three different nights with a duration of 12 h each, using a different array configuration (see Sec. 3.2.1 and the configuration column in Tab. 3.1). This allowed us to maximize the available uv-coverage. Details of all observations in the framework of the WSRT legacy survey are listed in Tab. 3.1. 3C 286 (for Abell 2319) and 3C 147 (for all the others) were observed for 15 min before the target observation for flux density scale and bandpass calibration.

3.3 Follow-up on target Abell 2069

3.3.1 The Giant Metrewave Radio Telescope

The GMRT is a radio interferometer located 10 km east of Narayangaon town on the Pune-Nasik highway in India[2]. The interferometer consists of 30 equatorially mounted parabolic antennas with a diameter of 45 meters each and is equipped with circular feeds ('R' and 'L' for right-handed and left-handed polarization, respectively). The array is specialized in observing in the meter wavelength regime. In particular, the GMRT is equipped with receivers for observing at frequencies of 50, 153, 233, 322, 608, and 1420 MHz. At such low frequencies it is necessary to provide longer baselines in order to resolve structures down to a scale of several arcseconds. In Fig. 3.4 the configuration of the array is depicted[3]. The array consists of a compact central array, where 14 out of 30 antennas are randomly distributed within an area of about 1 km^2. This compact core is complemented by an approximately 'Y'-shaped configuration,

---

[2] http://www.gmrt.ncra.tifr.res.in/gmrt_hpage/GMRT/intro_gmrt.html

[3] http://www.gmrt.ncra.tifr.res.in/gmrt_hpage/Images/Diagrams/gmrtarraya.gif

Table 3.1: The WSRT 346 MHz Legacy Survey: Observational details. All observations have been performed in the frequency range from 311 to 381 MHz and with an exposure time of 12 hours.

Source	Pointing center RA/DEC (J2000)	Date	Configuration
A115	00h55m59.5s $+26^\circ19'13.9''$	03/04-October-2011	36M
		10/11-October-2011	60M
		05/06-October-2011	84M
A1240	11h23m32.0s $+43^\circ06'30.1''$	27/28-March-2012	36M
		10/11-April-2012	60M
		03/04-April-2012	84M
A1758	13h32m32.1s $+50^\circ30'37.0''$	26/27-March-2012	36M
		11/12-April-2012	60M
		04/05-April-2012	84M
A2061	15h21m20.6s $+30^\circ40'15.3''$	25/26-April-2012	36M
		08/09-May-2012	60M
		14/15-May-2012	84M
A2069	15h23m57.9s $+29^\circ53'26.0''$	26/27-April-2012	36M
		09/10-May-2012	60M
		16/17-May-2012	84M
A2218	16h35m54.0s $+66^\circ13'00.0''$	24/25-June-2011	36M
		01/02-July-2011	60M
		08/09-July-2011	84M
A2219	16h40m22.1s $+46^\circ42'20.0''$	25/26-June-2011	36M
		02/03-July-2011	60M
		09/10-July-2011	84M
A2254	17h17m45.9s $+19^\circ40'22.8''$	27/28-June-2011	36M
		03/04-July-2011	60M
		10/11-July-2011	84M
A2319	19h20m45.3s $+43^\circ57'42.9''$	01/02-August-2011	36M
		02/03-August-2011	60M
		03/04-August-2011	84M
RXJ1053	10h53m44.4s $+54^\circ52'21.1''$	18/19-January-2012	36M
		25/26-January-2012	60M
		15/16-February-2012	84M

Notes. The label of the WSRT configuration is named according to the distance of antenna 9 and A in meters.

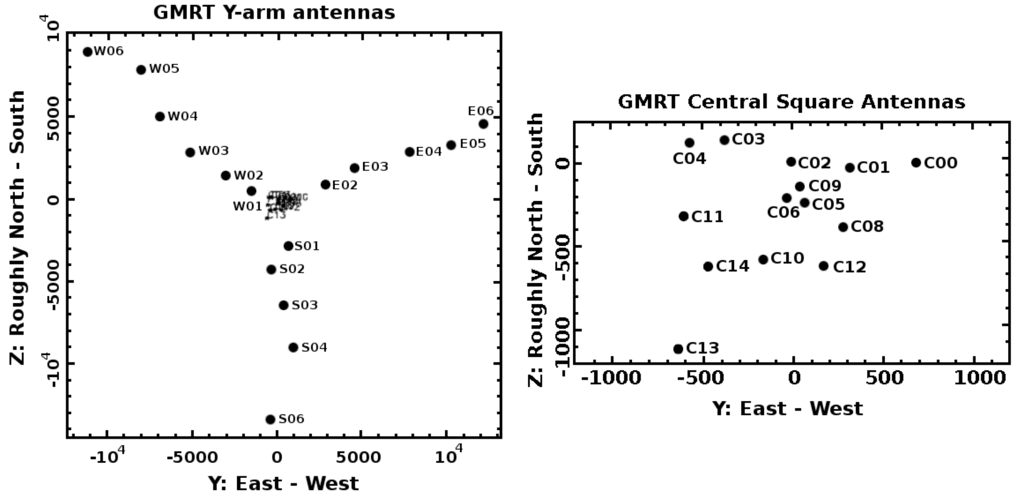

Figure 3.4: *Left panel:* Configuration of the GMRT array. *Right panel:* Zoom into the core of the GMRT array.

where the remaining 16 antennas are placed. After 6 hours of observation redundant information is recorded. The longest interferometric baseline in between the arms of the 'Y' has a length of ∼25 km.

With the shortest baseline of ∼50 meters the largest angular scale recovered is $\sim 32'$ at 322 MHz and $\sim 16'$ at 608 MHz, whereas the highest possible resolution is $\sim 8''$ at 322 MHz and $\sim 4''$ at 608 MHz. Thus, the GMRT provides a much higher resolution at 346 MHz than the WSRT which is useful in discriminating compact sources from the diffuse radio emission. The sensitivity of the GMRT to large scale diffuse radio emission is comparable to the sensitivity of the WSRT, but the short baselines of the GMRT are often affected by strong RFI at frequencies of 320 MHz and lower.

3.3.2 The Low Frequency Array

The LOFAR is a novel radio telescope (see also van Haarlem et al., 2013, for a review) and a big leap forward in terms of sensitivity for diffuse radio sources at very low frequencies. The LOFAR telescope observes in the largely unexplored frequency range from 10 to 80 MHz using the Low Band Antennas (LBA) and from 110 to 240 MHz using the HBA. It is a pathfinder instrument for the Square Kilometre Array (SKA)[4]. Instead of having large dishes it consists of simple dipole antennas grouped into stations. The LOFAR stations are located at different sites in the Netherlands and in other countries of Europe. LOFAR consists of 24 "core stations" (denoted with

---

[4] https://www.skatelescope.org/uploaded/31558_SKA_GWP_2012_lr.pdf

CS), 14 "remote stations" (denoted with **RS**), and 13 international stations. The core stations are located near the village Exloo in the Province Drenthe[5] and consist of two 24-element HBA fields with a diameter of 30.8 m each and one 96-element LBA field with a diameter of 87 m diameter[6], see left sketch of Fig. 3.5. They form a compact array distributed in an area with a diameter of 2 to 3 km. The densest part of LOFAR is realized with the "superterp", hosting seven core stations placed adjacent to each other. In the current state of the telescope, the core of the LOFAR HBA is already twice as sensitive as the GMRT at 150 MHz at an intermediate resolution ($\sim$ 25 arcsec). To resolve structures at a scale of several arcseconds at such a low frequency the remote stations are located at a distance of up to $\sim$ 100 km from the core. The HBA array of the remote stations consists of 48 elements. Thanks to the extension of LOFAR to Germany (6 stations), Poland (3 stations), France, Sweden, the United Kingdom, and Ireland (1 station each) LOFAR can serve as a homogeneous Very Long Baseline Interferometry (VLBI) instrument, with baselines larger than $\sim$ 1000 km, reaching subarcsecond resolution at a central frequency of 150 MHz. For the international stations, the HBA fields are twice the size of the remote stations to

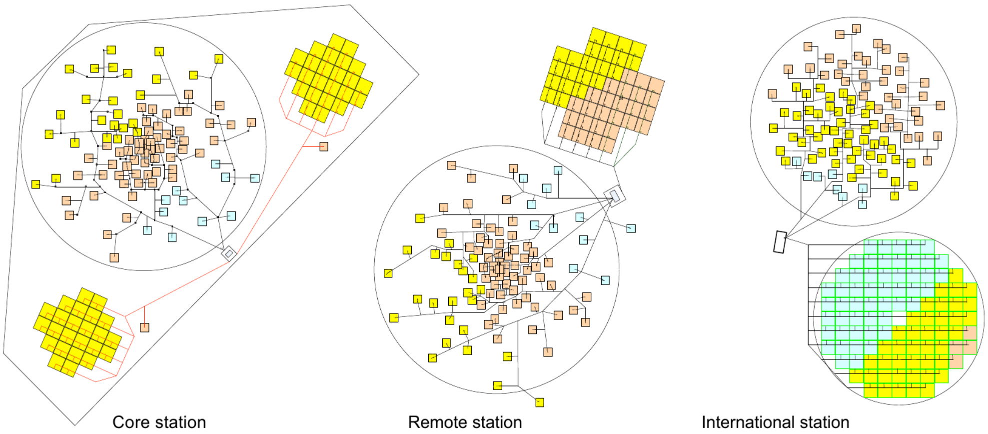

Figure 3.5: Sketches of the LOFAR station layouts showing core, remote and international stations (from left to right). The LBA dipoles are within the area indicated with a large circle. The small squares beyond the large circle indicate the HBA tiles. The different colors of the elements refer to different cable lengths each element is connected with. A larger version of this image including tile and antenna numbers is shown in App. A.

---

[5] http://www.lofar.org/about-lofar/general-information/location-lofar/location-lofar

[6] https://www.astron.nl/radio-observatory/astronomers/users/technical-information/lofar-stations/lofar-stations-description-

increase sensitivity for the very long baselines. In total, LOFAR comprises more than 100,000 dipoles distributed over Europe.

Each station operates as a phased array, i.e. the beam and the direction of the beam is set by delays when combining the signals of the individual dipoles ("beamforming"). This technique allows LOFAR to observe in more than one direction at the same time. The station beam corresponds to the primary beam. The beam-formed data are sent from each station to a central correlator (currently the Correlator and Beamforming Application platform for the Lofar Telescope (COBALT)) via fast fiber connections (10 Gbit/s for each station). The total number of visibilities N_V produced by the correlator is

$$N_V = N_{\mathrm{pol}} \times \frac{N_{\mathrm{a}}\,(N_{\mathrm{a}} - 1)}{2} \times N_n \times N_k, \tag{3.7}$$

with N_{pol} the number of polarizations, N_{a} the number of stations, N_n the number of integration time steps, and N_k the number of frequency channels. According to equation 3.7 this implies a total of 10^{13} complex visibilities. This corresponds to a data volume of the order of 100 TByte to be stored and further processed for one typical LOFAR observation of 12 hours that includes all available stations. LOFAR is a radio telescope of high flexibility, only limited by the software, data links and computational resources. This is reflected by the variety of scientific fields covered by LOFAR, e.g., Epoch of Reionization (EoR) (Zaroubi et al., 2012), cosmic magnetism (Anderson et al., 2012), transient sources (Stewart et al., 2016), Solar science and space weather (e.g., Morosan et al., 2014), cosmic rays (Buitink et al., 2016), pulsars (Pilia et al., 2016), and deep extragalactic surveys.

Low Band Antennas

The LBA operate at the lowest end of the ionospheric window from 10 to 80 MHz, but they mainly observe in the frequency range from 30 to 80 MHz due to strong RFI at very low frequencies. LBA elements are constructed out of two orthogonal copper wires serving as dipoles receiving two orthogonal linear polarizations. A metal grid on the ground serves as reflector for the dipoles. An image of a single LBA is depicted in the left panel of Fig. 3.6. The design of the LBA elements causes a strongly peaked bandpass close to the resonance frequency of the single dipole (see right panel of Fig. 3.6) around 60 MHz[7]. Furthermore, the single element is sensitive to the entire sky, but its sensitivity significantly drops below about 30° in elevation. The typical

---

[7] https://www.astron.nl/radio-observatory/astronomers/lofar-imaging-capabilities-sensitivity/sensitivity-lofar-array/sensiti

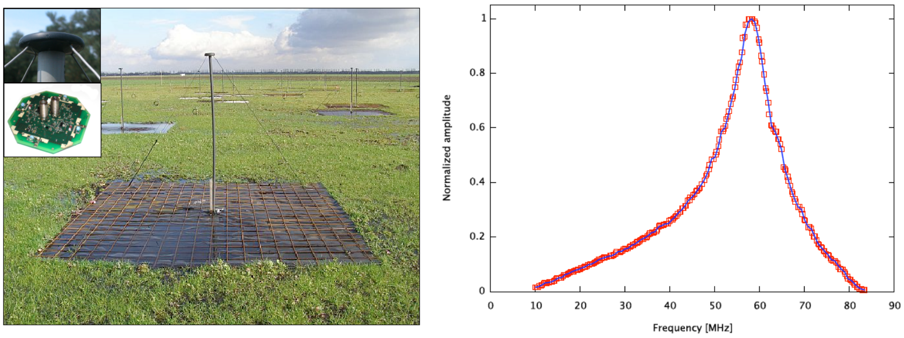

Figure 3.6: *Left panel:* Image of a single LBA dipole including the ground plane. *Right panel:* Bandpass of a single LBA dipole in the frequency range between 10 and 80 MHz. Both images are adapted from van Haarlem et al. (2013).

size of the LBA station beam is ∼7.5° at 50 MHz (Falcke et al., 2007).

High Band Antennas

The HBA are assembled in blocks of 24, 48, or 96 tiles. Each tile consists of a 4×4 dual-polarization antenna grid. The antenna elements are supported by the expanded polystyrene structure of the tiles. The HBA tiles are more fragile than the LBA elements and thus protected by covers from weather damage (see left panel of Fig. 3.7). For a given direction in the sky the signals of this grid elements are formed into a "tile beam". This beam limits the FoV of an individual tile to ∼30° at a frequency of 150 MHz. This is important to take into account when conducting a multibeam observation.

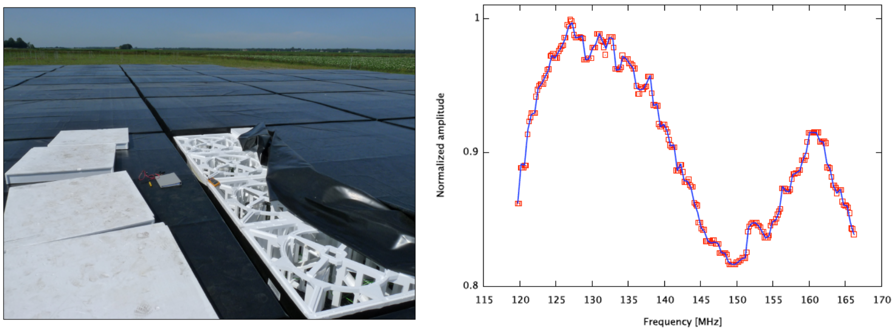

Figure 3.7: *Left panel:* Closeup image of a single HBA tile after removing parts of the protective cover. *Right panel:* Bandpass of a single HBA dipole in the frequency range between 120 and 165 MHz. Both images are adapted from van Haarlem et al. (2013).

In contrast with the LBA the HBA show a rather flat bandpass (see right panel of Fig. 3.7), in case of a low noise environment it is easy to make use of the whole bandwidth. The typical size of the HBA station beam is ∼3° at 150 MHz (Falcke et al., 2007).

3.3.3 Observational overview for the target Abell 2069

Since the galaxy cluster Abell 2069 was of particular interest, we additionally observed Abell 2069 with the GMRT for 4.8 hours. The observation was conducted in two different frequency ranges, one from 306 to 339 MHz (central frequency of 322 MHz and spectral resolution of 130.208 kHz) and the other from 591 to 625 MHz (central frequency of 608 MHz and spectral resolution of kHz). Furthermore, the galaxy cluster was observed with the LOFAR HBA in the frequency range from 117 MHz to 190 MHz (central frequency of 153 MHz and spectral resolution of 48.8 kHz after preprocessing, see Sec. 3.6.1) for 9.6 hours using 46 core stations and 14 remote stations. Details of all observations are listed in Tab. 3.2. 3C147 (WSRT) and 3C286 (GMRT / LOFAR HBA) were observed for 15 minutes (10 minutes) before and after the target observation for flux density calibration (see Tab. 3.3).

Table 3.2: Details of the WSRT 346 MHz and its follow-up observations. For the WSRT label see Tab. 3.1.

Telescope	Pointing center RA/DEC (J2000)	Frequency [MHz]	Exposure time [h]	Date	Configuration
WSRT	15h23m57.9s $+29^\circ 53' 26.0''$	311-381 MHz	12.0	26/27-April-2012	36M
				09/10-May-2012	60M
				16/17-May-2012	84M
GMRT	15h24m08.0s $+29^\circ 52' 55.0''$	306-339 MHz	4.8	30-May-2014	–
		591-625 MHz		10-June-2014	–
LOFAR HBA	15h23m57.9s $+29^\circ 53' 26.0''$	117-190 MHz	9.6	08/09-May-2014	–

Table 3.3: Flux density scale calibrators used for each telescope.

Telescope	Calibrator ID	Exposure time [min]
WSRT	3C147	15
GMRT	3C286	15
LOFAR HBA	3C286	10

3.4 Basics of image reconstruction and calibration

In order to restore the true sky brightness distribution of equation 3.4 one needs to "deconvolve" the initially obtained image, also called "dirty image". A standard deconvolution scheme is the `CLEAN` algorithm (Högbom, 1974; Clark, 1980). `CLEAN` operates in the image plane and identifies the brightest pixel. The pixel location and the flux density of the pixel is added to the `CLEAN` component model. The `CLEAN` component model represents a point-source model of the true sky brightness distribution. The components of the `CLEAN` model are then convolved with the synthesized beam and subtracted from the image. In the next iterations this step is repeated with the residual images, obtained from subtracting the next brightest pixels convolved with the synthesized beam. This procedure continuously adds total flux to the restored image with every iteration. The `CLEAN` version by Schwab (1984) is interleaving this scheme (referred to as "minor cycles") with "major cycles" in which the `CLEAN` component model is transformed to visibility space and then subtracted from the visibilities. The new residual image is then generated by transforming the residual visibilities back to image space. Hence, the deconvolution is already a complex process in which the image needs to be computed from the visibilities many times. When `CLEAN` has finished after a fixed number of iterations or through a previously defined threshold, the restored radio map is created out of the residual image and the `CLEAN`-component model

$$\text{restored image} = \texttt{CLEAN}\text{-model} * \text{restoring beam} + \text{residual image}, \tag{3.8}$$

where the restoring beam is a two-dimensional elliptical Gaussian. Convolving with the restoring beam removes the sidelobes of the dirty beam in the image. Its semi-major and semi-minor axes are derived from the full width at half maximum (FWHM) of the synthesized beam. The restored image only represents one possible interpretation of the visibilities and should thus be treated as an estimate of the true sky brightness distribution. The maximum angular resolution of the restored image according to equation 3.5 is defined by the *uv*-coverage of the observation and the chosen weighting scheme within the `CLEAN` algorithm. The weighting scheme corresponds to a multiplication of a weighting function $W\,(u,v)$ with the *uv*-coverage $B\,(u,v)$ in order to modify the dirty beam, see equation 3.4. The "natural weighting" scheme puts equal weights to all samples. Since lower spatial frequencies are usually sampled better, they get a higher weighting. This leads to a larger dirty beam (lowered resolution) and maximum peak sensitivity. The "uniform weighting" puts equal weights on each spatial frequency regardless of the sample density. This suppresses the sidelobes of the dirty beam and narrows down the dirty beam. The peak sensitivity is significantly lower compared to images achieved with natural weighting applied. The Briggs robust weighting offers a compromise between maximizing the peak sensitivity and suppressing the sidelobes of the dirty beam (Briggs, 1995) and is thus commonly used.

In practice, a radio interferometer only measures the visibilities of a radio signal received at the detectors and processed through the observing system

$$\tilde{V}_{jk}\left(u,v\right) = J_{jk} V_{jk}\left(u,v\right), \tag{3.9}$$

where the operator J_{jk} represents the net effect of all modifications of the radio signal before it is actually recorded. Inverting the matrix $\hat{J}$ is called "calibration". Typically, calibration aims to correct the total flux density scale, the instrumental bandpass as well as time and frequency dependent phase deviations between the antennas. Especially at low frequencies $\nu \ll 1\,\mathrm{GHz}$, the earth's ionosphere introduces phase delays to the radio signals. Sometimes $\hat{J}$ corrupts the received signal irreversibly, e.g., in case of strong RFI. Those affected visibilities often need to be removed ("flagged"). In order to reliably determine proper calibration parameters, a reasonable a-priori model of the true sky brightness distribution is needed. That's why observations of radio sources of known flux density and shape ("calibrator") are typically performed together with the target observations. If a skymodel is extracted from the reconstructed sky brightness distribution the inversion of equation 3.9 is referred to as "self-calibration".

3.5 Calibration and imaging strategy for the WSRT Legacy Survey

Before starting the calibration procedure we performed RFI excision. We used the automatic statistical flagging algorithm `AOFlagger` (Offringa, 2010), which has been developed originally for the use with LOFAR data. Since we have observed with the WSRT and the GMRT at a different wavelength regime and with a different time and frequency resolution than with LOFAR, we modified the default strategy of the `AOFlagger`. Unfortunately, in the GMRT observation all baselines shorter than about 1 500 meters were heavily affected by RFI. A total of 30% of the WSRT data and 40% of the GMRT data have been flagged.

Calibration, imaging, and self-calibration were carried out with the Common Astronomy Software Applications (CASA)[8] package. This software package is optimized to process VLA data. Since the WSRT and the GMRT are telescopes of similar design, this package suits all needs to properly process the data. For the WSRT we have corrected for amplitude variations based on the system temperature information recorded during the observations. We used the calibrator observations of 3C147 and 3C286 to correct for the bandpass and flux density scale according to Scaife and Heald (2012). Because of the excellent phase stability of the WSRT backend, a few iterations of self-calibration were sufficient to correct for remaining phase variations. We carried out the initial phase calibration for the GMRT data with a skymodel based on positions in the Faint Images of the Radio Sky at Twenty-Centimeters (FIRST) catalog (Becker et al., 2012), using 36 sources that contribute most to the visibilities. For self-calibration and imaging, we applied Briggs weighting with a robust parameter of 0.0 in CASA, which offers a compromise between high-resolution and the best signal-to-noise ratio (SNR) per beam. With the final calibrated data we achieve a root mean square (rms) noise level of about 0.5 mJy beam^{-1} for the WSRT images with a $108'' \times 52''$-beam, and 0.2 mJy beam^{-1} for the GMRT images with a $14'' \times 7''$-beam.

Throughout our flux density I measurements we assume a flux density scale uncertainty f_{scale} of 5% for 3C147 and 2.5% for 3C286 according to Scaife and Heald (2012). All errors take into account noise uncertainties based on the rms level of the radio maps σ_{rms}. Since we could not correct for system temperature variations of the GMRT, we adopt an average amplitude instability f_{inst} of 10%. The total error of all flux density measurements ΔI, including the case of subtracted sources in the region of measurement, is then given by

$$\Delta I = \sqrt{(f_{\mathrm{scale}} \cdot I)^2 + \left(\sigma_{\mathrm{rms}} \cdot \sqrt{N_{\mathrm{beam}}}\right)^2 + (f_{\mathrm{inst}} \cdot I)^2 + (f_{\mathrm{subtr}} \cdot I_{\mathrm{subtr}})^2}, \qquad (3.10)$$

where N_{beams} is the number of beams needed to measure the integrated flux density, $f_{\mathrm{subtr}} = 10\%$ is the subtraction uncertainty, and I_{subtr} is the amount of subtracted flux density.

3.6 Calibration and imaging the LOFAR data

3.6.1 Special challenges with LOFAR

Since LOFAR uses a phased array fixed to the ground out of simple antenna dipoles, non-standard techniques for the data reduction are needed. The biggest challenges

---

[8] http://casa.nrao.edu/

for a proper LOFAR data reduction remain in dealing with the huge data volume, the large FoV, the strong sidelobes of the synthesized beam, and the severe impact of the ionosphere on radio signals at very low frequencies. To prevent visibility data from being decorrelated, LOFAR initially observes in the interferometric mode with a time resolution of 1 second and a frequency resolution of 768 Hz. The standard preprocessing consists of flagging (with the `AOFlagger`), `demixing` (van der Tol et al., 2007) and averaging the data in frequency and time to be more handy for further processing.

`Demixing` is an algorithm that subtracts bright radio sources that are not the actual target of the observation. Especially, the radio signal of the so-called "A-team" sources (Cassopeia A, Cygnus A, Virgo A, Herkules A, and Virgo A), a group of the brightest radio sources (total flux density $\gtrsim 1\,\mathrm{kJy}$) in the northern hemisphere, can severely affect the recorded visibilities if they accidently reside in a sidelobe of the primary beam.

The large FoV of LOFAR at low frequencies prohibits ignoring the w-term in equation 3.1. Furthermore, the station beam $A_j\,(l,m,t)$ and the polarization properties of LOFAR depend on the pointing direction (in elevation) and on the location of the station. They vary with frequency as well as with time when tracking a source on the sky. To reconstruct the sky brightness distribution, a simple Fourier transform of the visibility data as mentioned in equation 3.4 does not work in the case of LOFAR. Equation 3.1 shows that the w-term as well as the A-term can be seen as an additional kernel of a two-dimensional Fourier transform (Cornwell et al., 2008; Bhatnagar et al., 2008). A combined treatment of the w-term and the A-term in the image plane is called Aw-projection. A dedicated imager for LOFAR implementing the Aw-projection is the `awimager` by Tasse et al. (2013).

The cosmic radio signals are severely influenced by the Earth's ionosphere before reaching the telescope at the ground at the low frequencies LOFAR is observing. The most dominant effects are frequency-dependent propagation delays, which cause a phase rotation ϕ_{ion} and Faraday rotation (see, e.g., Intema et al., 2009; Sotomayor-Beltran et al., 2013). The ionospheric delay of a particular LOFAR station τ_{ion} depends on the free electron density n_{e^-} integrated over the LoS through the ionosphere (the total electron content (TEC)) in such a way that

$$\tau_{\mathrm{ion}} = \left|\frac{\partial \phi_{\mathrm{ion}}}{\partial \nu}\right| = \frac{q^2}{4\pi\varepsilon_0 m_{\mathrm{e}^-} c \nu^2} \int\limits_{\mathrm{LoS}} n_{\mathrm{e}^-} dl \propto \frac{\mathrm{TEC}}{\nu^2}, \tag{3.11}$$

where q is the elementary charge, m_{e} is the electron mass, and ε_0 the vacuum permittivity. The LOFAR telescope operates in the Lonsdale regime 4 (Lonsdale, 2005), see Fig. 3.8, when using remote stations or even international stations. This means that the ionospheric delay depends on antenna position and viewing direction. A simple calibration, see equation 3.9, can only be done in one direction of the sky, preferably the phase reference center. To account for the directional dependency of the phase variations, a technique that corrects for phases that vary over the entire FoV of each station, is required. Up to now a variety of techniques and tools, e.g., "peeling" (Noordam, 2004), `SPAM` (Intema, 2014) or `LOFAR facet calibration` (van Weeren et al., 2016b) (see also Sec. 3.6.3) have been developed.

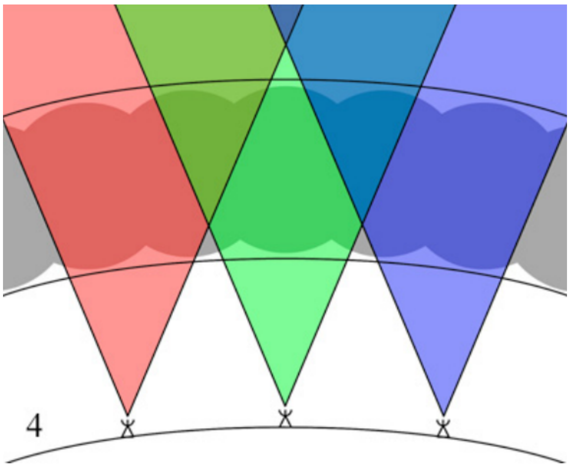

Figure 3.8: Scheme of the Lonsdale regime 4 adapted from Intema et al. (2009). The array is represented by three antennas at ground level when looking through different parts of the ionosphere (grey clouds) with individual FoVs (red, green and blue areas).

Additionally, the remote stations don't run on the same clock as the core stations. Clock offsets introduce a frequency-independent delay τ_{clock}. The total delay τ that needs to be corrected for is

$$\tau = \tau_{\text{clock}} + \tau_{\text{ion}}. \tag{3.12}$$

The procedure to disentangle both delays during the calibration is called "clock-TEC separation".

3.6.2 Direction-independent calibration and imaging

Before performing any direction-dependent calibration it is necessary to obtain a fairly reasonable sky model of the target field. To achieve this, we started with basic direction-independent calibration. LOFAR data are split into single subbands of

~ 0.2 MHz. The calibrator observation of 3C286 was used to correct for the flux density scale of each single subband. That's why there is no need for a dedicated bandpass calibration. Furthermore, cross-polarization phase offset correction and clock-TEC separation was performed. Since the clock delay is direction-independent, this allows us to already transfer the solutions of the clock delay to the target observation. The effect of the clock delay of the remote stations is illustrated in the left image of Fig. 3.9. Since the phase solutions are colorcoded the frequency-dependent (y-axis) phase drift is visibile as horizontal stripes, indicating the presence of several phase wraps across the whole band. The right image of Fig. 3.9 presents the derived clock solutions from the clock-TEC separation with time. In our observation the clock delay ranges from -100 ns to $+100$ ns. This leads to up to eight phase wraps within the full bandwidth.

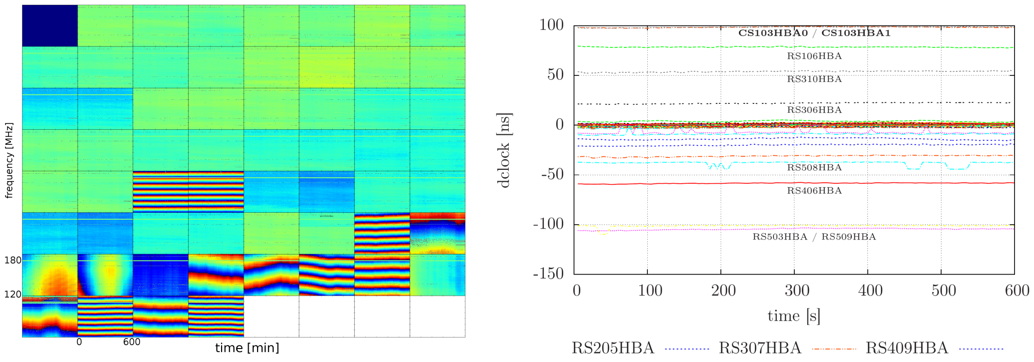

Figure 3.9: *Left panel:* Station based frequency versus time matrix of the colorcoded phase solutions in XX polarization of the HBA calibrator observation of 3C286. The phase reference station is CS001HBA0. The station CS013HBA shows a clear frequency-dependent phase pattern indicating a non-zero clock delay. A larger image and the station names are shown in App. B. *Right panel:* Extracted clock delay for each station. Stations with significant offsets are labeled.

The large FoV and the sidelobes of the LOFAR primary beam make the observation susceptible to strong sources in the vicinity of the pointing. In the case of our observation of Abell 2069 all very bright radio sources are at a well-tolerated angular separation: Cassopeia A ($\approx 78°$), Cassopeia A ($\approx 55°$), Taurus A ($\approx 119°$), Hercules A ($\approx 32°$), and Virgo A ($\approx 44°$). Thus we simulated the expected impact of these sources on the data using the common LOFAR beam model and flagged all affected data above a threshold of 5 Jy at 153 MHz.

Then we applied the flux density scale and the the clock solutions derived from our calibrator observation to the target field. An initial direction-independent phase calibration was performed on the target field using the global sky model (GSM). The

GSM is a database that contains source locations and spectral indices derived from the VLA Low-Frequency Sky Survey (VLSS) (Cohen et al., 2007), Westerbork Northern Sky Survey (WENSS) (de Bruyn et al., 2000), and NVSS (Condon et al., 1998) catalogs. Therefore, a dedicated phase calibrator observation to track phase variations during the observations is not needed. We used `LOFAR solutions tool (LoSoTo)`[9] to reject outliers in the calibrator solutions as well as for smoothing and displaying the calibration solutions. We have flagged the stations CS006HBA0 and CS006HBA1, the frequency regime between 169.65 - 169.85 MHz and 177.46 - 179.22 MHz as well as the last 30 minutes of our observation completely due to bad calibration results. Afterwards, we concatenated our data (370 subbands) into 37 chunks of ten subbands each and imaged the full FoV using the `awimager`. This translates to images of a bandwidth of 2 MHz. From each of these images we extracted a skymodel using the Python Blob Detection and Source Measurement (PyBDSM) (Mohan and Rafferty, 2015) package. We have then rerun the initial direction-independent phase calibration on every data chunk individually with its corresponding PyBDSM skymodel. This has improved the calibration results significantly (see Fig. 3.10). With this step we finished the direction-independent part of the calibration.

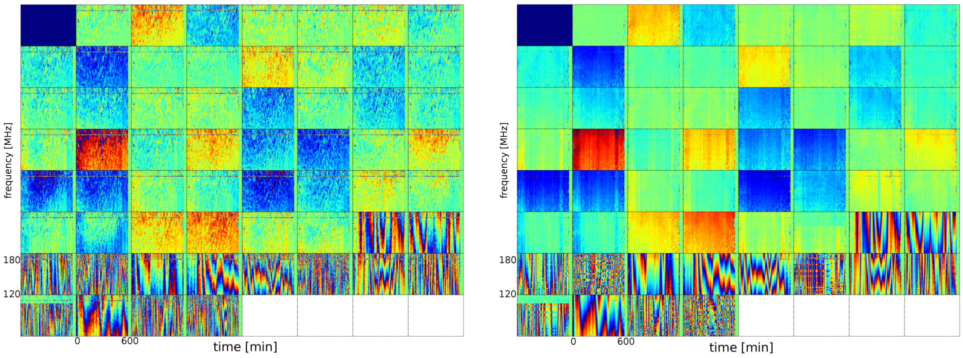

Figure 3.10: *Left panel:* Station based frequency versus time matrix of the colorcoded phase solutions in XX polarization of the HBA target observation of Abell 2069 using the GSM. The phase reference station is CS001HBA0. *Right panel:* The same as left panel using a PyBDSM extracted skymodel. A larger image and the station names are shown in App. B.

The procedure described in this section has been implemented in the `LOFAR pre-facet calibration pipeline (prefactor)`[10]. Nevertheless, the radio map obtained with this basic strategy has only limited fidelity and a noise level of about a factor 5

---

[9] https://github.com/revoltek/losoto

[10] https://github.com/lofar-astron/prefactor

to 10 higher than the expected thermal noise of the instrument.

3.6.3 Facet calibration

`Facet Calibration for LOFAR (factor)` is a new tool which is applying the facet calibration strategy (see van Weeren et al., 2016b, for a more detailed description) to LOFAR data in a semi-automated fashion. It is still under development and dedicated to properly handle the special calibration challenges of LOFAR using a minimum amount of free parameters to calibrate for. It assumes that ionospheric disturbances and an improper modelling of the station beams are the main cause of the artifacts remaining in the radio maps achieved from direction-independent calibrated data. The ionosphere and inevitably the phases can vary on short timescales, usually from a couple of seconds up to half a minute, whereas the station beams, leading to amplitude variations, vary slowly with time and frequency and therefore can be calibrated on solution intervals between ~ 5 and ~ 30 minutes. `factor` assumes that all direction-dependent effects vary slowly across the FoV.

These assumptions allows one to tile the sky into facets in which the effects of the varying beam and the phase distortions due to the ionosphere are small. The sky is partitioned via a Voronoi tessellation scheme (Okabe, 2000) according to the directions of suitable calibrators, usually bright sources or groups of bright sources. The calibrators should be sufficiently bright to calibrate for the amplitudes and phases at the needed time resolution. The calibration results of the calibrators are then applied to the entire facet.

Before running `factor` the direction-independent calibrated data has to be processed as follows: First, each frequency chunk of the direction-independent calibrated data is imaged independently at medium resolution ($\approx 25''$) with a FoV radius of $\sim 7°$. The resulting clean component model is subtracted from the target data. This data is then reimaged at low resolution ($\approx 75''$) with a FoV radius of $\sim 15°$ to also recover and subtract more extended sources as well as bright sources beyond the FWHM of the LOFAR primary beam.

Finally, we are left with 37 basically "empty" data sets and a skymodel for each frequency chunk which now serves as an input for the faceting. In the field of Abell 2069 `factor` selected 20 calibrator fields with a combined flux density of $\gtrsim 0.3$ Jy from the skymodels. The facet layout of the Abell 2069 field is depicted in Fig. 3.11.

Now the full bandwidth data is phase shifted to the direction of the first calibrator field and all clean components of the calibrator field are added back. The self-calibration of the calibrator field is then performed iteratively, beginning with a phase

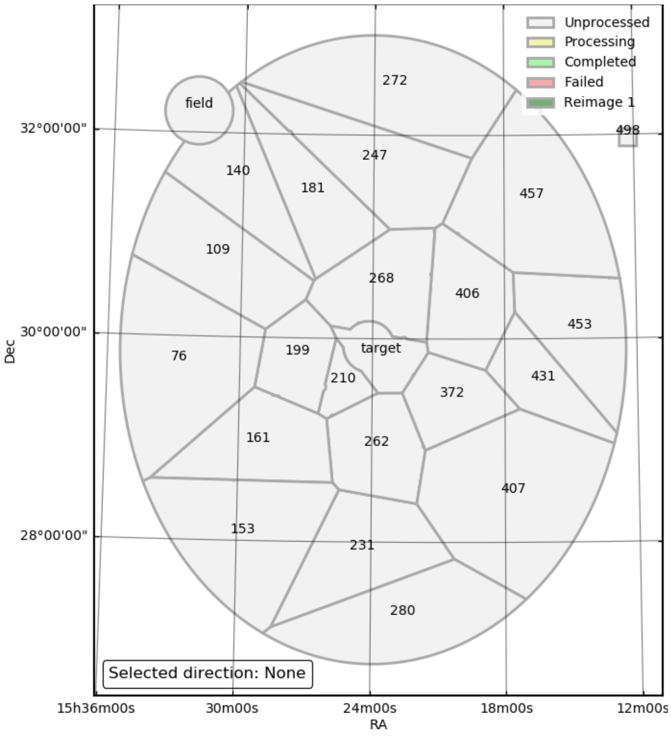

Figure 3.11: Facet layout of the full bandwidth `factor` run of the LOFAR HBA observation of Abell 2069.

self-calibration and finishing with phase and amplitude self-calibration. Each iteration is repeated until the background noise level converges. Fig. 3.12 illustrates the main steps of the self-calibration process for the calibrator field in the facet #109.

Once the first facet is finished, the skymodels are updated, and the improved sources are subtracted again. The calibration continues with the facet of the next brightest calibrator field until the whole sky is calibrated. Fig. 3.13 compares the same facet in the Abell 2069 field before (*left panel*) and after (*right panel*) facet calibration. Although the calibration did not run perfectly, which is recognizable by the “negative” valley surrounding the calibrator, the noise level decreased and the image provides a significantly higher fidelity. Facet calibration is able to reduce the noise by a factor of 4 at comparable resolutions if the self-calibration procedure performs well.. The thermal noise of this kind of LOFAR observation is about $\lesssim 100\mu\mathrm{Jy}$ at a resolution scale of $\sim 5''$.

Once all facets have been calibrated, they are imaged again with the direction-dependend solutions applied and assembled into an image mosaic. The outcome is very promising and represents a proof of concept how to deal with the severe direction-

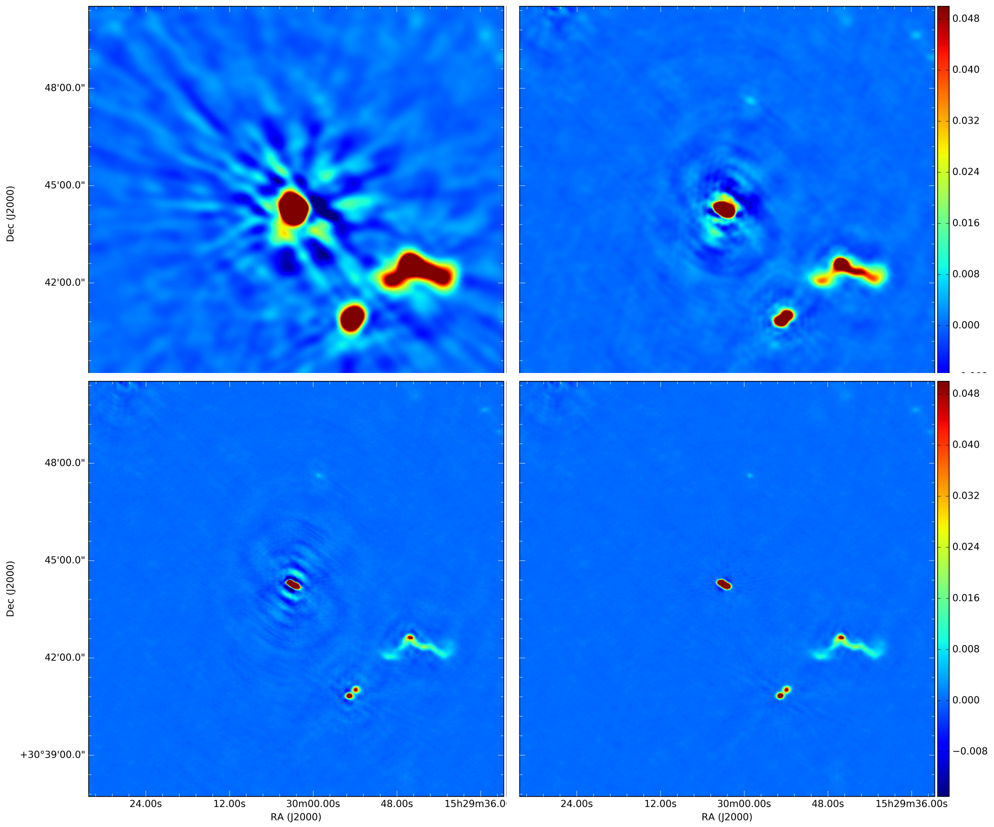

Figure 3.12: Images of a calibrator field during the direction-dependent self-calibration cycles using the full bandwidth of the observation. *From upper left to bottom right:* Initial image from direction-indepedent calibration (beam: 24″× 23″, position angle: 66°, $\sigma_{\rm rms} \approx 1.0\,\mathrm{mJy\,beam^{-1}}$), first TEC + phase calibration (beam: 16″× 13″, position angle: 88°, $\sigma_{\rm rms} \approx 320\,\mathrm{\mu Jy\,beam^{-1}}$), second TEC + phase calibration (beam: 7″× 5″, position angle: 100°, $\sigma_{\rm rms} \approx 180\,\mathrm{\mu Jy\,beam^{-1}}$), TEC + phase + slow amplitude calibration ($\sigma_{\rm rms} \approx 160\,\mathrm{\mu Jy\,beam^{-1}}$). The colorscale is in units of Jy beam^{-1}.

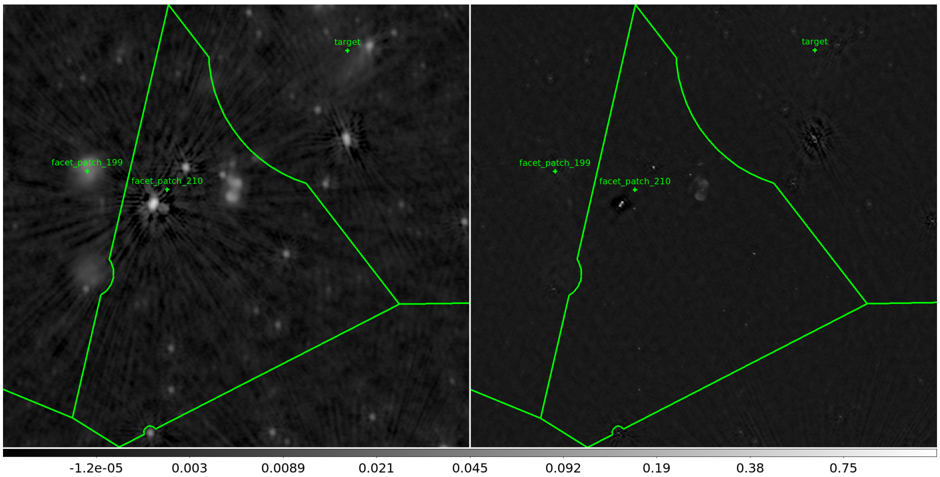

Figure 3.13: Direct comparison of the direction-independent radio map (*left panel*, beam: $28'' \times 24''$, position angle: $46°$, $\sigma_{\rm rms} \approx 450\,\mu$Jy beam^{-1}) with the direction-dependent radio map (*right panel*, beam: $7'' \times 5''$, position angle: $100°$, $\sigma_{\rm rms} \approx 180\,\mu$Jy beam^{-1}) of the `facet_patch_210`.

dependent distortions. `factor` is intended to be the main tool for the calibration of LOFAR HBA data..

3.7 X-ray data analysis

With X-ray telescopes like Chandra we can track the thermal bremsstrahlung of the hot ICM. In this work we took archival Chandra data and used the Chandra analysis software Chandra Interactive Analysis of Observations (CIAO) 4.6 as well as Chandra Calibration Database (CALDB) 4.5.9 for the data reduction. The exposure-corrected images are created with the task `fluximage` and `merge_obs` if more than one observation is available. In order to properly minimize point source contamination when measuring X-ray flux densities in the Chandra images, a reprocessing is needed. To identify point sources the exposure-corrected image is not binned. We then determine the size of the PSF in the image (`mkpsfmap`), detect point sources (`wavdetect`), disentangle the sources from the background (`roi`), and replace the pixels of the point source regions of the image with values interpolated from the surrounding background regions[11] (`dmfilth`), see Fig. 3.14. In Fig. 3.15, we illustrate the difference of an exposure-corrected image of the X-ray surface brightness distribution of the ICM of the galaxy cluster Abell 2069 (see Sec. 5) before and after the point source subtraction procedure described above.

---

[11] `http://cxc.cfa.harvard.edu/ciao/ahelp/`

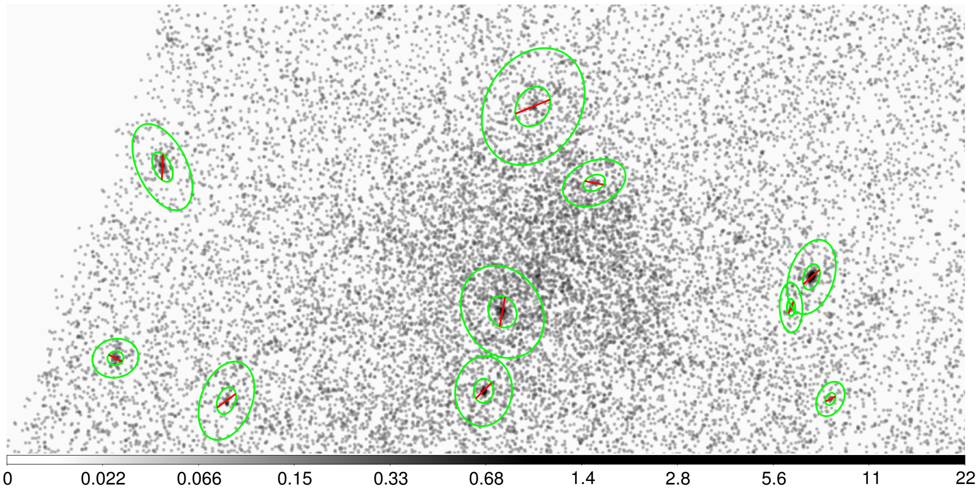

Figure 3.14: Identification of point sources (red lines) and their background contributions (green circles) in the Chandra X-ray image of Abell 2069.

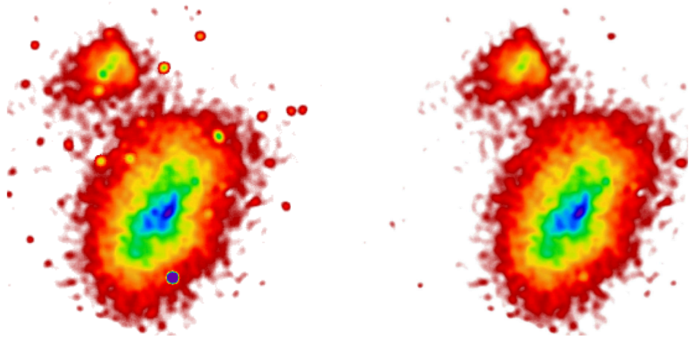

Figure 3.15: Chandra image of the X-ray surface brightness in Abell 2069 in linear scale smoothed with a 2D Gaussian with a FWHM of 20″ before (*left image*) and after (*right image*) point source subtraction.

4 Analysis of the WSRT 346 MHz Legacy Survey

The aim of the WSRT 346 MHz Legacy Survey is the investigation of the morphology and the spectrum of diffuse radio emission in galaxy clusters at low frequencies. At low frequencies we observe a population of cosmic ray electrons at a lower energy than the population we would observe at high frequencies, e.g, at 1.4 GHz (see equation 2.2). The WSRT offered a high sensitivity to extended diffuse radio structures in the past years, thanks to its large fractional bandwidth ($\approx 20\%$) and its sensitivity at large angular scales ($> 15'$), see Sec. 3.2.1. For the Legacy Survey, the radio relics in Abell 115, Abell 1240, and Abell 2061, and the radio halos in Abell 1758, Abell 2218, Abell 2219, Abell 2254, and Abell 2319 have been selected as targets. Moreover, the diffuse radio source candidates in RXC J1053.7+5452 (RXJ1053, see Sec. 4.9) and Abell 2069 have also been observed. Both candidates have tentatively been classified as radio relics. In the case of Abell 2069 the data analysis of the WSRT 346 MHz Legacy Survey data has revealed previously unknown diffuse radio sources. The full analysis of this galaxy cluster is thus presented in Sec. 5. The targets are summarized in Tab. 4.1.

The measurement of the flux density of the diffuse radio emission in our sample is often hindered by the superposition of the diffuse radio emission with compact source emission. To estimate the diffuse part of the flux density better, we imaged the fields with uniform weighting removing the short baselines (`uvrange` $> 0.6\,\mathrm{k}\lambda$). This significantly reduces the sensitivity of the array to diffuse radio emission. The achieved high resolution images are assumed to be dominated by compact source emission and are therefore used to create a sky model which in turn is subtracted from the visibilities. The resulting images from the data with the sky model being subtracted mainly contain the diffuse radio emission, see Fig. 4.1. All uncertainties given below include the potential errors introduced by this procedure following equation 3.10.

We estimate the integrated spectral index of the diffuse radio emission with respect to 1.4 GHz, since most galaxy clusters have been observed and analyzed at this frequency in literature. To confirm their nature as radio halos and radio relics we

Table 4.1: Properties of all clusters of the WSRT 346 MHz Legacy Survey.

Source	RA (J2000) [h m s]	DEC (J2000) [° ′ ″]	z^a	L_{500} (0.1 - 2.4 keV)^e [10^{44} erg s^{-1}]	Scale [kpc / ″]	Type
Abell 115	00 55 59.8	+26 22 41	0.197	7.5	3.261	R
Abell 1240	11 23 32.1	+43 06 32	0.195^b	0.9	3.235	R+R
Abell 1758	13 32 32.1	+50 30 37	0.278^c	8.7	4.222	H
Abell 2061	15 21 17.0	+30 38 24	0.078	1.9	1.476	R
Abell 2069	15 24 09.8	+29 55 16	0.116	4.3	2.101	U
Abell 2218	16 35 52.4	+66 12 52	0.176	5.1	2.981	H
Abell 2219	16 40 21.4	+46 42 21	0.226	17.0	3.626	H
Abell 2254	17 17 40.2	+19 42 51	0.178	–	3.008	H
Abell 2319	19 21 08.8	+43 57 30	0.056^d	1.5	1.087	H
RXC J1053.7+5452	10 53 43.9	+54 52 20	0.070	0.4	1.337	U

Columns. (5): For the definition of L_{500}, see Sec. 2.6, (6): scales have been derived using Ned Wright's cosmology calculator (Wright, 2006), (7): **R** – radio relic, **H** – radio halo, **U** – uncertain
References. $^{(a)}$Ebeling et al. (1998), $^{(b)}$Barrena et al. (2009), $^{(c)}$Boschin et al. (2012), $^{(d)}$Struble and Rood (1999), $^{(e)}$Piffaretti et al. (2011) and Yuan et al. (2015)

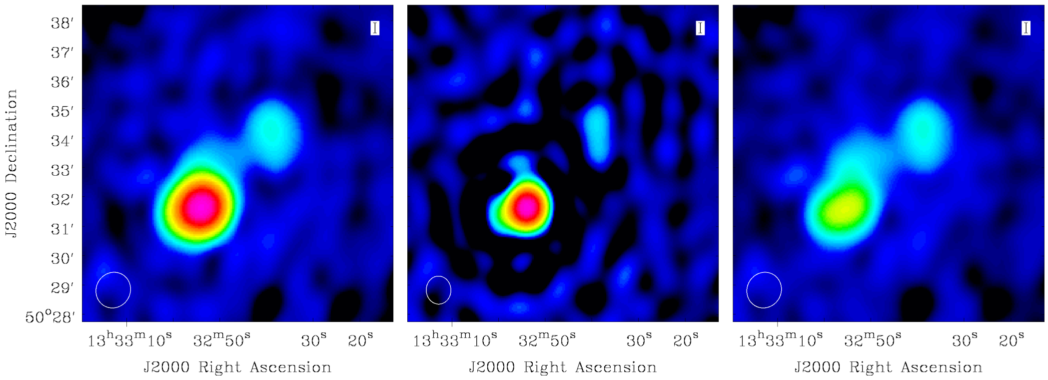

Figure 4.1: Subtraction procedure applied to the WSRT Legacy Survey data. *From left to right:* Total intensity map of a target created with `CLEAN` using Briggs weighting, uniform weighting + `uvrange` $> 0.6\,\mathrm{k}\lambda$, and Briggs weighting after subtraction. The colorscale is arbitrary and identical in all images.

expect a steep spectrum ($\alpha < -1$) known from already confirmed radio halos and radio relics as well as from predictions of the currently favoured models (see Sec. 2.4). Furthermore, we compare their morphology with the maps published at 1.4 GHz. Since we observe a cosmic ray electron population of a lower energy than observed at 1.4 GHz, deviations in the morphology of the diffuse radio emission might provide insights into the galaxy cluster merger dynamics and history.

The observation IDs and total exposure times are listed in Tab. 4.2. For Abell 2254 we used reduced data from the *XMM-Newton* data archive (observation ID 0601080101).

Table 4.2: Chandra ACIS-I archival data.

Source	Observation IDs	Total exposure time [ks]
A115	3233, 13458, 13459, 15578, 15581	361.55
A1240	4961	51.35
A1758	2213, 7710, 13997, 15538, 15540	212.97
A2061	10449	31.35
A2069	4965	55.42
A2218	553, 1454, 1666, 7698	71.02
A2219	896, 7892, 13988, 14355, 14356, 14431, 14451	194.82
A2319	3231, 15187	89.60
RXJ1053	15322	24.76

In the following, we discuss our results of the analysis of the WSRT 346 MHz Legacy Survey on the individual sources listed in Tab. 4.1. The results are summarized in Sec. 4.10.

4.1 Abell 115

Abell 115 is a merging galaxy cluster composed of three major galaxy concentrations as observed in the optical (Beers et al., 1983). The two main components correspond with the two X-ray peaks detected by Forman et al. (1981). They are colliding with a LoS impact velocity of 1 600 km s^{-1} (Barrena et al., 2007). The cool cores of both main components have not been disrupted by the merger yet. On the other hand, the temperature distribution of the ICM is highly nonuniform (Gutierrez and Krawczynski, 2005). The northern component (in the following denoted with A115N) hosts the very strong radio source 3C 28 with a total flux density of 7 Jy in the WSRT 346 MHz map. 3C 28 is known to have an unusually distorted double lobe structure (Feretti et al., 1984; Giovannini et al., 1987), which is not resolved at the resolution of the WSRT at 346 MHz. Such a distortion might be an indication of large-scale flows and inhomogeneities of the ICM in the northern component of Abell 115 (Heinz et al., 2006; Forman et al., 2014). The BCG of the northern concentration is associated with 3C 28. The radio relic in Abell 115 was first reported by Giovannini et al. (1999). Govoni et al. (2001b) confirmed the discovery of the radio relic, extending from the northern sub-cluster center to its periphery, with the VLA at 1.4 GHz in C and D configuration. They measured an integrated flux density of 147.0 mJy at

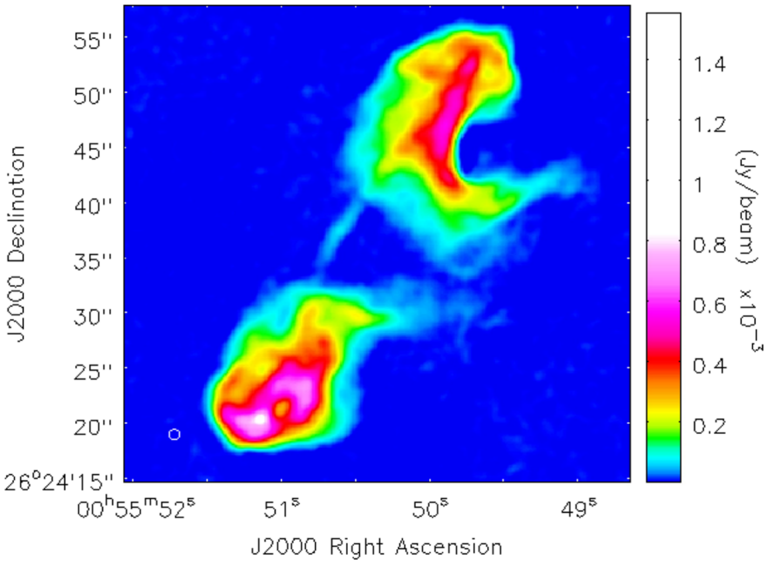

Figure 4.2: Map of 3C 28 observed with the VLA in B and C configuration at a central frequency of 5 GHz. The rms noise level is 4 µJy beam^{-1}. The restoring beam is 1′. Image adapted from Harwood et al. (2015).

1.4 GHz and an LLS of the radio relic of 2.5 Mpc. The radio relic is stretched into a low-density area of the ICM. Since shock acceleration models predict a spherically symmetric compression of the ICM, this source is apparently unusual. Botteon et al. (2016a) detected a shock coinciding with the western part of the radio relic. The Mach numbers derived from the density ($\mathcal{M} = 1.7 \pm 0.1$) and the temperature ($\mathcal{M} = 1.8^{+0.5}_{-0.4}$) jumps in X-ray match. Botteon et al. (2016a) claim that the radio relic is in agreement with an off-axis merger and can be best explained through re-acceleration of pre-existing mildly relativistic cosmic ray electrons. The radio galaxy VLSS J0056.0+2627 might have provided the seed electrons for the eastern part of the radio relic.

We have recovered the radio relic at 346 MHz (see Fig. 4.3). Unfortunately, 3C 28 and the second strongest radio source on top of the relic (VLSS J0056.0+2627, a narrow-angle tail radio galaxy (Gregorini and Bondi, 1989)), with a flux density of ≈ 650 mJy, superpose with the radio relic. Since both sources are very luminous and known to be extended, a subtraction of these sources within acceptable error margins turned out not to be reliable. A detailed high resolution model of 3C 28 at 346 MHz would be necessary. The imaging of 3C 28 or even VLSS J0056.0+2627 at a sufficient high resolution $\theta \ll 1'$ is beyond the capabilities of the WSRT. The impact of these sources on the morphology might be severe. Therefore, we present the radio relic contours from a $\sigma_{\rm rms}$ level larger than 3. We estimated the flux density

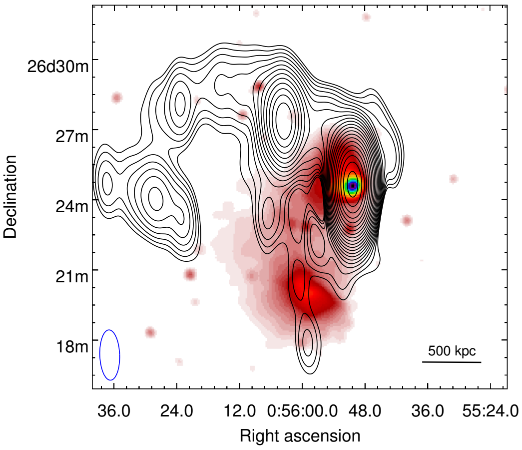

Figure 4.3: Radio and X-ray emission in Abell 115. *Black contours:* WSRT 346 MHz image. The noise level is $\sigma_{\rm rms} \approx 0.5\,\rm mJy\,beam^{-1}$. Contour levels start at 5.9 mJy and are spaced by a factor of $\sqrt{2}$. The shape of the restoring beam is $129'' \times 51''$ with a position angle of $-178°$. *Colorscale:* X-ray surface brightness at 0.5 - 7 keV in linear scale smoothed with a 2D Gaussian of a FWHM of $20''$.

of the radio relic through measuring the small area left of VLSS J0056.0+2627, where the radio emission is likely dominated by the radio relic emission. The measured surface brightness of this area is assumed to be representative of the entire area of the radio relic. We estimate an integrated flux density of the radio relic of ~ 600 mJy at 346 MHz. This corresponds to a spectral index of roughly -1, which is in agreement with the DSA model. We note that the surface brightness of the radio relic at the location of 3C 28 might be significantly higher and that we thus might underestimate the true flux density of the radio relic.

The LLS of the radio relic remained constant at 346 MHz in comparison to 1.4 GHz (east-west elongation). In our maps, the radio relic is slightly more extended to the south compared to the maps of Govoni et al. (2001b) and Botteon et al. (2016b) at 1.4 GHz. This can only be confirmed if the impact of 3C 28 and VLSS J0056.0+2627 on the recovered morphology of the diffuse radio emission is constrained much better.

4.2 Abell 1240

Abell 1240 is composed of two major concentrations of galaxies which are aligned along the same north-south direction as its X-ray surface brightness profile. A BCG is associated with each of the northern and the southern galaxy clump. Barrena et al. (2009) suggest that we see a merger in Abell 1240 in the plane of sky and that both galaxy concentrations have already undergone a first core passage. The presence of a double-relic was first reported by Kempner and Sarazin (2001) after their analysis of the WENSS. This discovery has later been confirmed by Bonafede et al. (2009) by deep VLA observations at 325 MHz and 1.4 GHz. The two radio relics are located at opposite sides of the galaxy cluster and the semi-major axis of both radio relics is perpendicular to the cluster's north-south elongation. The northern relic (in the following denoted with A1240N) and the southern relic (in the following denoted with A1240S) are located at a distance of $\approx 270''$ and $\approx 400''$ from the galaxy cluster's X-ray center, respectively. Bonafede et al. (2009) measured an integrated flux density of 6.0 ± 0.2 mJy for A1240N and 10.1 ± 0.4 mJy for A1240S at 1.4 GHz. Moreover, they derived a mean spectral index in the region where the surface brightness at both frequencies is $> 3\sigma_{\rm rms}$. This resulted in a spectral index of -1.2 ± 0.1 for A1240N and -1.3 ± 0.2 for A1240S. Both relics show a mean degree of polarization of $\approx 25\%$ at 1.4 GHz.

We have recovered both relics at 346 MHz (see Fig. 4.4). Within our $3\,\sigma_{\rm rms}$ contours we measure an integrated flux density of 35.7 ± 2.0 mJy for A1204N and 54.5 ± 3.0 mJy for A1240S. This allows us to confirm the spectral index estimate by Bonafede et al.

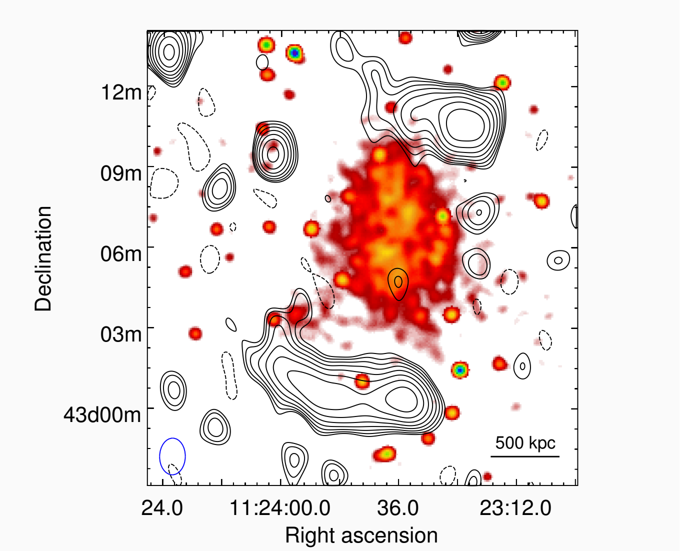

Figure 4.4: Radio and X-ray emission in Abell 1240. *Black contours:* WSRT 346 MHz image. The noise level is $\sigma_{\rm rms} \approx 0.25\,{\rm mJy\,beam^{-1}}$. Contour levels are drawn at $[-0.75, 0.75, 1.1, 1.5\,, 2.1, 3.0, 4.2, 6.0, 8.4]$ mJy. The negative contour is drawn with a dashed line. The shape of the restoring beam is $82'' \times 57''$ with a position angle of $-1°$. *Colorscale:* see Fig. 4.3.

(2009) with −1.3 for A1204N and −1.2 for A1240S.

The morphology of both radio relics is in agreement with the radio maps at 1.4 GHz. So there is no indication of a spatially separated population of aged electrons in Abell 1240. Moreover, both radio relics are located directly at the periphery of the galaxy cluster and their shape is tangential to the isophotes of the X-ray emission. The overall morphology and the similar brightness of both radio relics are consistent with the scenario of two symmetric shocks propagating outwards after the occurrence of an equal mass merger in Abell 1240. The spectral indices correspond to a shock Mach number of $\mathcal{M} \approx 2.8$ and $\mathcal{M} \approx 3.3$ for the northern and for the southern radio relic, respectively (see equations 2.5 and 2.9). Our analysis could not recover any sign for a radio halo at a central galaxy cluster position.

4.3 Abell 1758

The galaxy cluster Abell 1758 consists of two hot X-ray luminous subclusters (in the following denoted with A1758N and A1758S) separated by 2 Mpc in projection (Rizza et al., 1998). Both of them show major merger activities independent from each other. Although both cluster parts likely form a gravitationally bound system (Boschin et al., 2012), there are no signs of an interaction between the two cluster parts (Durret et al., 2011). David and Kempner (2004) showed that the hotter subcluster A1758N is in a late stage of a cluster merger between its two hot subclumps along the northwest-southeast direction. They argue that the high temperature of the ICM indicates that any shocks generated by the merger have already propagated throughout most of the subcluster. Moreover, A1758N hosts a powerful narrow-angle tail radio galaxy (O'Dea and Owen, 1985).

Diffuse radio emission in A1758N was first reported by Kempner and Sarazin (2001). This was confirmed by Giovannini et al. (2006) with the VLA at 1.4 GHz detecting a radio halo permeating the central region of the galaxy cluster with ≈ 0.8 Mpc in size. Furthermore, they classified the two peripheral radio sources to the east and to the west of A1758N as radio relics (Giovannini et al., 2009). They measured a total flux density of the diffuse radio emission of 16.7 ± 0.8 mJy and an LLS of ≈ 1.5 Mpc at 1.4 GHz. Although the shape of the diffuse radio emission is very peculiar, Giacintucci (2011) suggests a classification of all the diffuse radio emission as a radio halo after investigating the galaxy cluster with the GMRT at 325 MHz. She measured an integrated flux density of 146 ±7 mJy and a total size of about 1.5 Mpc at 325 MHz.

We have recovered the diffuse radio emission in A1758N at 346 MHz (see Fig. 4.5). The resolution limit of the WSRT prevents us from discriminating the radio halo from the reported radio relics and the strong compact sources to the east and to the west of the radio halo. We applied our subtraction procedure and were able to recover the morphology and the LLS (≈ 1.8 Mpc) of the radio halo similar to the maps published in Giovannini et al. (2009) and Giacintucci (2011). The resulting integrated flux density of the radio halo is 129 ± 8 mJy at 346 MHz, which is in agreement with the measurement by Giacintucci (2011). This results in a rather steep spectral index of about -1.5, putting the radio halo in Abell 1758 close to the population of ultra-steep spectrum radio halos. The presence of ultra-steep spectrum radio halos is only predicted by the turbulent re-acceleration model (see Sec. 2.4.3). There could be still some flux density of the radio halo missing in the high-resolution radio map. The missing flux density might be potentially caused by an oversubtraction of the compact sources. The radio halo shows two peaks corresponding to both edges of the northern clump. The two peaks follow the merger direction (southeast-northwest) and thus probably correspond to the hotter parts of the merging system.

The slightly larger LLS of the radio halo in our map at 346 MHz is uncertain, since our subtraction procedure does not reliably maintain the overall structure of the diffuse radio emission. With our sensitivity we do not to detect any diffuse radio

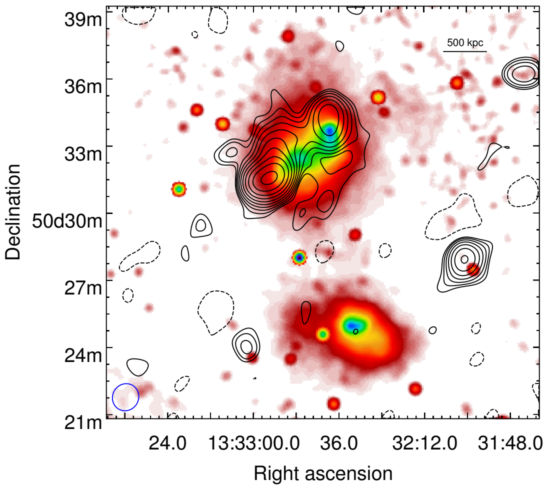

Figure 4.5: Radio and X-ray emission in Abell 1758. *Black contours:* WSRT 346 MHz image with compact sources subtracted. The noise level is $\sigma_{\rm rms} \approx 0.7\,{\rm mJy\,beam^{-1}}$. Contour levels are drawn at $[-2.1, 2.1, 3.0, 4.2, 6.0, 8.4, 11.9, 16.8, 23.8, 33.6, 47.5]$ mJy. The negative contour is drawn with a dashed line. The shape of the restoring beam is $74'' \times 70''$ with a position angle of $-31°$. *Colorscale:* see Fig. 4.3.

emission in the southern component.

4.4 Abell 2061

Abell 2061 is one of ten galaxy clusters of the Corona Borealis supercluster (Postman et al., 1988; Small et al., 1997b,a). It belongs to the northern part of the supercluster (Small et al., 1998), together with the smaller nearby cluster Abell 2067. Since Abell 2061 and Abell 2067 are separated by 2.5 Mpc in the plane of the sky and about 600 km s^{-1} in redshift, both galaxy clusters are probably bound (Rines and Diaferio, 2006). X-ray investigations revealed an elongation of the hot ICM of Abell 2061 along the northwest-southeast direction, with an extension towards Abell 2067 (Marini et al., 2004). It is debated whether both galaxy clusters might be interacting or even in a pre-merger state. Marini et al. (2004) and Hogge et al. (2013) also find evidence of an internal shock in the northern part of Abell 2061. The internal shock could be caused by an infalling galaxy group along the northwest-southeast axis. The presence of a radio relic, first reported by Kempner and Sarazin (2001), along the same axis but on the opposite side of Abell 2067, supports the scenario of a major disturbance in Abell 2061 induced from an ongoing merger. Kempner and Sarazin

(2001) measured a flux density of the radio relic of 104±15 and 19±3 mJy at 327 MHz and 1.4 GHz, respectively; yielding a spectral index of −1.17 ± 0.23. Moreover, Farnsworth et al. (2013) measured a flux density of 25.3 ± 5.6 mJy for the radio relic with the GBT at 1.4 GHz. Analyzing WSRT data, van Weeren et al. (2011) measured a flux density of the radio relic of 27.6 ± 1.0 and 21.2 ± 2.1 at 1382 MHz and 1714 MHz, respectively. Taking into account the measured flux density of the radio relic of 120 mJy from WENSS images at 325 MHz (Rudnick and Lemmerman, 2009), van Weeren et al. (2011) derived a spectral index of −1.03±0.09. Furthermore, Rudnick and Lemmerman (2009) reported the presence of increased flux density in the area of the cluster center. The presence of a radio halo in Abell 2061 has later been confirmed with the GBT at 1.4 GHz (Farnsworth et al., 2013). They measured a flux density of 16.9 ± 4.2 mJy.

We have recovered the radio relic at 346 MHz (see Fig. 4.6) as well as a not yet reported source located at the galaxy cluster center. Two compact sources to the north and to the south are embedded in the radio relic emission. We thus measure an integrated flux density of the radio relic of 90±9 mJy subtracting the contribution from the two compact sources. This is not in agreement with the measurements by Rudnick and Lemmerman (2009) but still within the errors of the flux density measured by

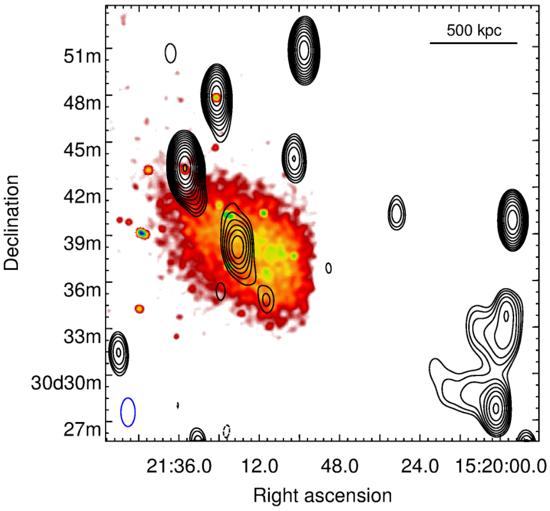

Figure 4.6: Radio and X-ray emission in Abell 2061. *Black contours:* WSRT 346 MHz image. The noise level is $\sigma_{\rm rms} \approx 1.0\,{\rm mJy\,beam^{-1}}$. Contour levels are drawn at $[-3.0, 3.0, 4.2, 6.0, 8.5, 12.0, 17.0, 24.0, 33.9]$ mJy. The negative contour is drawn with a dashed line. The shape of the restoring beam is $110'' \times 55''$ with a position angle of $-180°$. *Colorscale:* see Fig. 4.3.

Kempner and Sarazin (2001). If we compare the 1.4 GHz measurement by Kempner and Sarazin (2001) with van Weeren et al. (2011) this constrains the spectral index of the radio relic to be within ≈ -0.8 and -1.1. Since the radio relic emission is only covered by a few beams, there is only little evidence for an extension of the radio relic emission towards the galaxy cluster center compared with the morphology of the radio relic at 1.4 GHz. The sharp edge to the west, presumably the location of the shock front, and the filamentary structure in the direction of the galaxy cluster center shows the presence of aged electrons downstream of the shock. The detection of any X-ray brightness jump is challenging because of the low X-ray surface brightness at the location of the radio relic. With a distance of ~ 1.7 Mpc to the galaxy cluster center, the radio relic in Abell 2061 is one of the most distant ones.

The newly discovered source at the galaxy cluster center of Abell 2061 shows a flux density of 40.8 ± 3.2 mJy and is not associated with any cluster galaxy. This source is potentially extended, which is supported by the profile of the source with respect to the beam size. We thus speculate that we see the peak of the reported radio halo by Farnsworth et al. (2013).

4.5 Abell 2218

Abell 2218 is a massive galaxy cluster which is one of the first known to exhibit a Sunyaev–Zel'dovich (SZ) effect (Birkinshaw et al., 1978; Perrenod and Lada, 1979; Birkinshaw et al., 1981; Schallwich, 1982; Birkinshaw and Gull, 1984; Jones et al., 1993; Uyaniker et al., 1997; Tsuboi et al., 1998). Pello-Descayre et al. (1988) discovered arc-like structures in the g- and r-band caused by gravitational lensing of background galaxies by the dense dark matter core (Pello et al., 1992). Today Abell 2218 is a much studied lensing galaxy cluster (see, e.g., Abdelsalam et al., 1998; Mohammed et al., 2014). Chandra observations revealed a displacement of the X-ray centroid from the BCG and an azimuthally asymmetric temperature structure in the galaxy cluster core. Machacek et al. (2002) claim that the observed X-ray structure is consistent with Abell 2218 being an off-axis merger system at roughly 1 to 2 Gyr after the initial interaction (Machacek et al., 2002). Govoni et al. (2004) derived a temperature map from Chandra observations that confirms the irregular temperature distribution. They suggest that Abell 2218 is at a later merger state. Schallwich and Wielebinski (1979) detect a complex radio source at the center of Abell 2218 with the Effelsberg 100-m single dish telescope measuring a total flux density of 28 mJy at 2.7 GHz. Most of the compact radio sources in the central part of Abell 2218 show optical counterparts, mainly elliptical galaxies which are cluster members (Le Borgne and Vilchez-Gomez, 1993). Birkinshaw (1986) and Moffet and Birkinshaw (1989) detected a radio halo in Abell 2218 using the Cambridge One-Mile Radio Telescope at 408 MHz and 1.4 GHz as well as the VLA at 1.4 GHz and 4.8 GHz, respectively. Partridge et al. (1987) measured a flux density of the radio halo of 0.6 mJy at 5 GHz. The radio halo was then observed by Giovannini and Feretti (2000) with the VLA in C- and D-configuration at 1.4 GHz. They measured an integrated flux density of 4.7 mJy at 1.4 GHz with an LLS of 490 kpc. The fact that the radio halo in Abell 2218 is smaller than typical cluster-wide radio halos and that there is a slight offset between the peaks of the radio and the X-ray emission supports the idea that Abell 2218 is at a late merger state. A closeby source to the north is obscuring the diffuse radio emission.

We have recovered the diffuse radio emission at 346 MHz (see Fig. 4.7) with a significantly higher LLS of about 0.8 Mpc than in the map at 1.4 GHz shown by Giovannini and Feretti (2000). We do not confirm the offset between the radio halo peak and the X-ray peak. In our maps both positions agree with each other within the uncertainties of our resolution. We note that our recovered morphology is very different from the one presented in Giovannini and Feretti (2000). We measure an integrated flux density of 34.6 ± 8.6 mJy excluding the area of the closeby compact source to the north and thus estimate the spectral index to be about -1.4. The significantly larger extent of the radio halo in our 346 MHz image of Abell 2218 may

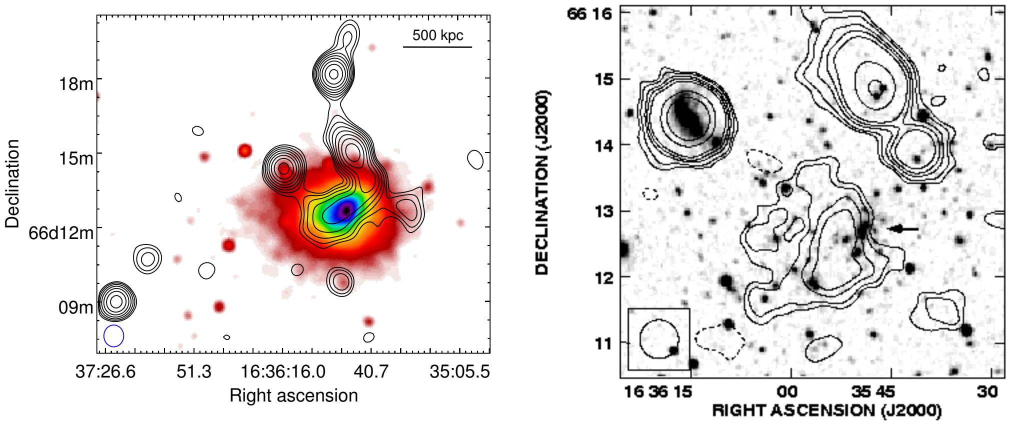

Figure 4.7: Radio and X-ray emission in Abell 2218. **Left image:** *Black contours:* WSRT 346 MHz image. The noise level is $\sigma_{\rm rms} \approx 0.4\,{\rm mJy\,beam}^{-1}$. Contour levels are drawn at $[-1.2, 1.2, 1.7, 2.4, 3.4, 4.8, 6.8, 9.6, 13.6, 19.2]$ mJy. The negative contour is drawn with a dashed line. The shape of the restoring beam is $53'' \times 48''$ with a position angle of $-180°$. *Colorscale:* see Fig. 4.3. **Right image:** Radio contour map at 1.4 GHz overlaid on an optical DSS image, adapted from Giovannini and Feretti (2000).

indicate that the turbulent energy dissipated in the ICM started to slowly decrease in the outskirts of the galaxy cluster, leaving behind a population of aged electrons at larger radial distances from the galaxy cluster core (see, e.g., Feretti et al., 2004a). Such an aged population may not be visible anymore at 1.4 GHz. On the other hand, the sensitivity of the 1.4 GHz observation could have been too low to recover the more extended parts of the radio halo.

4.6 Abell 2219

Abell 2219 is a hot and X-ray luminous galaxy cluster. It is located at a redshift $z = 0.2256$ and shows evidence of an undergoing complex merging episode, where many clumps, possibly in different dynamical states, are involved (Boschin et al., 2004). The bimodal core structure, associated with the two BCGs, as well as the overall X-ray morphology suggest a major merger in an advanced state along the northwest-southeast direction (Rizza et al., 1998). Recent detailed Chandra studies revealed the existence of multiple surface brightness edges, namely two low Mach number shock fronts ($\mathcal{M} \sim 1.2$) to the northwest and to the southeast as well as indications of a sloshing cold front at a distance of 360 kpc from the galaxy cluster center (Million and Allen, 2009; Canning et al., 2015). Bacchi et al. (2003) observed this cluster with the VLA in C- and D-configuration at 1.4 GHz and discovered a radio halo with an integrated flux density of 81 ± 4 mJy and an LLS of 2.2 Mpc. It thus belongs to the brightest and most extended radio halos known so far. The radio halo is superimposed by a strong central radio source, which is a blend of three distinct components that are associated with cluster galaxies (Owen et al., 1992). Orrú et al. (2007) investigated the radio halo with the VLA at 325 MHz und measured a total flux density of 232 ± 17 mJy, after subtracting discrete sources, and an average spectral index of 0.9 ± 0.1.

We have recovered the diffuse radio emission at 346 MHz (see Fig. 4.8) and confirmed the LLS to be about 2.3 Mpc. The central radio source also dominates the radio emission of the galaxy cluster in our WSRT radio maps. We thus can only estimate the flux density of the radio halo to be 135 ± 10 mJy after subtracting the compact sources. So we estimate a spectral index of the radio halo of about -0.4. This corresponds to the spectral index of compact "core-dominated" flat spectrum radio sources ($\alpha \lesssim -0.5$), which are often identified with quasars having their jets closely aligned with the line of sight (see, e.g., Barthel et al., 2000). This scenario is ruled out by the size of the diffuse radio emission and the fact that Bacchi et al. (2003) could clearly separate the diffuse radio emission from the embedded compact sources

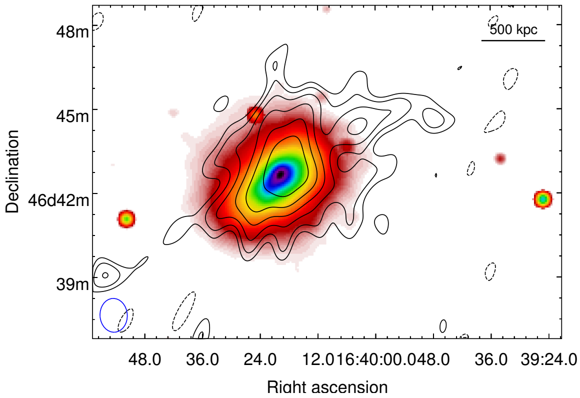

Figure 4.8: Radio and X-ray emission in Abell 2219. *Black contours:* WSRT 346 MHz image after subtracting compact sources. The noise level is $\sigma_{\rm rms} \approx 0.7\,{\rm mJy\,beam}^{-1}$. Contour levels are drawn at $[-2.1, 2.1, 3.0, 4.2, 5.9, 8.4, 11.9, 16.8, 23.8, 33.6]$ mJy. The negative contour is drawn with a dashed line. The shape of the restoring beam is $72'' \times 58''$ with a position angle of 4°. *Colorscale:* see Fig. 4.3.

at 1.4 GHz. We suspect that our radio map imaged at the highest possible resolution of the WSRT still contains a significant flux density contribution of the radio halo. Subsequently, we might have erroneously subtracted part of the diffuse flux density, which is then missing in the low resolution image. There is a slight offset between the peak of the radio and the X-ray emission visible in the image after subtracting the compact sources. Since we might have subtracted too much of the central radio source, this detection of the offset should be taken with caution. In contrast with most of the radio halos investigated in the framework of the WSRT Legacy Survey, the radio halo emission is more extended than the X-ray emission. This indicates that a sufficient amount of turbulent energy is dissipated in the low-density area of the cluster outskirts, probably due to shocks propagating outwards. This scenario is suggested by the detection of several surface brightness jumps in the outskirts of Abell 2219.

4.7 Abell 2254

Abell 2254 is a dynamically disturbed galaxy cluster at a redshift of $z = 0.178$. The galaxy cluster hosts four dominant cluster galaxies, three of which are located at the eastern boundary of the galaxy cluster. From optical and X-ray analysis it has been revealed that Abell 2254 is mainly characterized by a bimodal structure along the east-west direction (Girardi et al., 2011), but may consist of up to five subclusters. In addition, the absence of a temperature drop in the core suggests a merging scenario in which the eastern group has just passed through the main system and disrupted the cool core. The first evidence of an extended diffuse radio emission located in Abell 2254 was reported by Owen et al. (1999). Giovannini et al. (1999) classified this emission as a radio halo with an LLS of about 1 Mpc and a flux density of 32 mJy derived from NVSS images at 1.4 GHz. Govoni et al. (2001b) confirmed the presence of the radio halo with VLA observations at 1.4 GHz. Their images show a very clumpy and irregular structure of the radio halo. They could recover a diffuse flux density of 33.7 mJy and an LLS of 1.2 Mpc at 1.4 GHz. To the northeast, a compact radio source, associated with a cluster galaxy (Girardi et al., 2011), with a flux density of about 38 mJy at 1.4 GHz is embedded in the radio halo emission.

We detected the radio halo in our maps at 346 MHz (see Fig. 4.9) and measured the flux density of the radio halo to be 176 ± 9 mJy within the 3σ contours avoiding the compact radio source to the northeast. This corresponds to a spectral index of about −1.2. In our image the radio halo is extended up to an LLS of 1.3 Mpc. This size is comparable to the size of the radio halo at 1.4 GHz. Following the $3\sigma_{\rm rms}$ contour lines

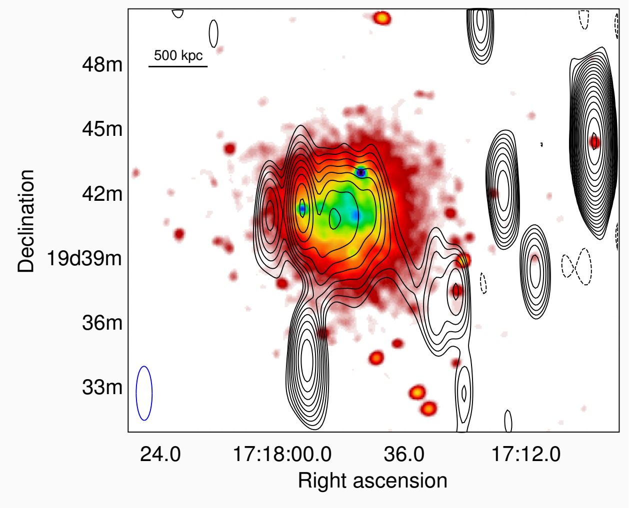

Figure 4.9: Radio and X-ray emission in Abell 2254. *Black contours:* WSRT 346 MHz image. The noise level is $\sigma_{\rm rms} \approx 1.0\,{\rm mJy\,beam^{-1}}$. Contour levels are drawn at $[-3.0, 3.0, 4.2, 6.0, 8.5, 12.0, 17.0, 24.0, 33.9, 48.0, 67.9]$ mJy. The negative contour is drawn with a dashed line. The shape of the restoring beam is $151'' \times 44''$ with a position angle of 0°. *Colorscale:* XMM-Newton reduced archival data (Observation ID 0601080101).

the radio halo in Abell 2254 nicely matches the X-ray surface brightness distribution. This is evidence that the ongoing merger episode has introduced turbulence in nearly the whole volume of the denser ICM. According to the evolutionary model by Donnert et al. (2013), such a radio halo indicates that we witness the most violent merger stage right after the core passage.

4.8 Abell 2319

Abell 2319 is a well-studied galaxy cluster at a redshift of $z = 0.056$. It actually consists of two separate galaxy clusters superimposed along the line of sight, which was first reported by Faber and Dressler (1977). The smaller galaxy cluster Abell 2319B is located $10'$ to the northwest of the more massive central galaxy cluster Abell 2319A (Oegerle et al., 1995). Extensive studies in X-ray revealed several signatures of merger activity, in particular the presence of an inhomogeneous temperature structure (Sugawara et al., 2009), including a cool spot located close to Abell 2319B (Markevitch, 1996; Molendi et al., 1999). Furthermore, a cold front has been detected to the southeast of the cD galaxy (O'Hara et al., 2004) as well as a cool arm extending from the tip of the cold front into the direction of Abell 2319B (Govoni et al., 2004). It is suggested that both galaxy cluster parts are probably gravitationally bound and have recently undergone a major merger seen in projection ($50^\circ \pm 20^\circ$) (Yan et al., 2014). Harris and Miley (1978) have detected an irregular radio halo of $\sim 10'$ size with the WSRT at 610 MHz. After subtracting five discrete sources, they have measured a total flux density of the radio halo of 1.0 ± 0.2 Jy. Feretti et al. (1997b) mapped the irregular structure of the radio halo, tracing the X-ray surface brightness from the northeast to the southwest, with the WSRT at 1.4 GHz. They recovered a total flux density of 153 mJy after point source subtraction and an LLS of about $15'$. Furthermore, they reported about a measurement with the Northern Cross Radio Telescope, yielding a flux density of the radio halo of 1.45 Jy at 408 MHz. Farnsworth et al. (2013) measured an integrated flux density of 328 ± 28 mJy and an LLS of 2 Mpc with the single dish GBT at 1.4 GHz. A recent analysis by Storm et al. (2015) with the VLA at 1.4 GHz and X-ray observations with *XMM-Newton* revealed a multiple component radio emission as well as a spiral pattern of the X-ray emitting gas that is commonly associated with gas sloshing. They decomposed the radio halo emission into a main component and a core component, which is 1 400 kpc and 800 kpc in size, respectively. The main component is much more extended to the southwest and does not show a clear X-ray correlation, whereas the core component coincides with the X-ray core. Storm et al. (2015) therefore speculate that the main component radio halo evolved due to merger-driven turbulence and the core-component halo was created due to gas sloshing. They measured a total integrated flux density of 240 ± 10 mJy at 1.4 GHz.

We have recovered diffuse radio emission at 346 MHz (see Fig. 4.10) with a large angular extent ($\sim$22 arcmin$\hat{=}$1.4 Mpc). The analysis of the data was complicated, because of strong sidelobes (image artifacts) introduced by the nearby radio galaxy Cygnus A (distance $\sim 8°$), one of the brightest radio sources in the sky. Such sidelobes often appear if strong sources in the periphery are not properly deconvolved and calibrated. We could reduce the effect through imaging both fields simultaneously (CASA option `outlierfield`). After subtracting the compact sources embedded in the diffuse radio emission, we measure a total integrated flux density of the radio halo of 1 283 ± 91 mJy. Compared to the 1.4 GHz map published by Feretti et al. (1997b), the radio halo in Abell 2319 appears to be significantly more extended at 346 MHz in all directions, but is similar in its extension if compared with the VLA map by Storm et al. (2015) at 1.4 GHz. Thus, the presumably larger extension detected at lower frequencies might simply be caused by a lower sensitivity of the older observations.

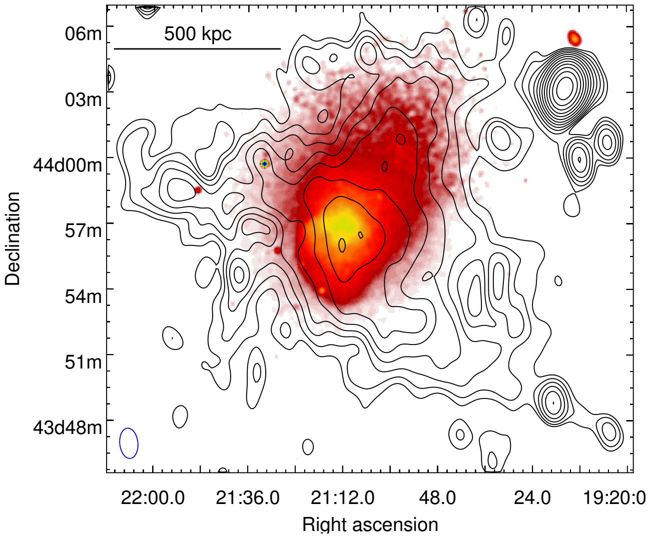

Figure 4.10: Radio and X-ray emission in Abell 2319. *Black contours:* WSRT 346 MHz image after subtracting compact sources. The noise level is $\sigma_{\mathrm{rms}} \approx 0.9\,\mathrm{mJy\,beam^{-1}}$. Contour levels are drawn at $[2.7, 3.8, 5.4, 7.6, 10.8, 15.3, 21.6, 30.5, 43.2]$ mJy. The shape of the restoring beam is $83'' \times 50''$ with a position angle of $-174°$. *Colorscale:* see Fig. 4.3.

Abell 2319 is the only galaxy cluster in the framework of the WSRT Legacy Survey for which measurements of the flux density for more than one more frequency are available. This allows us to compare the measured flux densities in the literature with our measurement, see Fig. 4.11. Additionally, we overplotted the spectral index of $\alpha = -1$ for orientation. The plot shows that there are three significantly different measured values at 1.4 GHz (GBT, WSRT, and VLA) as well as quite high values measured at 408 MHz and 610 MHz. In order to measure the diffuse flux density in the area of Abell 2319, Farnsworth et al. (2013) took all sources visible in the NVSS image at 1.4 GHz down to a flux density threshold of 1.35 mJy and convolved them with the GBT beam ($\theta = 45''$). The achieved convolved image was then subtracted from the observed GBT map, but unidentified compact sources may still contribute to their flux density estimate. On the other hand, the radio halo in Abell 2319 has a largest angular extent of $\approx 22''$, so part of the radio halo might be beyond the sensitivity of the VLA, see equation 3.6. The GBT does not suffer from missing short spacings and is thus able to recover the full extent of the radio halo. Because of the large beam size of the GBT, the true extent of the radio halo might be potentially broadened.

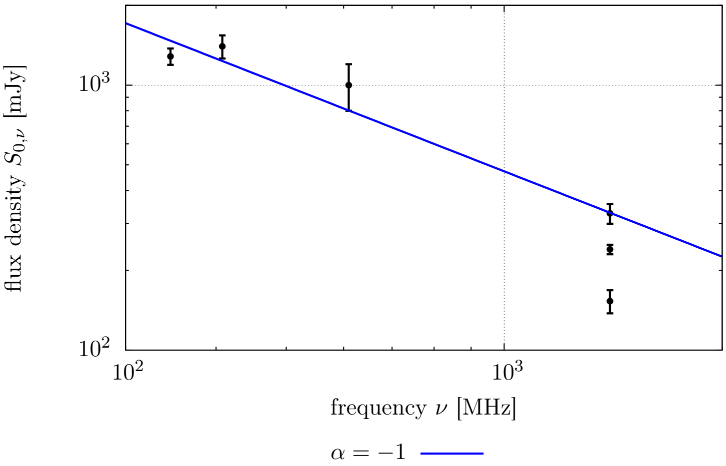

Figure 4.11: Spectral index of Abell 2319. The plot shows measured integrated flux density after subtracting compact sources versus the observation frequency adapted from literature. Errorbars are shown if provided in literature, otherwise the error is assumed to be ± 10%, see text. The straight line represents the spectral index of −1.

Furthermore, the values at 408 MHz and 610 MHz are rather old. The calibration and imaging techniques as well as the flux density reference scale has changed (Scaife and Heald, 2012). That's why we believe that the most recent measurement by Storm et al. (2015) is more suitable as a 1.4 GHz reference for our WSRT map. We thus estimate a spectral index of the radio halo to be about −1.2.

4.9 RXC J1053.7+5452

RXC J1053.7+5452 is a nearby and poorly studied cluster at a redshift of $z = 0.0704$. This cluster is listed in the Cluster Infall Regions in the Sloan Digital Sky Survey (SDSS) (Cluster Infall Regions in the SDSS (CIRS)) catalog (Rines and Diaferio, 2006). Rudnick and Lemmerman (2009) reported the existence of a radio relic at the cluster's periphery with an extent of 1 Mpc. They measured a total diffuse flux density of 360 mJy at 325 MHz. The galaxy cluster was observed by van Weeren et al. (2011) with the WSRT at 1 382 MHz. They recovered an extent of the radio relic of 600 kpc and a total diffuse flux density of 15 ± 2 mJy.

We have recovered the diffuse radio emission at 346 MHz (see Fig. 4.12) with a similar LLS and a flux density of 33.8 ± 2.0 (excluding the compact source to the north). Since there were no further complications in the imaging and the measurement of the flux density, we do not expect to miss a significant amount of flux density. This analysis results in a spectral index of $\alpha \approx -0.6$, thus far too shallow for being a radio relic. Probably, we see extended structure of a radio galaxy with the core being the

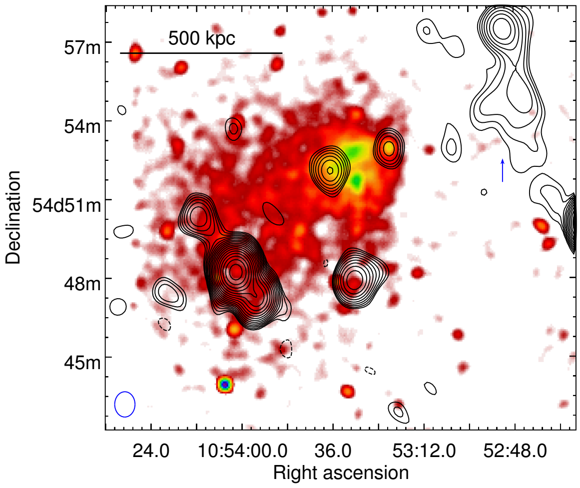

Figure 4.12: Radio and X-ray emission in RXC J1053.7+5452. The blue arrow is indicating the location of the radio relic. *Black contours:* WSRT 346 MHz image. The noise level is $\sigma_{\rm rms} \approx 0.5\,\mathrm{mJy\,beam^{-1}}$. Contour levels are drawn at $[-1.5, 1.5, 2.1, 3.0, 4.2, 6.0, 8.5, 12.0, 17.0, 24.0]$ mJy. The negative contour is drawn with a dashed line. The shape of the restoring beam is $58'' \times 46''$ with a position angle of 0°. *Colorscale:* see Fig. 4.3.

compact source to the north. At the location of the compact source we identify the faint galaxy SDSS J105250+545727.

Therefore, we would classify the radio source in RXC J1053.7+5452 as a radio galaxy, as long as no further evidence, e.g. detection of polarization, is found.

4.10 Concluding remarks on the WSRT Legacy Survey

Tab. 4.3 provides an overview of the results of the WSRT 346 MHz Legacy Survey. The WSRT 346 MHz Legacy Survey was a powerful survey, since we were able to detect diffuse radio emission in all of our targets. On the other hand, the analysis was often affected by compact sources embedded in the diffuse radio emission. Some of these compact sources turned out to be rather hard to isolate, since the resolution of the instrument sets strict limits. Where necessary we applied our subtraction procedure: We imaged the target fields with uniform weighting cutting off the short baselines (`uvrange`$< 0.6\,\mathrm{k}\lambda$), used the images as a model of the compact sources for subtraction and estimated the flux density of the diffuse radio sources in the residual images. For most of the sources, we could reliably measure the flux density of the diffuse radio sources and recovered their morphology at 346 MHz. We

- confirmed the radio relics in Abell 115, Abell 1240, and Abell 2061,
- confirmed the radio halos in Abell 1758, Abell 2218, Abell 2219, Abell 2254, and Abell 2319,
- revealed a much larger extent and a different morphology of the radio halo in Abell 2218 than previously known,
- classified the radio relic candidate in RXC J1053.7+5452 as a radio galaxy, and
- detected the potential peak of the recently reported radio halo in Abell 2061.

An older population of electrons should be visible at such low frequencies, but in our survey the morphology and the extent of the diffuse radio emission at 346 MHz agrees well with the ones at 1.4 GHz. Either we overestimate the occurrence of aged cosmic ray electron populations or our instrument is still not sensitive enough to detect them. On the other hand, the spatial dependence of the spectral index in radio halos as well as in radio relics strongly depends on the underlying mechanisms and the history of the origin of the diffuse radio emission.

Table 4.3: Overview of the results of the WSRT 346 MHz Legacy Survey. Newly discovered sources are in bold face.

Source	type	S_{346} [mJy]	S_{1400} [mJy]	LLS$_{346}$ [Mpc]	LLS$_{1400}$ [Mpc]	α	remarks	references
A115	R	~ 600	147.0	2.2	2.5	~ -1	flux density estimated	1
A1240N	R	35.7 ± 2.0	6.0 ± 0.2	1.2	1.2	-1.3 ± 0.1	–	2
A1240S	R	54.5 ± 3.0	10.1 ± 0.4	1.5	1.5	-1.2 ± 0.1	–	2
A1758N	H	129 ± 8	16.7 ± 0.8	1.8	1.5	-1.5 ± 0.1	subtraction applied	3
A2061	**H**	40.8 ± 3.2	16.9 ± 4.2	0.5	–	-0.6 ± 0.2	peak emission	4
	R	90.0 ± 8.2	27.6 ± 1.0	0.8	0.7	-0.9 ± 0.1	shallow spectral index	5
A2069				analysis presented in Sec. 5				
A2218	H	34.6 ± 2.2	4.7	0.8	0.5	-1.4 ± 0.1	more extended	6
A2219	H	135 ± 10	81 ± 4	2.3	2.2	-0.4 ± 0.1	oversubtracted	7
A2254	H	176 ± 9	33.7	1.3	1.2	-1.2 ± 0.1	–	8
A2319	H	$1\,283 \pm 91$	240 ± 10	1.4	1.4	-1.2 ± 0.1	subtraction applied	9
RXJ1053	**G**	33.8 ± 2.0	15 ± 2	0.5	0.6	-0.6 ± 0.1	shallow spectral index	5

Columns. (2): classification (this work): **R** – radio relic, **H** – radio halo, **G** – radio galaxy, (3): flux density at 346 MHz (this work), (4): flux density at 1.4 GHz, (5): LLS at 346 MHz (this work), (6): LLS at 1.4 GHz, (7): spectral index with statistical errors (this work)

References. 1 – Govoni et al. (2001b), 2 – Bonafede et al. (2009), 3 – Giovannini et al. (2009), 4 – Farnsworth et al. (2013), 5 – van Weeren et al. (2011), 6 – Giovannini and Feretti (2000), 7 – Bacchi et al. (2003), 8 – Govoni et al. (2001b), 9 – Storm et al. (2015)

5 The complex merging galaxy cluster Abell 2069

5.1 Galaxy cluster details

Abell 2069 is a complex galaxy cluster at a redshift of $z = 0.116$ (Struble and Rood, 1999). Together with Abell 2034, Abell 2049, Abell 2062, and Abell 2083, it is part of the so-called 'A2069-supercluster' (Einasto et al., 1997) at a mean redshift of $z = 0.11$ (Small et al., 1997b). The Corona Borealis supercluster (Small et al., 1997b,a) is located in the foreground ($z = 0.07$) of Abell 2069. Abell 2069 is a merging system ($T_\mathrm{X} \sim 6.4\,\mathrm{keV}$) with a moderately high X-ray luminosity $L_\mathrm{X} = 4.6 \cdot 10^{44}\,\mathrm{erg\,s^{-1}}$ (Owers et al., 2009). Recent observations with the Planck satellite provide a cluster mass of $M \approx 5.4 \cdot 10^{44} M_\odot$ (Planck Collaboration et al., 2015). Two BCGs (Gioia et al., 1982) are located at the center with a projected distance of about 55 kpc. X-ray and optical observations revealed two distinct components, in the following denoted A and B, which are separated by $\approx 1\,\mathrm{Mpc}$ from each other (Gioia et al., 1982).

The cluster component B has a peculiar velocity of $485\,\mathrm{km\,s^{-1}}$ with respect to the mean cluster redshift. Owers et al. (2009) detected a cold front towards the northwest of Abell 2069B along with an extension of X-ray emission towards the southeast. Furthermore, the X-ray temperature map by Owers et al. (2009) shows a complex temperature distribution of the X-ray emitting gas and no cool core in the main cluster component Abell 2069A. This suggests a complex dynamical state and thus indicates ongoing merger activities in Abell 2069A.

5.2 Diffuse radio emission at 346 MHz

Giovannini et al. (1999) reported a radio relic candidate of Abell 2069 found in the NVSS at 1.4 GHz, see left image of Fig. 5.1. We observed the galaxy cluster Abell 2069 as a part of the WSRT 346 MHz Legacy Survey. The right image of Fig. 5.1 shows the area of the radio relic candidate as imaged with our data at 346 MHz. Within the $3\sigma_\mathrm{rms}$ contour we measure a flux density of the diffuse radio source to be 51 ±

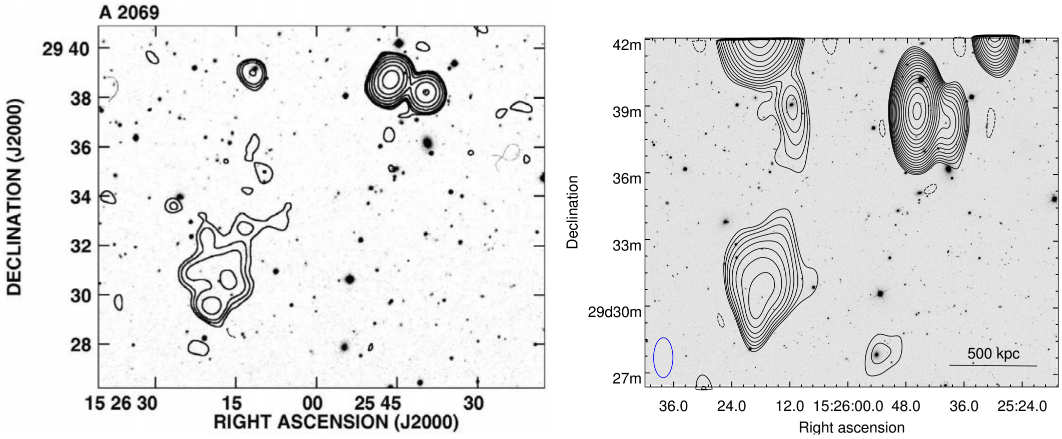

Figure 5.1: The radio relic candidate in Abell 2069. **Left image:** *Black contours:* NVSS image at 1.4 GHz. Contour lines are drawn at $[0.9, 1.35, 2, 4, 8, 16, 32, 64]$ mJy. *Greyscale:* Optical image from the Digitized Palomar Sky Survey (Digitized Palomar Sky Survey (PSS)). Adapted from Giovannini et al. (1999). **Right image:** WSRT 346 MHz radio map imaged with Briggs weighting (`robust` = 0.0 in CASA). The noise level is $\sigma_{\mathrm{rms}} \approx 0.5\,\mathrm{mJy\,beam}^{-1}$. Contour lines are drawn from $3\sigma_{\mathrm{rms}}$ on and are spaced by $\sqrt{2}$. The negative contour line is drawn at $-3\sigma_{\mathrm{rms}}$. The shape of the restoring beam is $108'' \times 52''$ with a position angle of 0°.

5 mJy. Giovannini et al. (1999) noted that the southernmost peak of the diffuse radio source is a compact source visible in the FIRST catalog. The distance of the radio relic candidate to the galaxy cluster center is about ≈ 4.6 Mpc. No radio relic at such a distance is reported in the literature so far. Its rather unusual structure and the presence of another diffuse radio source to the north, which has been revealed during follow-up observations (see Sec. 5.3), suggests that we see a double-lobed radio galaxy. The low resolution radio maps at 346 MHz prevent us from resolving the inner structure of this source. Therefore, the nature of this source remains uncertain so far and will be further discussed in Sec. 5.3.

Searching for radio halos, Farnsworth et al. (2013) studied the galaxy cluster with the GBT at 1.4 GHz and discovered extended emission, see Fig. 5.2, following the same procedure as described for Abell 2319 (see Sec. 4.8). Because of the large beam size of the GBT conclusions about the morphology or the internal structure of the emission are limited. Interestingly, the high sensitivity of the WSRT for diffuse radio emission revealed previously unknown radio features at the center of the galaxy cluster Abell 2069. They are denoted with HA, HB and G and are depicted in the left image of Fig. 5.3. In order to properly recover the diffuse radio emission we needed to

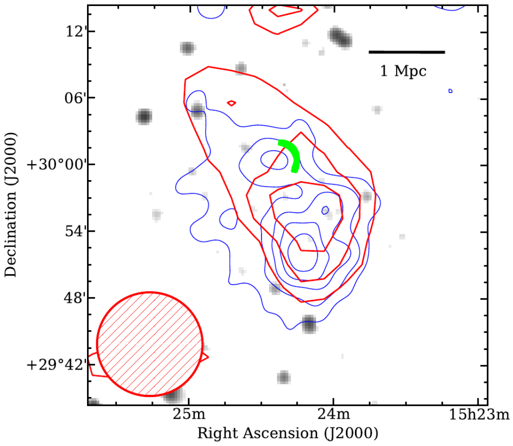

Figure 5.2: Abell 2069. *Red contours:* GBT-NVSS residuals at 1.4 GHz. The noise level is $\sigma_{\mathrm{rms}} \approx 3.0\,\mathrm{mJy\,beam}^{-1}$ with a beam size of $\approx 9.5'$. Contour levels are drawn at $[9.0, 12.0\,, 15.0]$ mJy. *Blue contours:* ROSAT PSPC X-ray image smoothed with a 2D Gaussian of $\sigma = 2'$. *Greyscale:* NVSS image clipped at 1.35 mJy $(45''\mathrm{beam})^{-1}$. The green arc indicates the location of the cold front. Adapted from Farnsworth et al. (2013).

reliably identify and isolate embedded compact sources. We thus performed a follow-up observation of Abell 2069 with the GMRT at a comparable central frequency (see Sec. 3.3.1). With the GMRT we achieved a high resolution image ($14'' \times 7''$) of our target at 322 MHz, see right image of Fig. 5.3. This allowed us to carefully estimate and remove the contribution of the compact sources from the extended emission.

In both images several sources within the cluster area and its vicinity are evident. The high-resolution GMRT image reveals that most of the sources visible in the WSRT image are compact. In particular, the sources B, C, E, F and I show similar flux densities in both images. In Tab. 5.1 we summarize the flux densities of all sources measured in the GMRT image at 322 MHz.

G is the brightest source in the WSRT image close to the cluster center. Neither in the FIRST (Becker et al., 2012) survey, the NVSS (Condon et al., 1998) at 1.4 GHz, nor in the VLSS (Cohen et al., 2007) at 74 MHz has a source been reported at this location. The highly resolved GMRT image shows that G is composed of three distinct sources, in the following indicated as G1, G2 and G3. In the WSRT map the extended source G2 dominates. In the NVSS the area of source G2 is covered by about 5 beams. Since the source is not detected at a $3\sigma_{\mathrm{rms}}$ level, its integrated flux density has to be less than 6.75 mJy. Therefore, G2 is a steep spectrum source with a spectral index of $\alpha_{322}^{1400} < -1.4$. The peculiar morphology of G2 may possibly originate from projected superimposed lobes of a radio galaxy. Radio galaxies with more complex structures are

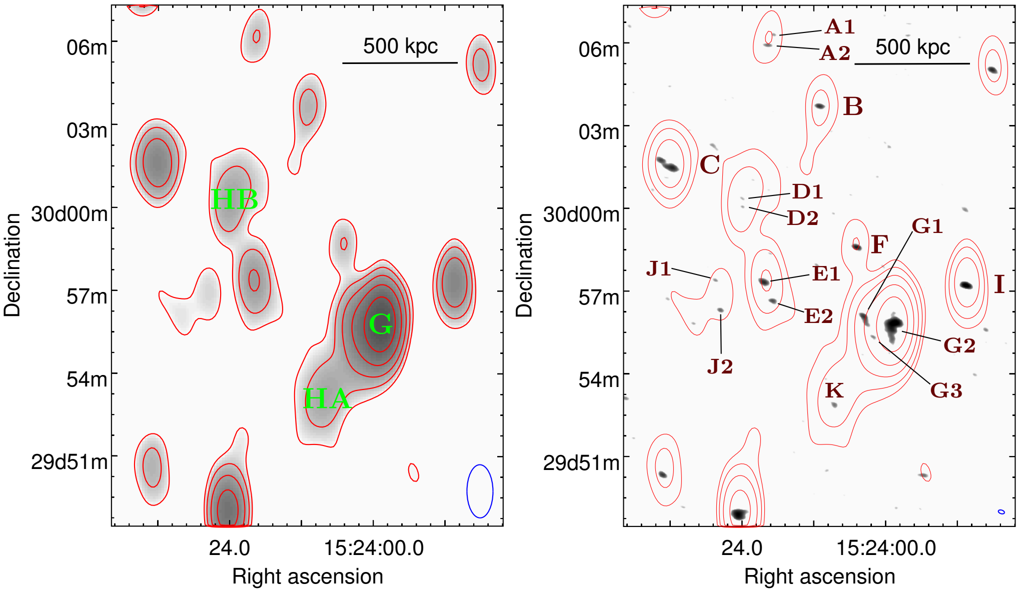

Figure 5.3: Left image: See right image of Fig. 5.1. Contour levels are drawn at [1.5, 3.0, 9.0, 18, 36] mJy. There is no negative flux density below −1.5 mJy within the depicted area. **Right image:** *Red contours:* See the left image. *Grayscale:* GMRT 322 MHz radio map imaged with Briggs weighting (`robust` = 0.0 in CASA). The map is logarithmically scaled. Flux density cutoff is set to $3 \times \sigma_{\rm rms}$ with $\sigma_{\rm rms} \approx 0.2\,{\rm mJy\,beam^{-1}}$. The shape of the restoring beam (denoted with the blue ellipse) is $14'' \times 7''$ with a position angle of 73°.

typically found close to galaxy clusters (Sarazin, 2009). The gravitational potential well of the galaxy cluster is attracting and accelerating all galaxies to higher velocities than the ambient ICM. Possibly, while the radio galaxy is moving through the ICM both lobes could have been bent and decelerated to the north due to ram pressure (Miley et al., 1972). This would classify the source G2 as a "head-tail" radio galaxy (see e.g., Owen et al., 1979). At the southern end of the emission's tail we identified the faint galaxy SDSS J152358+29551 in the SDSS r-band (Ahn et al., 2012), see the brown cross in Fig. 5.4. For this galaxy a photometric redshift of $z_{\rm photo} = 0.100 \pm 0.042$ was determined. Therefore, it could be a member of the galaxy cluster and is a candidate host for the 'head-tail' radio galaxy. Nevertheless, the age of the plasma in the lobes of radio galaxies can be about ∼100 Myr (see, e.g., Orrù et al., 2010; Shulevski et al., 2015), hence the host galaxy might have already moved away significantly. The sources G1 and G3 are associated with the potential cluster galaxies SDSS J152404+295608 ($z_{\rm spec} = 0.112 \pm 0.001$) and SDSS J152402+295522 ($z_{\rm photo} =$

Table 5.1: Flux densities of compact sources in Abell 2069 as measured with the GMRT at 322 MHz.

ID	flux density [mJy]
A1*	1.6 ± 0.3
A2	1.0 ± 0.3
B	3.8 ± 0.6
C†	13 ± 2
D1	0.7 ± 0.1
D2	0.6 ± 0.1
E1*	5.8 ± 0.8
E2	2.5 ± 0.4
F*	5.2 ± 0.7
G1*	4.6 ± 0.8
G2*	52 ± 6
G3*	1.0 ± 0.3
I†	14 ± 2
J1	0.8 ± 0.1
J2	1.6 ± 0.4
K*	1.7 ± 0.4

Notes. All sources marked with † are cataloged in NVSS and all sources that are marginally visible in the NVSS postage stamp images are marked with *.

0.111 ± 0.032), respectively. G1 also shows signs of a “head-tail” structure.

The peak positions of the compact sources E1 and E2 coincide with the foreground optical galaxies MCG+05-36-028 and WISEPC J152419+2956 (both $z = 0.076$), respectively. They may belong to a cluster member of the Corona Borealis Supercluster (Gioia et al., 1982).

Interestingly, the sources HA and HB, clearly visible in the WSRT image, can not be linked to any of the compact sources visible in the GMRT image at their respective locations. The sources D1, D2, located in the subcluster Abell 2069B, are only marginally visible and can not be counted as a clear detection. The source K, associated with the southern BCG of the main cluster component Abell 2069A, is clearly detected, but too faint ($\lessapprox 1$ mJy) to contribute significantly to the extended emission seen in the WSRT image. This strongly suggests that HA and HB are extended diffuse radio features.

In order to recover better only the diffuse part of the emission visible in the WSRT image we had to image with natural weighting after subtracting compact sources. We

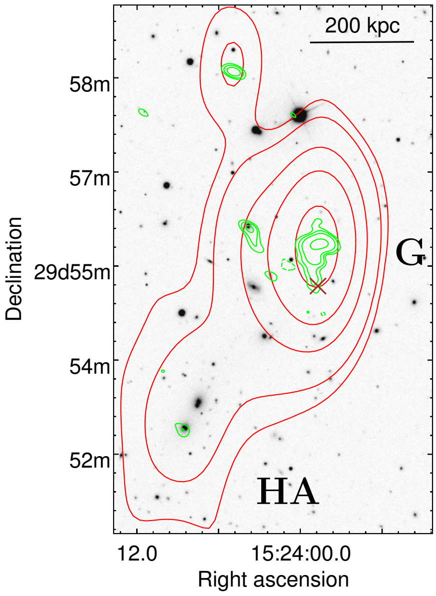

Figure 5.4: Zoom into the G/HA complex. *Red contours:* See the red contours in Fig. 5.3. *Green contours:* 322 MHz GMRT observation. The noise level is $\sigma_{\rm rms} \approx 0.2\,{\rm mJy\,beam}^{-1}$. Contour levels are drawn at $[-0.75, 0.75, 1.1, 1.5\,, 2.1]$ mJy. *Background:* SDSS-III (Data release 10) r-band image. *Brown cross:* Position of the potential host galaxy producing the radio emission G2.

therefore used the GMRT image as a skymodel to remove all visible compact sources in the area of Abell 2069. Since the central frequencies of both observations differ by 24 MHz, we modelled the sources assuming an overall spectral index of $\alpha = -0.8$. Afterwards we subtracted our rescaled GMRT skymodel from the calibrated WSRT visibilities. We then deconvolved the data again but now using natural weighting to put more emphasis on shorter baselines, so extended emission is expected to be recovered better.

The resulting radio map, see the left image of Fig. 5.5, shows extended emission in the main component Abell 2069A as well as a distinct feature in the subcomponent Abell 2069B. The extended radio emission of the main component A shows an LLS of about 900 kpc and is roughly elongated along the semi-major axis of the corresponding elliptical X-ray structure. In our maps the radio features associated with component A and B look apparently connected. We interpret this “bridge” as an imaging effect due to the large beam size of our WSRT map. Furthermore, the peak flux density of the radio emission in A is significantly shifted to the northwest. Since source G is a steep spectrum source (< -1.4), the shift might be caused by residual emission

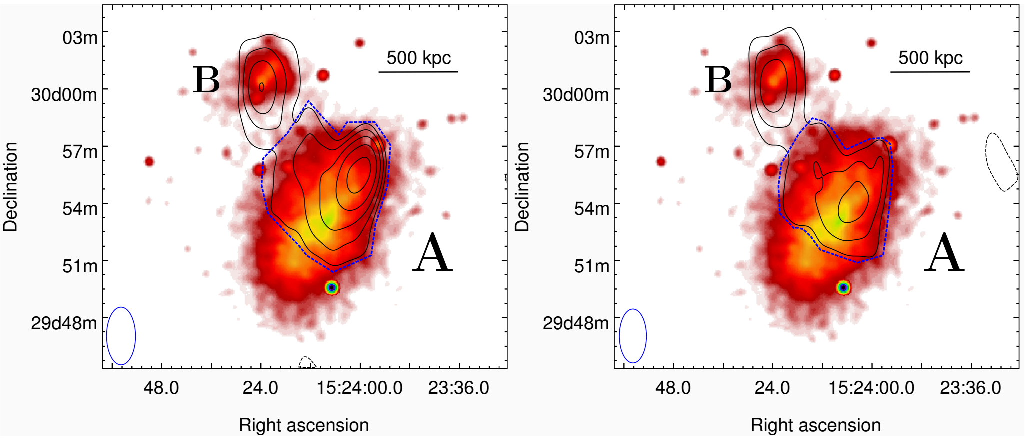

Figure 5.5: Left image: *Black contours:* WSRT 346 MHz image after subtracting compact sources. The noise level is $\sigma_{\rm rms} \approx 1.0\,{\rm mJy\,beam^{-1}}$. Contour levels are drawn at $[-3.0, 3.0, 4.2\,, 6.0, 8.5, 12.0]$ mJy. The negative contour is drawn with a dashed line. *Blue dashed line:* Region where the radio flux density related to the main cluster component A was measured. The skymodel for subtraction is based on the measured flux densities in the GMRT image at 322 MHz, listed in Tab. 5.1. The shape of the restoring beam is $182'' \times 91''$ with a position angle of 0°. *Colorscale:* X-ray surface brightness in linear scale smoothed with a 2D Gaussian of a FWHM of $20''$. The cluster components are labeled with A and B. **Right image:** Image obtained using a more aggressive subtraction procedure. The shape of the restoring beam is $170'' \times 85''$ with a position angle of 0°.

of source G. Imaging the WSRT data again now with uniform weighting provides a higher resolution image which still shows remaining emission at the position of G. The total missing flux density amounts to 14 ± 2 mJy. This indicates that the source G in the GMRT observation does not show all the flux density as observed with the WSRT. We therefore increased the flux density of G in our skymodel by 14 mJy and repeated subtraction and imaging of the WSRT data, see right image of Fig. 5.5. We now find a remaining LLS of about 750 kpc and a radio to X-ray offset of 120 kpc. This corresponds to a fractional radio to X-ray offset of 0.16.

The elongated X-ray morphology of the component A, the presence of two BCGs, and the complex temperature distribution of the X-ray emitting gas are signs of a recent merger in Abell 2069. Since the morphology of the radio and the X-ray emission in the main cluster component Abell 2069A agree with each other, we classify the diffuse radio emission HA as radio halo. Radio halos of similar size have recently been discovered in the galaxy cluster Abell 1689 (Vacca et al., 2011) and CL 0217+70

(Brown et al., 2011a), whereas the latter halo also shows a slight offset with the corresponding X-ray peak.

Unfortunately, the map of our 346 MHz observation is not sufficiently deep to properly constrain the morphology of the source HB, since its size is comparable to the beam width. But comparing the profile of HB to the restoring beam profile, we find a slight extension of the source. This indicates, in agreement with the GMRT observation, that HB is extended.

We estimate the total diffuse flux density of the Abell 2069 cluster complex to be 54 ± 9 mJy through measuring within the black contours, see Fig. 5.5. Within the region enclosed by the blue dashed line (see left image of Fig. 5.5) we measure a flux density of 39 ± 8 mJy for the radio halo HA. In the map obtained with the more aggressive subtraction of G (see right image of Fig. 5.5) we measure a flux density of 25 ± 9 mJy for HA. Those two measurements may only serve as an upper and lower limit of the real flux density distribution of HA. In the first procedure, part of the flux density of G possibly remains in the subtracted image, and with more aggressive subtraction we may also remove part of the diffuse radio emission of the radio halo. In both maps, we measure a flux density of 15 ± 2 mJy for the unclassified source HB.

Our findings confirm the discovery of diffuse radio emission in Abell 2069 by Farnsworth et al. (2013). They recovered 28.8 ± 7.2 mJy of diffuse flux density at 1.4 GHz. Due to the confusion limit the recovered flux density by Farnsworth et al. (2013) may be contaminated by 8-13 mJy because of faint radio sources below the NVSS threshold. This is a viable assumption, since our GMRT image at 322 MHz already corroborates the presence of several sources that are not or only marginally visible in the NVSS (see Tab. 5.1). However, the total flux density of these sources sum up to 11 mJy. This is small in comparison to 66 mJy of all in the NVSS marginally visible sources. Comparing our upper (54 ± 9 mJy) and lower (40 ± 11 mJy) limit of the total diffuse flux density (HA + HB) at 346 MHz with the estimated upper (≈ 20 mJy) and lower (≈ 15 mJy) limit at 1.4 GHz by Farnsworth et al. (2013) (derived by taking 8-13 mJy of potential contamination of the flux density measurement into account), we estimate a spectral index between -0.5 and -1.0. The spectral indices of known radio halos are between -0.9 and -1.9 (Feretti et al., 2012). Because of the low surface brightness of the diffuse radio emission, the flux densities in Abell 2069 are only measured with large uncertainties. Furthermore, we might miss the flux density of even more extended structures. The area of the lowest contour of the GBT map of Abell 2069 at 1.4 GHz by Farnsworth et al. (2013) (depicted in Fig. 9 of their paper) is covered by ~ 40 beams in our radio maps with natural weighting (see Fig. 5.5). Our rms noise of about 1.0 mJy beam^{-1} thus limits the detection threshold of an extended source spread over an area of 40 beams to a flux density of about 19 mJy. Nevertheless, most of the emission originates from the two cluster components A and B. This is in agreement with the GBT map by Farnsworth et al. (2013). Assuming a spectral index of $\alpha_{346}^{1400} = -1$, we estimate a radio power of $P_{1.4\,\mathrm{GHz}} = 2\ldots3 \cdot 10^{23}\,\mathrm{W\,Hz^{-1}}$, according to equation 2.13. This is about 3 to 5 times lower than expected from the radio-power - X-ray-luminosity relation (Cassano et al., 2010, 2013).

After the analysis of the observation of Abell 2069 in the framework of the WSRT 346 MHz Legacy Survey we

- suggest that the radio relic candidate proposed by Giovannini et al. (1999) may be part of a double-lobed radio galaxy,
- revealed that the diffuse radio emission reported by Farnsworth et al. (2013) is mainly composed of two distinct extended emissions located at both cluster components A and B of Abell 2069 (Drabent et al., 2015),
- classified the diffuse radio source in the main cluster component Abell 2069A as a radio halo, and
- found evidence that the radio source discovered in the subcluster component Abell 2069B is extended.

To overcome the resolution limitations of the WSRT we have performed a high resolution follow-up observation with the GMRT at 322 MHz. So we managed to carefully model and subtract many compact sources from the data to extract the diffuse radio emission, in particular the radio galaxy G2. The presence of the diffuse radio source in Abell 2069B is unusual, since only a few radio halos have been found so far in such poor environments (Feretti et al., 2012). According to its size ($\lessapprox 500\,\mathrm{kpc}$) it would fit in the regime of radio mini-halos (see Sec. 2.3.3). The presence of a cold front at the western boundary of the subcluster component Abell 2069B (Owers et al., 2009) suggests that we might see a radio mini-halo (Mazzotta and Giacintucci, 2008). Cold fronts indicate the presence of gas sloshing in cool core galaxy clusters (Gitti et al., 2002, 2004). The gas sloshing might then generate turbulence (ZuHone et al., 2011). Turbulence is in turn able to re-accelerate cosmic ray electrons to highly relativistic energies and then produce diffuse synchrotron emission (see Sec. 2.4.3). Unfortunately, the resolution of the Chandra temperature map by Owers et al. (2009) is not sufficient to detect a cool core in Abell 2069B. On the other hand, the diffuse radio emission in B might be caused by highly relativistic electrons generated by hadronic collisions (Zandanel et al., 2014), see Sec. 2.4.2. Finally, HB could be simply caused by fossil plasma ejected during a former active phase of an AGN located in Abell 2069B.

A proper classification of the source is crucial for the understanding of the dynamics of the galaxy cluster complex Abell 2069. To further constrain the morphology and the spectrum of HB, we performed an observation of the Abell 2069 field with the LOFAR HBA at a central frequency of 153 MHz. The results are presented in the following section.

5.3 Low frequency analysis with the LOFAR HBA

With the LOFAR HBA follow-up observation of Abell 2069 we study the morphology and the spectrum of the diffuse radio emission in both galaxy cluster components at very low frequencies ($\nu = 153\,\mathrm{MHz}$). We aim to confirm the radio halo in Abell 2069A and to clarify the nature of the source in Abell 2069B. Thanks to baselines ranging from $\sim 100\,\mathrm{m}$ up to $\sim 100\,\mathrm{km}$ in our LOFAR observation, we are able to achieve images at high ($\sim 5''$) and low resolution ($\sim 100''$). That's why we do not rely on additional models or observations from other telescopes for a proper discrimination of compact sources from diffuse radio emission. Furthermore, thanks to the wide FoV, a single LOFAR pointing allows us to detect and investigate a large number of nearby radio sources with high fidelity. The radio galaxy 4C +28.39 (Parma et al., 1987) ($z = 0.0825$) of type FRI (see Fanaroff and Riley, 1974, for a morphological classification of radio galaxies) $\sim 2°$ south of our target illustrates the capabilities of the instrument, see Fig. 5.6. At low frequencies this radio galaxy is significantly more extended. Especially at the southern lobe, an extended area of old electrons appears. The stripped pattern close to the radio galaxy core is caused by remaining image artifacts.

Besides our target Abell 2069 (see Sec. 5.3.2 and 5.3.4), we present the radio images of the galaxy clusters Abell 2061 (see Sec. 4.4), Abell 2065, and Abell 2067 from the Corona Borealis Supercluster (Sec. 5.3.1) as well as classify the former radio relic candidate.

5.3.1 The Corona Borealis Supercluster field

In Fig. 5.7 we present the total intensity 5° widefield image of the target field resulting from the direction-independent LOFAR HBA data reduction. The Fig. 5.8 illustrates the location of the galaxy clusters Abell 2061, Abell 2065, and Abell 2067 with respect to Abell 2069. The sensitivity of our LOFAR HBA observation is high enough to recover the diffuse radio emission of Abell 2061 (see Fig. 5.9) and Abell 2065 ($z = 0.0726$) at a resolution scale of $\sim 25''$. The galaxy cluster Abell 2061 was observed in

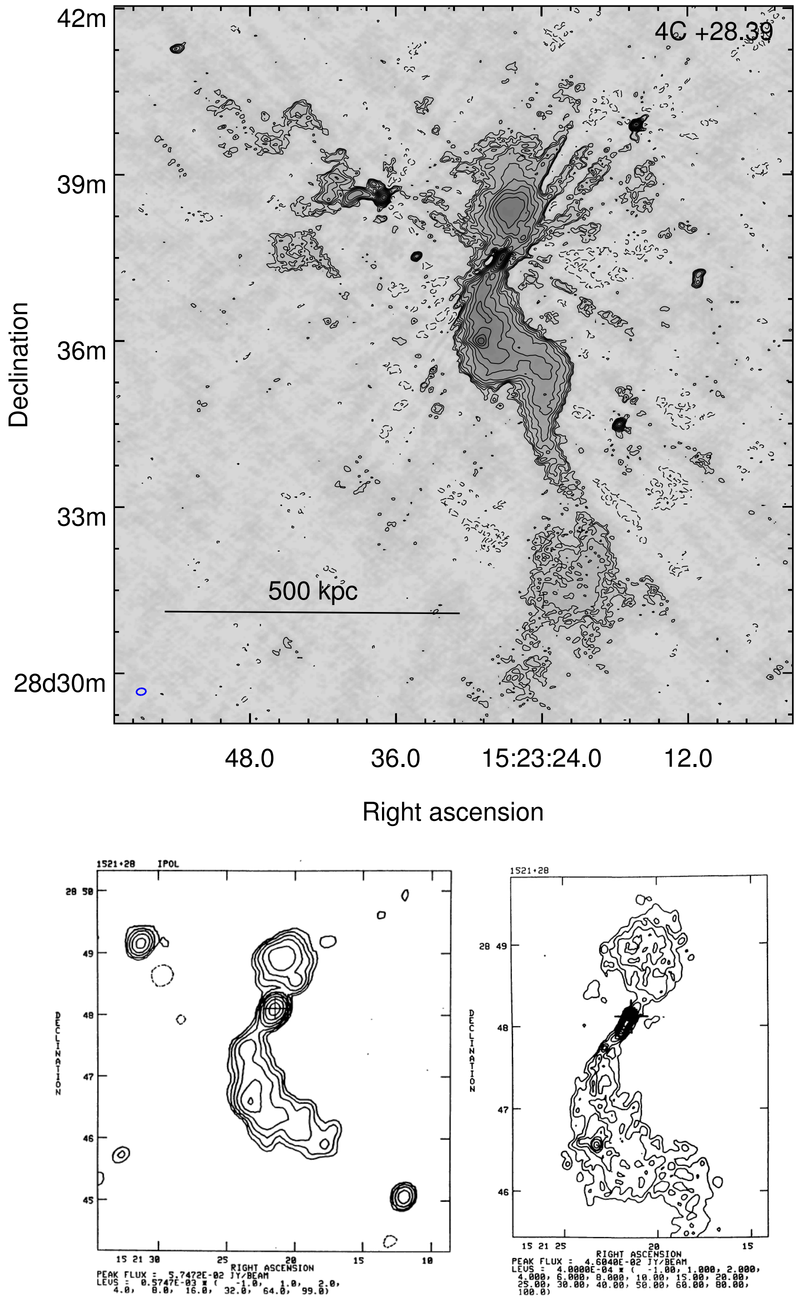

Figure 5.6: *Upper panel:* LOFAR HBA map of the radio galaxy 4C +28.39 using the full bandwidth from 117 MHz to 189 MHz. The noise level is $\sigma_{\rm rms} \approx 0.2$ mJy. Contours are spaced by $\sqrt{2}$ beginning from $3\sigma_{\rm rms}$. The dashed contour line is drawn at $-3\sigma_{\rm rms}$. The shape of the restoring beam is $7'' \times 5''$ with a position angle of 98°. *Lower panel:* VLA maps of the radio galaxy 4C 28+39 at 1.4 GHz adapted from de Ruiter et al. (1986) and Fanti et al. (1987) (*from left to right*).

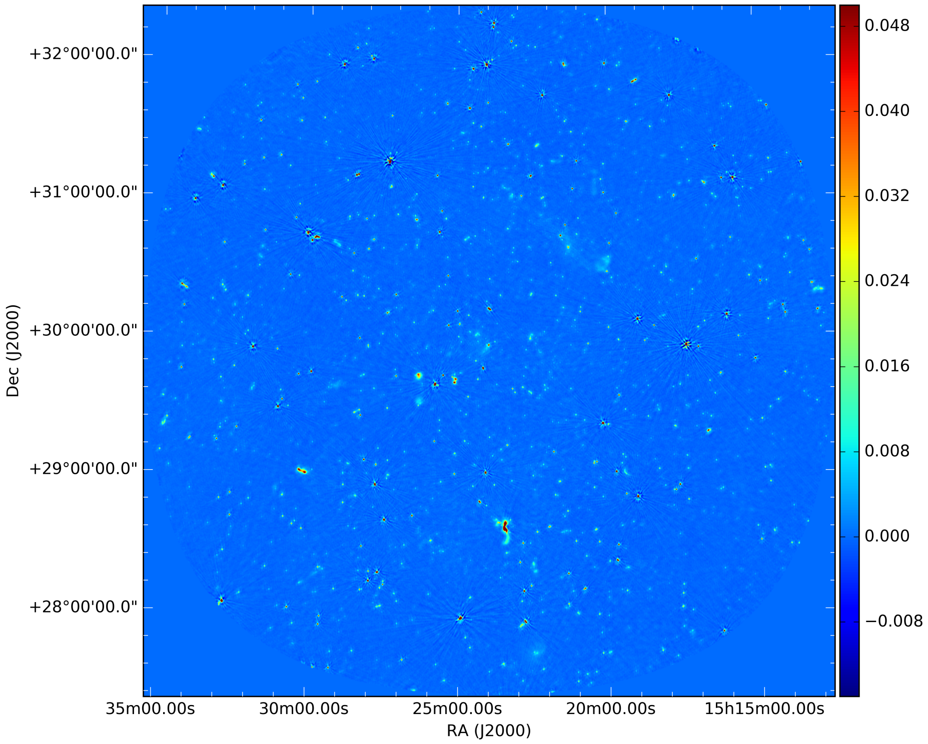

Figure 5.7: Total intensity 5° widefield image of the Corona Borealis Supercluster field including Abell 2069 with LOFAR HBA using the full bandwidth from 117 MHz to 189 MHz. The noise level is $\sigma_{\rm rms} \approx 450\,\mu$Jy. The shape of the restoring beam is $28'' \times 24''$ with a position angle of 46°. The colorscale unit is Jy. The image is not corrected for the primary beam.

the framework of the WSRT 346 MHz Legacy Survey (see Sec. 4.4). In our LOFAR HBA image the radio relic is clearly visible and significantly more extended than at 346 MHz. We measured a flux density of 308 ± 34 mJy for the radio relic in Abell 2061 after subtracting the contribution of compact sources. This corresponds to a steep spectral index of -1.5 ± 0.2 between our LOFAR HBA measurement at 153 MHz and the WSRT measurement at 346 MHz. On the other hand, we derive a much flatter spectral index of -1.1 ± 0.2 between 153 MHz and 1.4 GHz using recent measurements by van Weeren et al. (2011). Such a steepening of the spectrum at low frequencies disagrees with the DSA model. Since Abell 2061 is located at a distance of 1° from the phase reference center, the primary beam pattern is significantly attenuating the brightness level ($\approx 30\%$). The applied primary beam correction might have introduced additional errors we have not yet accounted for. So we derived the average ratio between the flux densities of all sources in the 7C catalog (Hales et al., 2007) and

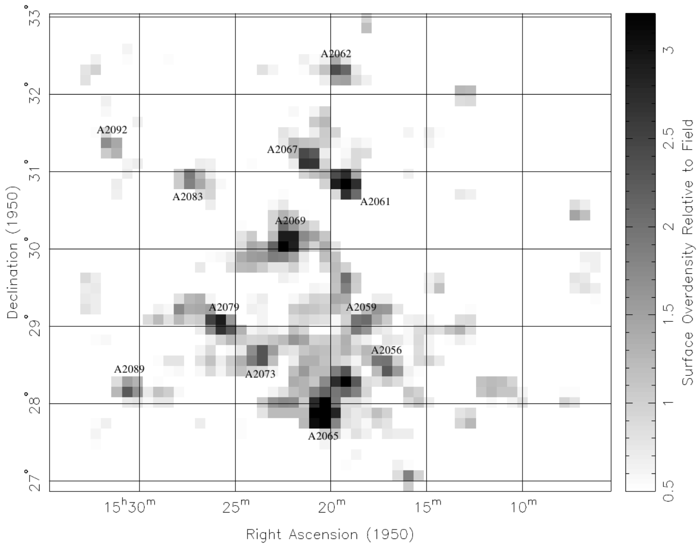

Figure 5.8: Greyscale plot of the galaxy surface overdensity in the field of the Corona Borealis Supercluster for all galaxies brighter than 19th magnitude in r-band. Image adapted from Small et al. (1998).

the flux densities of sources located at a comparable distance to the phase reference center in our LOFAR HBA map. We estimated an average uncertainty of ∼10% between our primary beam corrected map and the 7C flux densities. Since the radio relic is much more extended at 153 MHz, we might simply miss the flux density of this area at 346 MHz (see black and blue contours in the left image of Fig. 5.9) because of sensitivity limits of the WSRT. Furthermore, the LOFAR HBA map reveals low surface brightness emission of an LLS of about 0.9 Mpc in the galaxy cluster Abell 2061, beyond the peak emission already discovered with the WSRT at 346 MHz. We thus confirm the detection of a radio halo in Abell 2061 by Farnsworth et al. (2013) and measure a flux density of 320 ± 33 mJy at 153 MHz. The spectral index of the radio halo between 153 MHz and 1.4 GHz is estimated to be -1.3 ± 0.2, which is typical of already known radio halos (Feretti et al., 2012). Interestingly, the peak of the radio halo shows a very steep spectrum (-1.9 ± 0.2) when comparing its flux density between the LOFAR HBA map at 153 MHz (164 ± 17 mJy) and the WSRT map at 346 MHz (40.8 ± 3.2 mJy). Farnsworth et al. (2013) speculated about a radio relic in Abell 2067 and the existence of a filamentary bridge between both galaxy clusters. Our LOFAR image does not provide any evidence for a radio bridge between Abell 2061 and Abell 2067 (see right image of Fig. 5.9), but there is an increased noise level between the radio relic and the radio halo of Abell 2061.

Close to the FWHM of the LOFAR primary beam we detected the radio halo in

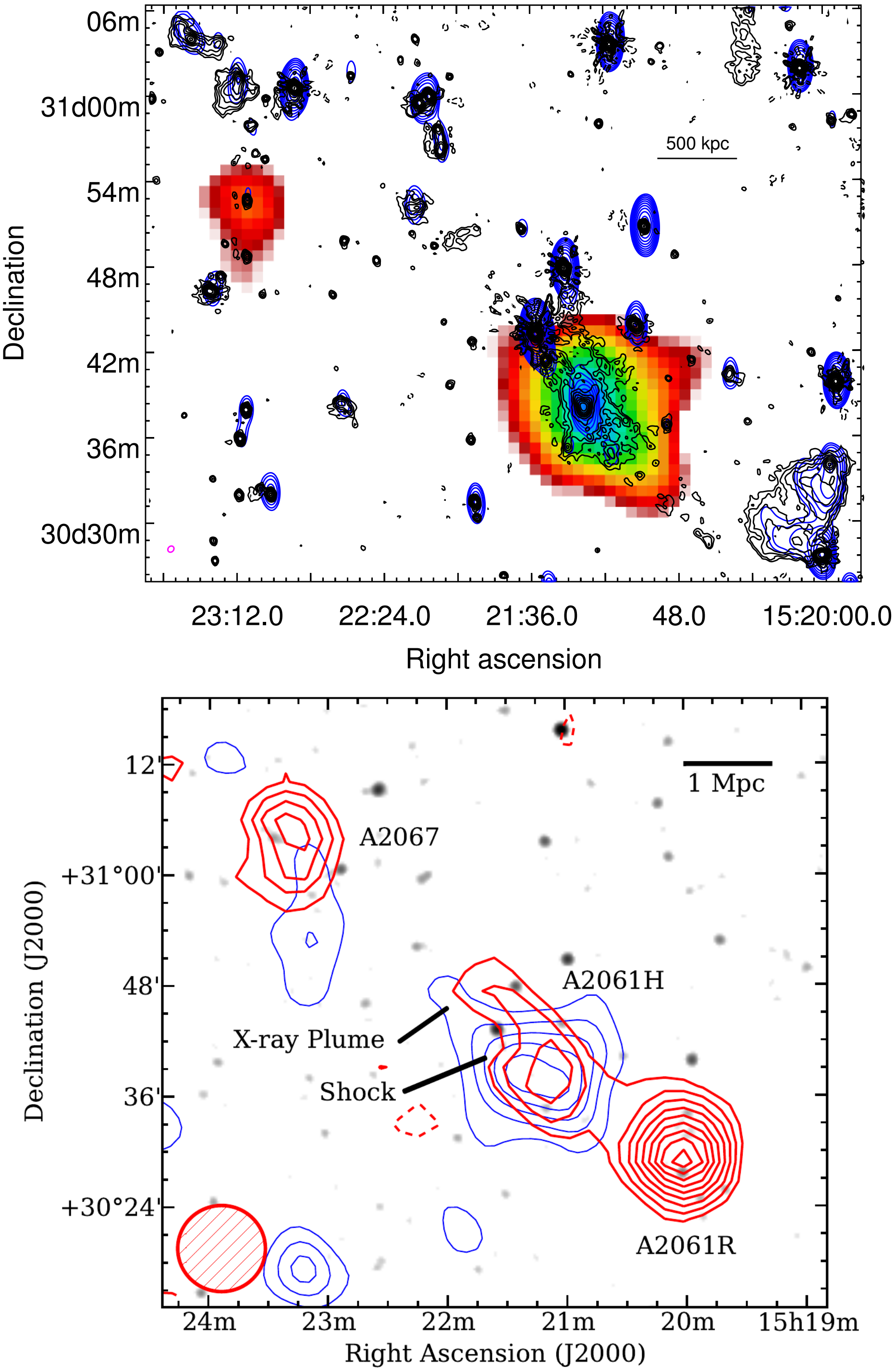

Figure 5.9: Radio and X-ray emission of the galaxy cluster complex Abell 2061 and Abell 2067. **Upper panel:** *Blue contours:* see left image of Fig. 4.6. *Black contours:* see Fig. 5.7. Contours are spaced by $\sqrt{2}$ beginning from $2\sqrt{2}\sigma_{\rm rms}$. The dashed contour line is drawn at $-2\sqrt{2}\sigma_{\rm rms}$. *Colorscale:* Smoothed ROSAT Position Sensitive Proportional Counter (PSPC) image. **Lower panel:** GBT-NVSS residuals at 1.4 GHz, see Fig. 5.2.

Abell 2065, first reported by Farnsworth et al. (2013). In Fig. 5.10 we present the first detailed map of the radio halo in comparison to the map published in Farnsworth et al. (2013) with an LLS of about 0.9 Mpc. The morphology coincides well with the X-ray surface brightness distribution, indicating that the cosmic ray electrons causing the synchrotron emission are mixed with the ICM.

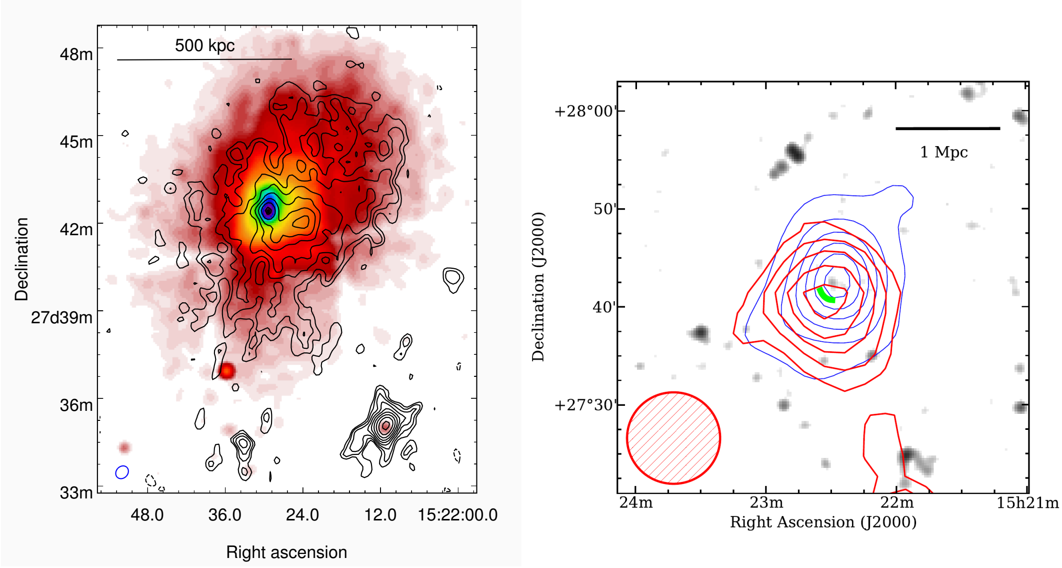

Figure 5.10: Radio and X-ray emission of Abell 2065. **Left image:** *Black contours:* see Fig. 5.7. Contours are spaced by $\sqrt{2}$ beginning from $3\sigma_{\rm rms}$. The dashed contour line is drawn at $-3\sigma_{\rm rms}$. *Colorscale:* See Fig. 5.5 using observation ID 3182. **Right image:** GBT-NVSS residuals at 1.4 GHz, see Fig. 5.2.

The nature of the former radio relic candidate in Abell 2069 is still unclear. The capability of LOFAR to provide sensitivity at resolutions from $\sim 5''$ to $\sim 100''$ reveals that the radio relic candidate is composed of diffuse radio emission and a compact radio source (FIRST J152619.4+292931) to the south associated with the galaxy SDSS J152619+292934 located at a spectroscopic redshift of $z = 0.63$ (Ahn et al., 2012). Interestingly, further north another bright diffuse radio source of similar structure is present showing a clear hotspot to the north, see Fig. 5.11. The radio galaxy SDSS J152611+293904 might be a potential host of the radio lobes and is located at the same redshift as the galaxy cluster Abell 2069 ($z = 0.117$). Its position is indicated with the blue cross. Consequently, we speculate that the radio relic candidate of Abell 2069 is the southern lobe of the rare type of giant radio galaxies (see, e.g., Malarecki et al., 2013). The extent of this potential giant radio galaxy is ~ 2 Mpc. The spectral index of the southern lobe between 153 MHz and 346 MHz is

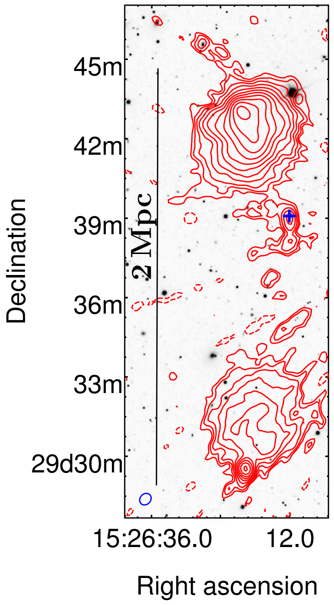

Figure 5.11: LOFAR HBA map of the giant radio galaxy close to Abell 2069. The southern lobe has earlier been classified as radio relic candidate (Giovannini et al., 1999). *Red contours:* see Fig. 5.10. The blue cross marks the position of the potential host galaxy. *Greyscale:* SDSS-III r-band image.

very steep (-1.5 ± 0.3), whereas the significantly brighter northern lobe shows a flatter spectrum (-1.0 ± 0.2).

In Fig. 5.12 we present the radio contours of Abell 2069 overlaid on the Chandra X-ray surface brightness map. Both diffuse radio emission, HA and HB, are clearly visible and extended. The overall morphology of HA and HB is constrained much better than with the WSRT at 346 MHz (see Fig. 5.5). We identified all compact sources embedded in the radio halo in Abell 2069A and the diffuse radio emission in the subcluster Abell 2069B using the GMRT 608 MHz radio map, depicted with green contours in Fig. 5.12. In the following, we discuss our results on the individual diffuse radio sources in Abell 2069.

5.3.2 The radio halo in Abell 2069A

The radio halo in Abell 2069A in our LOFAR HBA map clearly coincides with the X-ray surface brightness distribution. The morphological similarity between the thermal X-ray surface brightness and the relativistic electron distribution seen in the radio emission indicates a correlation of energy densities (Govoni et al., 2001a). Such a

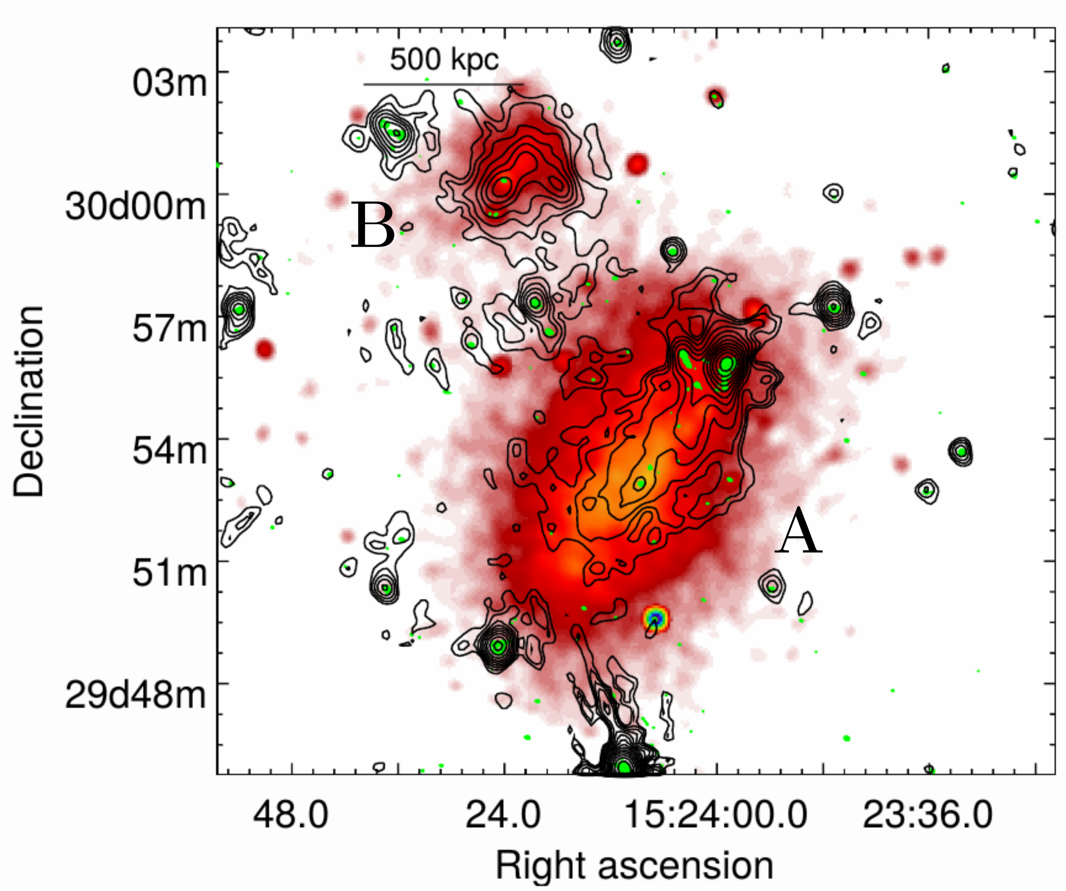

Figure 5.12: *Black contours:* See Fig. 5.10. *Green contours:* GMRT 608 MHz image. The noise level is $\sigma_{\mathrm{rms}} \approx 50\,\mu\mathrm{Jy}$. Contours are spaced by $\sqrt{2}$ beginning from $3\sigma_{\mathrm{rms}}$. The dashed contour line is drawn at $-3\sigma_{\mathrm{rms}}$. The shape of the restoring beam is $5'' \times 4''$ with a position angle of 70°. *Colorscale:* See Fig. 5.5.

relation is expected for radio halos and also for radio mini-halos. First, the X-ray emissivity j_X of the thermal bremsstrahlung in the ICM is related to the electron number density n_{e^-} and the electron temperature T_{e^-} of the ICM as follows

$$j_\mathrm{X} \propto n_{\mathrm{e}^-}^2 \sqrt{k_\mathrm{B} T_{\mathrm{e}^-}}, \tag{5.1}$$

with the Boltzmann constant k_B (see also equation 2.1). For an isothermal ICM, we can assume that the thermal energy density ε_th is proportional to the electron number density and the electron temperature of the ICM, yielding

$$j_\mathrm{X} \propto \varepsilon_\mathrm{th}^2 \left(k_\mathrm{B} T_{\mathrm{e}^-}\right)^{-\frac{3}{2}}. \tag{5.2}$$

Secondly, to derive the radio emissivity j_radio we need to integrate the synchrotron spectrum of a single cosmic ray electron $\frac{dP}{d\nu}$ multiplied by the number density n of the cosmic ray electrons in the energy regime between γ and $\gamma + d\gamma$ over all energies according to our observational frequency coverage. In case of a power-law energy distribution with index p (see equation 2.3), we get

$$j_\mathrm{radio} = \int n\left(\gamma\right) \frac{dP}{d\nu} d\gamma \propto \varepsilon_\mathrm{CRe} B^{\frac{1-p}{2}} \nu^{\frac{1+p}{2}}, \tag{5.3}$$

where ε_CRe is the cosmic ray energy density. For a typical spectral index of $\alpha = -1$ ($p = -3$, see also equation 2.5) we can write

$$j_\mathrm{radio} \propto \varepsilon_\mathrm{CRe} \varepsilon_B \nu^{-1}, \tag{5.4}$$

where ε_B is the magnetic energy density. As discussed in Sec. 2.1, a fraction of the energy dissipated via turbulence during structure formation, e.g, galaxy cluster mergers, may also be channeled into the acceleration of thermal electrons to relativistic energies as well as into the amplification of the intracluster magnetic fields. It is thus feasible to assume that $\varepsilon_\mathrm{CRe} \propto \varepsilon_\mathrm{th}$ and $\varepsilon_B \propto \varepsilon_\mathrm{th}$. Therefore, in an isothermal ICM, the radio emissivity and the X-ray emissivity are correlated.

To compare better the X-ray and the radio emission structure, we divided the area of HA into regions of concentric elliptical annuli centered at the X-ray surface brightness peak. The regions are chosen in such a way that they cover the area where X-ray and radio emission is present at a $> 3\sigma_\mathrm{rms}$ confidence level (see left panel in Fig. 5.13). We subtracted all detected X-ray point sources in the Chandra image according to the procedure described in Sec. 3.7 and smoothed the X-ray image with a Gaussian of a FWHM similar to the restoring beam of our LOFAR HBA map (25″). The achieved

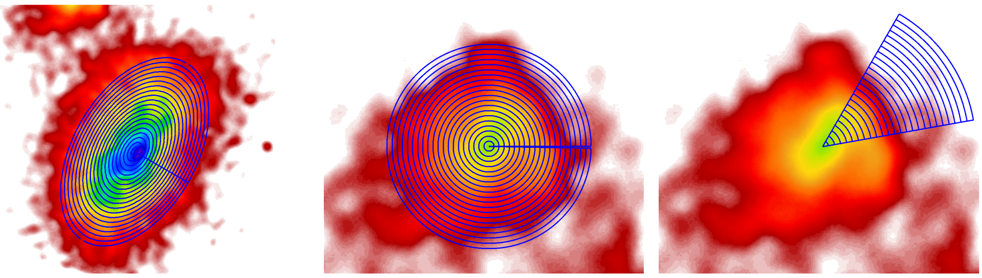

Figure 5.13: *Blue lines:* Regions chosen for measuring the X-ray to radio surface brightness comparison and the emissivity for Abell 2069A (*left panel*) and for Abell 2069B (*middle panel*). The *right panel* shows the regions chosen for measuring the radial X-ray and radio profile across the cold front. *Colorscale:* Subtracted X-ray surface brightness, see Fig. 5.5 and Sec. 3.7.

scatter plot of our X-ray to radio surface brightness comparison for Abell 2069A is presented in the upper panel of Fig. 5.14. Each point of the scatter plots represents the mean of a concentric annulus and each error bar the corresponding standard deviation. We have fitted the correlation to a power-law relation of the type

$$\langle I_{153\,\mathrm{MHz}} \rangle \propto \langle I_{\mathrm{X}} \rangle^{b} \tag{5.5}$$

with the averaged flux density at 153 MHz $\langle I_{153\,\mathrm{MHz}} \rangle$ and the averaged X-ray flux density $\langle I_{\mathrm{X}} \rangle$.

With our fit we measure a slope of $b = 1.21 \pm 0.06$ for HA, excluding the data points measured from annuli dominated by the emission of the radio galaxy G (seen as blue dashed points). Since we have assumed an isothermal ICM, the complex temperature distribution of the ICM in Abell 2069A (Owers et al., 2009) might have an impact on the slope of the relation. Very likely, the slope is affected by emission of the radio halo not recovered in our image. This steepens the X-ray to radio surface brightness relation. We note, that Dolag and Enßlin (2000) derived a slope of $b = 1.26$ in their simulation of a radio halo in a Coma-like galaxy cluster applying a hadronic model (see Sec. 2.4.2). Nevertheless, as discussed in Sec. 2.4.2, we consider a purely hadronic origin unlikely.

Another observable quantity, which characterizes radio halos and also radio mini-halos, is the volume-averaged radio emissivity $\langle J \rangle$, as introduced by

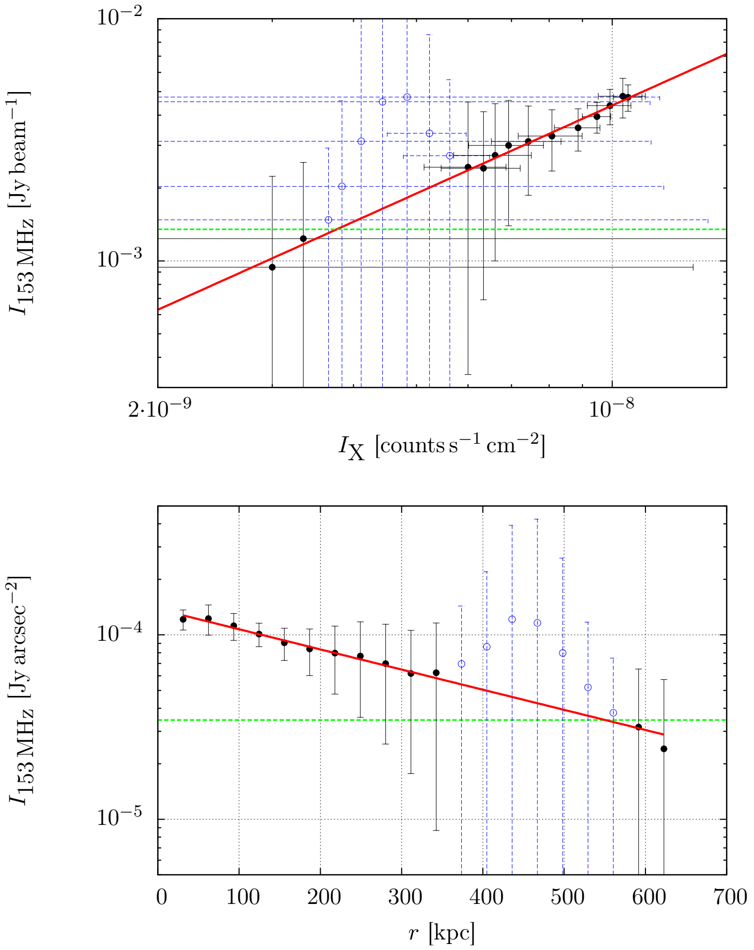

Figure 5.14: *Upper panel:* X-ray to radio surface brightness comparison for the radio halo in Abell 2069A. *Lower panel:* Azimuthally averaged flux density profile for the radio halo in Abell 2069A. Both relations are measured from elliptical concentric annuli at a central frequency of 153 MHz. Each point represents the mean of a concentric annulus and each error bar the corresponding standard deviation. The blue dashed points are contaminated by the radio galaxy G and are therefore excluded from the fit. The red solid line shows the best matching exponential fit to the correlation and the horizontal green dashed line indicates the $3\sigma_{\mathrm{rms}}$ noise level.

Murgia et al. (2009)

$$\frac{\langle J \rangle}{\mathrm{erg\,s^{-1}\,cm^{-3}\,Hz^{-1}}} \simeq 7.7 \cdot 10^{-41}\,(1+z)^{3-\alpha}\,\frac{I_0}{\mathrm{\mu Jy\,arcsec^{-2}}}\left(\frac{r_e}{\mathrm{kpc}}\right)^{-1}, \tag{5.6}$$

where the k-correction (see equation 2.13) and the cosmological dimming of the surface brightness (see, e.g., Calvi et al., 2014) are taken into account by the factor $(1+z)^{3-\alpha}$ and I_0 is the radio peak flux density. For the quantity of the volume-averaged radio emissivity it is supposed that all the emission of a diffuse radio source is distributed within a sphere of radius $3r_e$, where r_e is the e-folding radius. In contrast to the X-ray to radio surface brightness relation, this quantity is quite robust against the sensitivity of the radio map. Typically, radio halos have a volume-averaged radio emissivity of $\langle J \rangle \approx 10^{-42}\,\mathrm{erg\,s^{-1}\,cm^{-3}\,Hz^{-1}}$ (Murgia et al., 2009), see Fig. 2.3, assuming a spectral index of $\alpha = -1$. We are able to estimate the radio peak flux density I_0 through fitting the flux density profile of HA

$$I_{\mathrm{HA}} = I_0 e^{-\frac{r}{r_e}}, \tag{5.7}$$

as described in Orrú et al. (2007). The fit for the emissivity is depicted in the lower panel of Fig. 5.14 and provides a peak flux density of $I_0 = 138 \pm 3\,\mathrm{\mu Jy\,arcsec^{-2}}$ using an e-folding radius of $r_e = 398 \pm 17\,\mathrm{kpc}$. We thus calculate a radio emissivity of $\langle J_{\mathrm{HA}} \rangle \approx 4 \cdot 10^{-41}\,\mathrm{erg\,s^{-1}\,m^{-3}\,Hz^{-1}}$ for HA at a central frequency of 153 MHz. The volume-averaged radio emissivity of HA is thus in the regime of typical radio halos, in particular it is comparable to the emissivity of the radio halo in Abell 2744 (Govoni et al., 2001a), assuming a spectral index of $\alpha = -1$.

Some faint point sources are embedded in HA, appearing as brightness peaks in the extended radio emission. The overall peak of the radio emission in HA is associated with the BCG of Abell 2069A as well as with the X-ray surface brightness peak. The second BCG of Abell 2069A also shows a weak radio feature ($< 0.5\,\mathrm{mJy}$) in our GMRT map at 608 MHz (not shown here, observational details in Sec. 3.3.3). So both BCGs are radio sources. Their contribution to the halo emission is still negligible. The source G2 (see Fig. 5.4 for a comparison at 346 MHz) is again the brightest embedded source in HA at 153 MHz with an integrated flux density of $185 \pm 19\,\mathrm{mJy}$. We derived the spectral index of G2, including the analysis of the Abell 2069 field with the GMRT at 608 MHz, to be -1.6 ± 0.1. Such steep spectra, as in case of source G2, are known from dying radio galaxies, especially if the emission is dominated by the lobes (see, e.g., Parma et al., 2007; Brienza et al., 2016).

In our WSRT map at 346 MHz we detected a radio to X-ray emission peak offset to HA. Such an offset may indicate that the major merger is still in an early or very late stage (Govoni et al., 2009). With our LOFAR HBA map, which we consider more reliable, we do not confirm the radio to X-ray emission peak offset of HA.

Cassano et al. (2010) showed that galaxy clusters with and without radio halos populate different areas when comparing dynamical parameters of the galaxy cluster derived from a set of morphological parameters of the X-ray emission. The concentration parameter

$$C = \frac{S\left(r < 100\,\mathrm{kpc}\right)}{S\left(r < 500\,\mathrm{kpc}\right)} \tag{5.8}$$

is comparing the surface brightness in the direct vicinity within 100 kpc of the X-ray peak $S\left(r < 100\,\mathrm{kpc}\right)$ with the surface brightness in the ambient regions up to 500 kpc $S\left(r < 500\,\mathrm{kpc}\right)$ (Santos et al., 2008). Compact cores should provide a much higher concentration parameter than galaxy clusters, which show a flatter surface brightness distribution. The centroid shift

$$w = \frac{1}{R_{\mathrm{ap}}}\sqrt{\frac{1}{N-1}\sum_{j=1}^{N}\left(\Delta_j - \langle\Delta\rangle\right)^2} \tag{5.9}$$

is a measure of the displacement of the system's X-ray centroid (O'Hara et al., 2006; Poole et al., 2006) from the X-ray peak, where R_{ap} is the aperture radius, N is the number of apertures, Δ_j is the distance between the X-ray centroid and the X-ray peak of the jth aperture, and $\langle\Delta\rangle$ is the mean distance between the X-ray centroid and the X-ray peak of all apertures. Finally, the power ratio P_3/P_0 is a component of the multipole decomposition of the two-dimensional projected mass distribution P_j inside R_{ap}

$$P_j = \frac{a_j^2 + b_j^2}{2j^2 R_{\mathrm{ap}}}, \tag{5.10}$$

where the moments a_j and b_j are defined by

$$a_j = \iint\limits_{r' \leq R_{\mathrm{ap}}} S\left(\vec{r'}\right) \cdot \left(r'\right)^j \cos\left(j\varphi'\right) d^2\vec{r'} \tag{5.11}$$

$$b_j = \iint\limits_{r' \leq R_{\mathrm{ap}}} S\left(\vec{r'}\right) \cdot \left(r'\right)^j \sin\left(j\varphi'\right) d^2\vec{r'}. \tag{5.12}$$

Here, the vector $\vec{r} = (r,\varphi)$ consists of the distance r and the angle φ relative to the galaxy cluster's centroid. The normalizing component P_0 is basically described by the total intensity a_0 within R_{ap}

$$P_0 = a_0 \ln R_{\mathrm{ap}}. \tag{5.13}$$

The power ratio P_3/P_0 is sensitive to substructures in the surface brightness distribution. In the sample of Cassano et al. (2010) the median values of each parameter $w = 0.012$, $C = 0.2$, and $P_3/P_0 = 1.2 \cdot 10^{-7}$ are separating galaxy clusters with and without radio halos using $R_{\mathrm{ap}} = 500\,\mathrm{kpc}$. So, the galaxy clusters with radio halos tend to be more disturbed. We have measured the concentration parameter, the centroid shift, and the power ratio of Abell 2069A to be $C = 0.078 \pm 0.002$, $w = 0.018 \pm 0.002$, and $P_3/P_0 = (1.8 \pm 0.6) \cdot 10^{-8}$ in the point source subtracted Chandra image using $R_{\mathrm{ap}} = 500\,\mathrm{kpc}$, respectively. The errors are estimated through measuring all the parameters in different X-ray images smoothed with a Gaussian kernel with a FWHM of $[2.5, 5, 7.5, 10, 12.5, 15, 17.5, 20]''$. This puts Abell 2069A in the group of the disturbed galaxy clusters (see upper panel in Fig. 5.15), as regards to the concentration parameter and the centroid shift. This is in agreement with the presence of a radio halo. On the other hand, Abell 2069A occupies an empty area in the C-P_3/P_0 diagram, indicating that, although it is disturbed, not much substructure is present (see lower panel in Fig. 5.15). This might suggest that Abell 2069A is in a transition state between a disturbed and a relaxed configuration (or vice versa), for instance, at a late merger state, where substructures have been already resolved. The irregular temperature distribution of Abell 2069A (Owers et al., 2009) still puts it clearly into the branch of the disturbed galaxy clusters. Moreover, the galaxy cluster sample we are comparing with in the morphology parameter plots lies within a redshift range from $z = 0.20$ to 0.35, whereas Abell 2069A is located at a redshift of $z = 0.116$. Cassano et al. (2010) considered that, e.g., the power ratio might evolve with redshift.

We measure a flux density of the radio halo in Abell 2069A of $128 \pm 25\,\mathrm{mJy}$, subtracting the contributions of the sources G1, G2 and G3 and excluding the potential bridge area, see Sec. 5.3.3. The spectral index of HA between 153 MHz and 346 MHz thus ranges from -1.4 to -2.0, taking into account the large uncertainties of our flux density measurements at 346 MHz. So it is quite likely that HA belongs to the class of ultra-steep spectrum radio halos ($\alpha \lesssim -1.6$). In the framework of the turbulent re-acceleration model this again suggests that Abell 2069A is in a late merger state (Donnert et al., 2013). A steep spectrum radio halo can not be explained by the hadronic model, since the energy budget of the cosmic ray electrons producing the observed synchrotron emission is implausible for typical cluster magnetic field strengths of $\sim\mu\mathrm{G}$ (Brunetti, 2004).

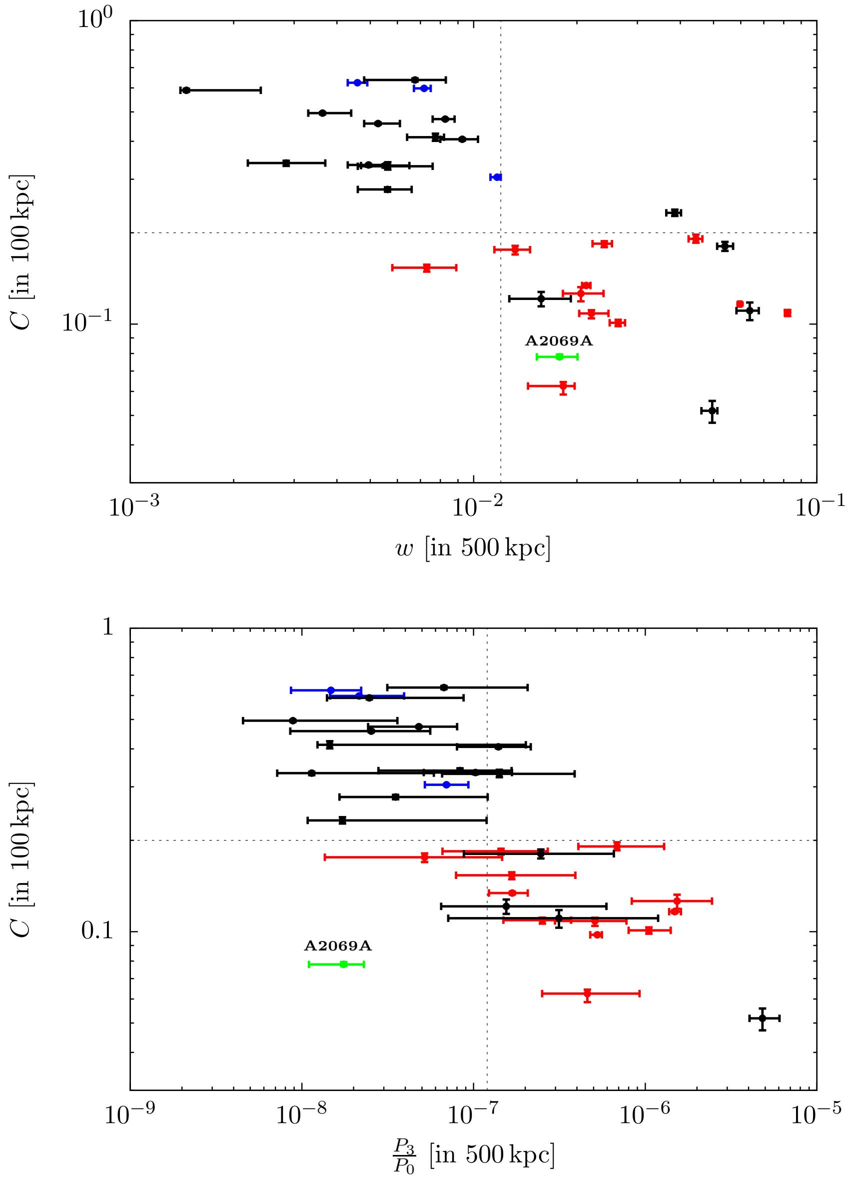

Figure 5.15: X-ray morphology parameters. *Upper panel:* Concentration parameter C versus centroid shift w. *Lower panel:* Concentration parameter C versus power ratio P_3/P_0. Galaxy clusters possessing radio halos are colored in red, mini-halos are colored in blue, and no radio emission are colored in black. The galaxy cluster component Abell 2069A is indicated with a green point. Data adapted from Cassano et al. (2010).

5.3.3 A potential bridge of radio emission in Abell 2069

Between the X-ray surface brightness peaks of both galaxy cluster components we have recovered low surface brightness emission, which seems to connect the diffuse radio emission in both galaxy cluster components. To figure out whether a diffuse “bridge” connects both diffuse radio features in A and B, we need to exclude whether we just see several unresolved faint compact sources located in that area and detected in our GMRT map at 608 MHz (see again green contours in Fig. 5.12). There are only a few galaxy clusters known to exhibit a “radio bridge”. All radio bridges known so far only reside in the area between radio halos and radio relics (see, e.g., Kim et al., 1989; Govoni et al., 2005). In such a scenario, the merger episode of a galaxy cluster could trigger shock waves in the ICM that could cause both the radio halo and the radio relics (Feretti et al., 2012).

5.3.4 The diffuse radio emission in Abell 2069B

After our analysis of the WSRT 346 MHz data, see Sec. 5.2, the nature of the diffuse radio source HB remained uncertain. The WSRT map did not allow us to draw any conclusions, whether HB could be an old radio galaxy with an unusual morphology or whether the radio emission is related to the ICM. In order to constrain better the nature of the source HB we have reimaged the calibrated LOFAR HBA data at the highest possible resolution using uniform weighting. We have depicted the high resolution radio contours of our LOFAR HBA map overlaid on an SDSS-III r-band image in the upper panel of Fig. 5.16. At a first glance, the ‘V’-shaped X-ray emission is silimar to the contours of the radio map. In this map, we recover a flux density of HB of about 40 mJy. Furthermore, we have marked all galaxies with a redshift of $z \sim 0.11$ with a cyan cross in the upper panel of Fig. 5.16. These galaxies are likely members of the galaxy cluster. From this map, we conclude that there is no hint for an active radio galaxy or its radio lobes causing the diffuse radio emission in Abell 2069B. Interestingly, the BCG in Abell 2069B shows only a very weak radio feature of ~ 0.5 mJy at 608 MHz and ~ 0.8 mJy at 322 MHz in our radio maps achieved with the GMRT, see again upper panel of Fig. 5.16. We expect a contribution from the BCG in Abell 2069B of roughly ~ 1.5 mJy at 153 MHz, assuming a mean spectral index of $\alpha_{\mathrm{BCG\_B}} \approx -0.8$. This corresponds to a flux density contamination of the order of $\sim 1\%$ and is thus negligible for the flux density estimate of the diffuse radio emission. Therefore, HB is not an AGN, but it might stem from fossil radio plasma of a dying or already radio-quiet AGN.

In our LOFAR HBA map at an intermediate resolution of $28'' \times 24''$, the whole

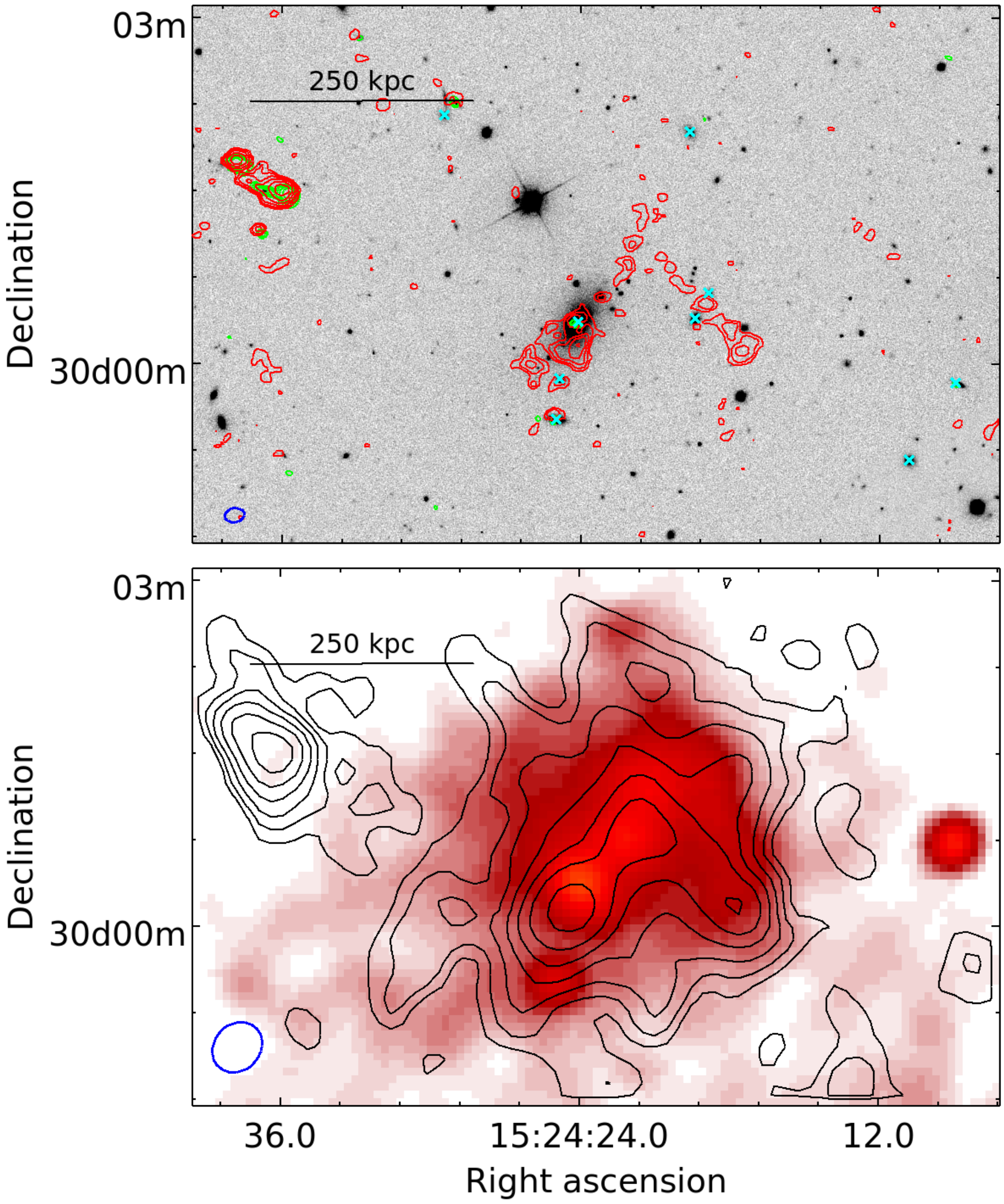

Figure 5.16: Zoom into the Abell 2069B region. **Upper panel:** *Red contours:* LOFAR HBA map at a central frequency of 153 MHz. The noise level is $\sigma_{\rm rms} \approx 170\,\mu$Jy. Contours are spaced by $\sqrt{2}$ beginning from 170 μJy. The dashed contour line is drawn at $-3\sigma_{\rm rms}$. The shape of the restoring beam is $7'' \times 5''$ with a position angle of 98°. *Green contours:* See green contours in Fig. 5.12. *Greyscale:* SDSS-III (Data release 12) r-band image. *Cyan crosses:* Location of galaxies associated with Abell 2069. **Lower panel:** See Fig. 5.5 for the background colorscale image, and see Fig. 5.12 for the black contours.

projected area of the ICM, indicated by the X-ray surface brightness distribution, is filled by diffuse radio emission (see lower panel in Fig. 5.16). In this map, we recover a flux density of HB of $95 \pm 9\,\mathrm{mJy}$. We estimate an ultra-steep spectral index of HB of -2.2 ± 0.3 between 153 MHz and 346 MHz. Such an ultra-steep spectral index is typical of fossil radio plasma (Parma et al., 2007). However, the radio emission shows an LLS of about 450 kpc. This raises the question if this fossil radio plasma could have been redistributed to distances of several $\sim 100\,\mathrm{kpc}$ throughout the ICM.

In order to check whether HB may be related to the ICM, we repeated the analysis of HA and constructed regions with concentric circular annuli spaced by $6''$ (see middle panel in Fig. 5.13). Our results for the X-ray to radio surface brightness comparison and the emissivity of HB are presented in the upper panel and the lower panel of Fig. 5.17, respectively. It is evident, that both X-ray emission and radio emission in Abell 2069B are correlated. We found an exponential slope of $b = 1.77 \pm 0.04$ for the X-ray to radio surface brightness comparison and fitted a peak flux density $I_0 = 264 \pm 7\,\mu\mathrm{Jy\,arcsec^{-2}}$ using an e-folding radius of $r_e = 130 \pm 5\,\mathrm{kpc}$. This X-ray to radio surface brightness correlation is evidence that the relativistic electrons causing the synchrotron emission are mixed with the ICM of Abell 2069B. We therefore exclude that the emission in Abell 2069B is only caused by fossil radio lobes of a formerly active AGN phase. From the fitted peak flux density I_0 we calculate a radio emissivity of $\langle J_{\mathrm{B}} \rangle \approx 3 \cdot 10^{-40}\,\mathrm{erg\,s^{-1}\,m^{-3}\,Hz^{-1}}$ at a central frequency of 153 MHz. This is comparable to the emissivity of the radio mini-halo in Abell 2029 if we extrapolate its flux density to 153 MHz, assuming a spectral index of $\alpha = -1$. Furthermore, the volume-averaged radio emissivity of HB is an order of magnitude higher than typical volume-averaged radio emissivities of radio halos (Murgia et al., 2009). We thus suggest that HB belongs to the class of radio mini-halos.

Radio mini-halos are typically located in cool core galaxy clusters where a powerful AGN is present. Govoni et al. (2009) thus speculated about a tendency of cool core clusters with a more powerful AGN to host more powerful radio mini-halos. In the case of Abell 2069B the radio power of the BCG is very low in contrast to the brightness of the radio mini-halo. Govoni et al. (2009) reported a “radio-off” mini-halo candidate in Abell 1413, but not a single example of a weak BCG emission in a cluster possessing a radio mini-halo has been confirmed yet. Since AGNs are known to run through multiple cycles of activity (see, e.g., Murgia et al., 2011), we might be currently witnessing a recent activity decrease from a formerly active AGN or a recent activity increase from a formerly inactive AGN.

Alternatively, the hadronic model (see Sec. 2.4.2) may provide an explanation of the origin of radio mini-halos. Assuming a spheroidal shape for Abell 2069A (semimajor

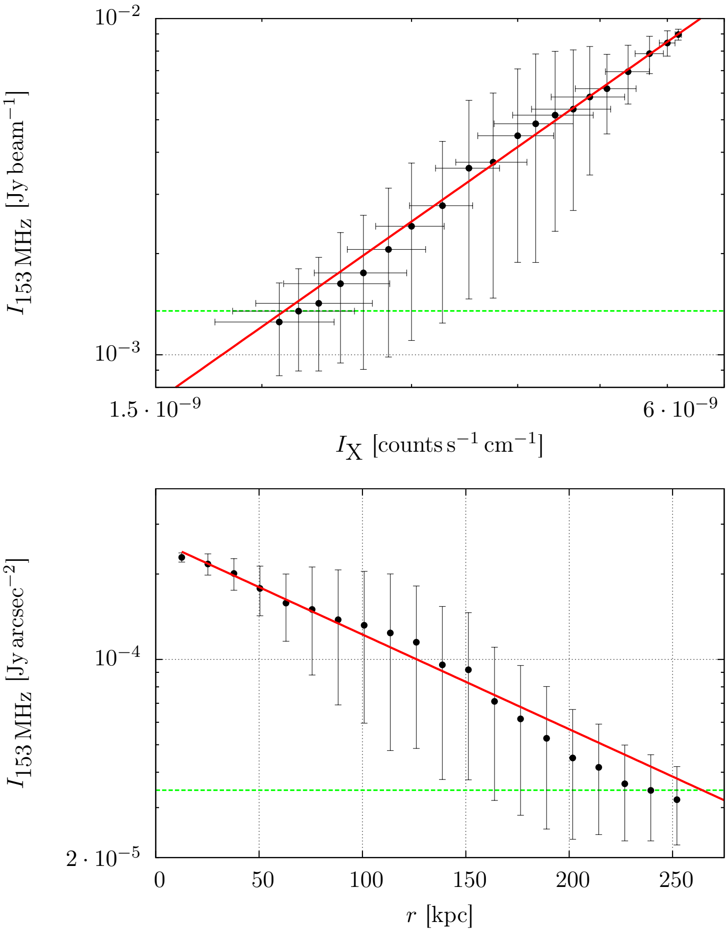

Figure 5.17: *Upper panel:* X-ray to radio surface brightness comparison for the diffuse radio emission Abell 2069B from circular concentric annuli at a central frequency of 153 MHz, see upper panel in Fig. 5.14 *Lower panel:* Azimuthally averaged flux density profile for the diffuse radio emission in Abell 2069B from circular concentric annuli at a central frequency of 153 MHz, see lower panel of Fig. 5.14.

axis $a_{\mathbf{A}}$ and semiminor axis $b_{\mathbf{A}}$) and a spherical shape for Abell 2069B (radius $r_{\mathbf{B}}$) we estimate the mass ratio of both galaxy cluster components to be $(L_{\mathrm{X},\mathbf{A}}/L_{\mathrm{X},\mathbf{B}})^2 \cdot \left(a_{\mathbf{A}}^2 b_{\mathbf{A}}/r_{\mathbf{B}}^3\right) \approx 10^4$ (fractional luminosity of 0.1). We thus consider a hadronic origin of HB unlikely, because if secondary electrons are able to produce such a luminous radio emission in such a poor X-ray environment, one should see "hadronic" radio halos in virtually every galaxy cluster. The presence of radio halos of that strength in nearly all galaxy clusters can be excluded by current observational evidence (see Sec. 2.3.1). Additionally, the ultra-steep spectrum of the radio mini-halo rules out a purely hadronic origin of the radio mini-halo, as discussed for HA (see Sec. 5.3.2). To produce HB we need at least a second ingredient, like turbulence, which is enhancing the brightness of HB. Current so-called "hybrid" models take this into account. The advantage of secondary electrons serving as seed electrons for turbulent re-acceleration is a much lower γ-ray emission, which is not detectable within the current FERMI limits (Pinzke et al., 2015).

The cold front found in the cluster component B to the northwest (Owers et al., 2009) can be considered as a hint for an ongoing internal gas sloshing present in Abell 2069B. Simulations by ZuHone et al. (2013) show that gas sloshing potentially induces turbulence, which eventually causes radio emission. We thus propose a scenario, where gas sloshing subsequently could have gathered mildly relativistic (or "aged") electrons from the fossil plasma reservoir provided during a former active phase of an AGN in Abell 2069B and re-distributed it within the entire subcluster volume. An additional supply of seed electrons from the fossil plasma reservoir could explain the high emissivity of HB. Moreover, the steep slope of the X-ray to radio surface brightness comparison indicates that the magnetic field strength or the particle density of the seed electrons decrease stronger than the thermal energy density of the ICM, see discussion in Sec. 5.3.2. The original distribution of the fossil plasma and an ongoing gas sloshing in the subcluster may have a stronger impact on the radio emission distribution of HB than the distribution of the thermal plasma. Furthermore, gas sloshing can significantly enhance the magnetic field strength in different parts of the subcluster (ZuHone et al., 2015).

Simulations by ZuHone et al. (2013) show that radio mini-halos created by turbulence in a sloshing core trace the cold front and are confined within its boundary. We compared the radio profile of HB in our LOFAR HBA map with the X-ray profile in our Chandra map in the region of the cold front (see right panel of Fig. 5.13). We have smoothed the X-ray image with a Gaussian to a similar restoring beam size as the LOFAR HBA map (FWHM of $25''$). Interestingly, the radio emission of HB drops coincidently with the X-ray surface brightness at the location of the cold front, see

Fig. 5.18. This suggests that HB is caused by re-acceleration of fossil plasma due to

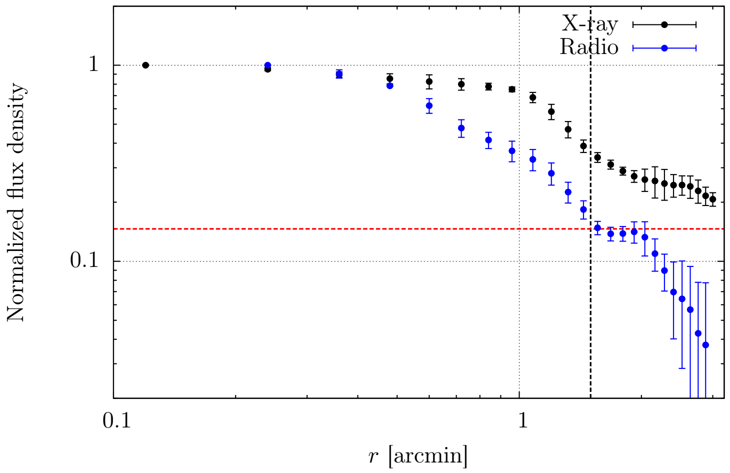

Figure 5.18: Azimuthally averaged radio and X-ray profile at the cold front in Abell 2069B. The profile is measured from the regions depicted in the right panel of Fig. 5.13. The red dashed line marks the $3\sigma_{\rm rms}$ level of the radio map and the black dashed line the proposed location of the cold front. For illustration purposes both profiles are normalized to 1.

turbulence induced by internal gas sloshing in Abell 2069B. Since HB shows an ultra-steep spectrum, we suspect that the turbulence has already decayed, leading to a less efficient re-acceleration (ZuHone et al., 2013). Moreover, there is no further injection of seed electrons from an active AGN.

5.4 Conclusions on Abell 2069

Abell 2069 is a complex merging galaxy cluster displaying two major X-ray peaks. In the WSRT 346 MHz Legacy Survey we discovered previously unclassified diffuse radio features, in both galaxy cluster components. In order to classify these sources we performed a comprehensive follow-up analysis with the GMRT at 322 MHz and 608 MHz as well as with the LOFAR HBA at 153 MHz. We complemented our study with archival X-ray data observed with the Chandra X-ray telescope.

We decomposed the diffuse radio patch discovered by Farnsworth et al. (2013) at 1.4 GHz with our WSRT 346 MHz map into a multitude of sources, in particular a dying radio galaxy, a radio halo with evidence of an ultra-steep spectrum in the main cluster component, and an ultra-steep spectrum radio mini-halo in the subcluster component. The measured flux densities and spectral indicies of source G2, the radio halo and the radio mini-halo in Abell 2069 in this work are listed in in Tab. 5.2.

Table 5.2: Flux densities of selected sources in Abell 2069 as measured with the LOFAR HBA at 153 MHz, the WSRT at 346 MHz, the GMRT at 322 MHz, and the GMRT at 608 MHz.

ID	$I_{153\,\mathrm{MHz}}$	$I_{322\,\mathrm{MHz}}$	$I_{346\,\mathrm{MHz}}$	$I_{608\,\mathrm{MHz}}$	α_{153}^{346}	α_{153}^{1400}
	[mJy]					
HA	128 ± 25	–	$25 \ldots 39$	–	$-1.4 \ldots -2.0$	–
HB	95 ± 9	–	15 ± 2	–	-2.2 ± 0.3	–
G2	185 ± 19	52 ± 6	–	16 ± 1	$-1.6 \pm 0.1^{\dagger}$	

Columns. (2,3,4,5): measured flux density at the indicated frequency measured in this work, (6): measured flux density by Farnsworth et al. (2013), (7,8): spectral index between the indicated frequencies measured in this work

†obtained from a power-law fit using all available frequencies

The morphological analysis suggests an active merger in the main cluster component Abell 2069A with signs of relaxation. This is supported by the steep spectrum of the radio halo, which might indicate a late merger state as predicted from simulations of the turbulent re-acceleration model by Donnert et al. (2013). The cold front in the subcluster component B indicates the presence of gas sloshing. Turbulence and magnetic field amplification in cold sloshing cores could have redistributed and re-accelerated old cosmic ray electrons provided from a former active phase of an AGN in B. A minor or off-axis merger in B, irrespective of the interaction between both cluster parts, may have evoked gas sloshing in B without disrupting its cool core (Poole et al., 2008), if present. Nevertheless, the dynamical state of the whole galaxy cluster appears to be rather complex. According to the low peculiar velocity of the subcluster B with respect to the mean cluster redshift of A, both are potentially undergoing a merger. It is uncertain, whether the subcluster component is still in its first encounter or has already passed the core of the main cluster component. Thus, the interaction of the subcluster with the much more massive main component might already have induced sufficient energy into the intracluster medium of B to re-accelerate cosmic ray electrons, subsequently giving rise to the particularly remarkable radio mini-halo discovered. Signs of a "radio bridge" in the low-density environment between both cluster components support the idea that part of the energy is dissipated via turbulence between both galaxy cluster components, leading to an acceleration of cosmic ray electrons to highly relativistic energies.

6 Summary and Outlook

In this work we studied diffuse radio emission in ten galaxy clusters at low frequencies ($\nu < 1.4\,\mathrm{GHz}$). Diffuse radio emission in galaxy clusters, like radio halos, radio relics, and radio mini-halos, trace highly relativistic electrons in the ICM. With decreasing observing frequency, we can map the distribution of relativistic electrons at decreasing energies. Since aging electron populations lose electrons at the higher end of their energy distribution, observations at very low frequencies allow us to study old electron populations.

The known sample of diffuse radio sources in galaxy clusters is still small (~ 100). For most diffuse radio sources, information is only available 1.4 GHz. Since the WSRT was one of the best suited instruments offering high quality radio observations in the low frequency regime, we have analyzed the spectrum and the morphology of diffuse radio emission in ten galaxy clusters in the framework of the WSRT 346 MHz Legacy Survey. We have confirmed the radio relics in Abell 115, Abell 1240, and Abell 2061; the radio halos in Abell 1758, Abell 2218, Abell 2219, Abell 2254, and Abell 2319; and classified a former radio relic candidate in RXC J1053.7+5452 as a radio galaxy. Furthermore, our analysis of the WSRT 346 MHz Legacy Survey data revealed that the galaxy cluster Abell 2069 shows a richness of previously unknown radio features. Subsequently, we performed deep radio follow-up observations of Abell 2069 with the GMRT at 322 MHz and 608 MHz as well as with the LOFAR HBA at 153 MHz. We complemented our study with Chandra ACIS-I archival data.

The galaxy cluster Abell 2069 is composed of a main cluster component and a much less massive subcluster component (A2069B). We revealed that both galaxy cluster components possess diffuse radio emission. The main cluster component shows clear signs of an ongoing merger and the low peculiar velocity of the subcluster component with respect to the main cluster component suggests another ongoing merger of both components.

We observed Abell 2069 with the LOFAR HBA to further investigate the structure of the radio sources. LOFAR is a novel telescope. It provides high sensitivity at low frequencies and allows one to vary the resolution over a wide range of angular scales. The calibration of LOFAR data and the imaging of the telescope's large FoV is challenging. In our LOFAR maps the diffuse radio emission in the main cluster component shows an LLS of about 900 kpc and its brightness distribution is clearly correlated with the X-ray surface brightness. We classify the diffuse emission in the cluster's main component as a radio halo. A steep-spectrum radio galaxy embedded in the radio halo emission is difficult to separate in our WSRT maps at 346 MHz and therefore causes large uncertainties. We thus estimate the flux density of the radio halo to be in between 25 mJy and 39 mJy at 346 MHz. In our LOFAR HBA map we measure a flux density of 128 ± 25 mJy at 153 MHz. This corresponds to a spectral index of $\alpha_{153}^{346} < -1.4$. Thus, the radio halo in the main cluster component may belong to the small population of ultra-steep spectrum radio halos. Hadronic models can not explain an ultra-steep spectrum, hence the spectral index of the radio halo in the main cluster component strongly disfavors a hadronic origin. Re-acceleration models suggest a late merger state for the main cluster component.

The diffuse radio emission of an LLS of about 450 kpc in the subcluster component is also mixed with the subcluster's ICM and is confined within the subcluster's cold front. Its flux density amounts to 15 ± 2 mJy at 346 MHz and 95 ± 9 mJy at 153 MHz, thus showing an ultra-steep spectrum ($\alpha = -2.2 \pm 0.3$). Due to its small size and its high radio emissivity, we suggest that this source belongs to the class of radio mini-halos. The absence of a powerful central AGN in the subcluster is untypical for a radio mini-halo. The cold front suggests that internal gas sloshing is present in the subcluster component, which could have led to bulk motions and turbulence in the ICM. Simulations by ZuHone et al. (2013) show that gas sloshing may redistribute and re-accelerate the fossil radio plasma from a former AGN phase to cause the radio emission. Alternatively, we speculate that the interaction of both galaxy cluster components may have induced turbulence in the ICM or has caused gas sloshing in the subcluster. Abell 2069 is the second case of a double-halo system, but the first case in which a single galaxy cluster shows both a radio halo and a radio mini-halo.

Deep radio observations together with X-ray observations are a powerful tool for shedding light on the intrinsic dynamics of the ICM in galaxy clusters. Our analysis of the merging galaxy cluster Abell 2069 with the LOFAR HBA shows the outstanding capabilities of the instrument. It allows us to study old electrons in diffuse structures in great detail with unprecedented sensitivity. Potentially, more ultra-steep spectrum low surface brightness radio sources, like the one in Abell 2069B, are still awaiting discovery. With LOFAR we are able to reveal more of those ultra-steep spectrum radio sources than it had been possible by present observations at GHz frequencies. Thus, we are entering a new era of low frequency science which may fundamentally change our current picture of the origin of synchrotron emission in galaxy clusters.

Bibliography

H. M. Abdelsalam, P. Saha, and L. L. R. Williams. Nonparametric Reconstruction of Abell 2218 from Combined Weak and Strong Lensing. *Astronomical Journal*, 116: 1541–1552, October 1998.

G. O. Abell. The Distribution of Rich Clusters of Galaxies. *Astrophysical Journal Supplement*, 3:211, May 1958.

G. O. Abell, H. G. Corwin, Jr., and R. P. Olowin. A catalog of rich clusters of galaxies. *Astrophysical Journal Supplement*, 70:1–138, May 1989.

M. Ackermann, M. Ajello, A. Allafort, L. Baldini, J. Ballet, et al. GeV Gamma-ray Flux Upper Limits from Clusters of Galaxies. *Astrophysical Journal Letters*, 717: L71–L78, July 2010.

M. Ackermann, M. Ajello, A. Albert, A. Allafort, W. B. Atwood, et al. Search for Cosmic-Ray-induced Gamma-Ray Emission in Galaxy Clusters. *Astrophysical Journal*, 787:18, May 2014.

C. P. Ahn, R. Alexandroff, C. Allende Prieto, S. F. Anderson, T. Anderton, B. H. Andrews, É. Aubourg, S. Bailey, E. Balbinot, R. Barnes, and et al. The Ninth Data Release of the Sloan Digital Sky Survey: First Spectroscopic Data from the SDSS-III Baryon Oscillation Spectroscopic Survey. *Astrophysical Journal Supplement*, 203:21, December 2012.

H. Akamatsu, J. de Plaa, J. Kaastra, Y. Ishisaki, T. Ohashi, M. Kawaharada, and K. Nakazawa. Properties of the Intracluster Medium of Abell 3667 Observed with Suzaku XIS. *Publications of the Astronomical Society of Japan*, 64:49, June 2012.

J. Anderson, R. Beck, M. Bell, G. de Bruyn, K. Chyzy, J. Eislöffel, T. Enßlin, A. Fletcher, M. Haverkorn, G. Heald, A. Horneffer, A. Noutsos, W. Reich, A. Scaife, and the LOFAR collaboration. The LOFAR Magnetism Key Science Project. *ArXiv e-prints*, March 2012.

M. Arnaud. Non thermal emission in clusters of galaxies. *Memorie della Societa Astronomica Italiana*, 79:170, 2008.

Y. Ascasibar and M. Markevitch. The Origin of Cold Fronts in the Cores of Relaxed Galaxy Clusters. *Astrophysical Journal*, 650:102–127, October 2006.

M. Bacchi, L. Feretti, G. Giovannini, and F. Govoni. Deep images of cluster radio halos. *Astronomy and Astrophysics*, 400:465–476, March 2003.

M. G. Baring. Diffusive Shock Acceleration : the Fermi Mechanism. In Y. Giraud-Heraud and J. Tran Thanh van, editors, *Very High Energy Phenomena in the Universe; Moriond Workshop*, page 97, 1997.

R. Barrena, W. Boschin, M. Girardi, and M. Spolaor. The dynamical status of the galaxy cluster Abell 115. *Astronomy and Astrophysics*, 469:861–872, July 2007.

R. Barrena, M. Girardi, W. Boschin, and M. Dasí. Internal dynamics of Abell 1240: a galaxy cluster with symmetric double radio relics. *Astronomy and Astrophysics*, 503:357–371, August 2009.

P. D. Barthel, M. Vestergaard, and C. J. Lonsdale. Radio imaging of core-dominated high redshift quasars. *Astronomy and Astrophysics*, 354:7–16, February 2000.

R. H. Becker, D. J. Helfand, R. L. White, M. D. Gregg, and S. A. Laurent-Muehlheisen. The FIRST Survey Catalog, Version 12Feb16 (Becker+ 2012). *VizieR Online Data Catalog*, 8090:0, 2012.

T. C. Beers, M. J. Geller, and J. P. Huchra. Galaxy clusters with multiple components. II - Abell 115. *Astrophysical Journal*, 264:356–363, January 1983.

V. S. Berezinsky, P. Blasi, and V. S. Ptuskin. Clusters of Galaxies as Storage Room for Cosmic Rays. *Astrophysical Journal*, 487:529–535, October 1997.

V. Bharadwaj, T. H. Reiprich, G. Schellenberger, H. J. Eckmiller, R. Mittal, and H. Israel. Intracluster medium cooling, AGN feedback, and brightest cluster galaxy properties of galaxy groups. Five properties where groups differ from clusters. *Astronomy and Astrophysics*, 572:A46, December 2014.

S. Bhatnagar, T. J. Cornwell, K. Golap, and J. M. Uson. Correcting direction-dependent gains in the deconvolution of radio interferometric images. *Astronomy and Astrophysics*, 487:419–429, August 2008.

M. Birkinshaw. A deep survey of Abell 2218 at 408 and 1407 MHz - 5C 20. *Monthly Notices of the Royal Astronomical Society*, 222:731–751, October 1986.

M. Birkinshaw and S. F. Gull. Measurements of the gas contents of clusters of galaxies by observations of the background radiation at 10.7 GHz. III. *Monthly Notices of the Royal Astronomical Society*, 206:359–375, January 1984.

M. Birkinshaw, S. F. Gull, and K. J. E. Northover. Measurements of the gas contents of clusters of galaxies by observations of the background radiation at 10.6 GHz. *Monthly Notices of the Royal Astronomical Society*, 185:245–262, October 1978.

M. Birkinshaw, S. F. Gull, and K. J. E. Northover. Measurements of the gas contents of clusters of galaxies by observations of the background radiation at 10.6 GHz. II. *Monthly Notices of the Royal Astronomical Society*, 197:571–592, November 1981.

R. Blandford and D. Eichler. Particle acceleration at astrophysical shocks: A theory of cosmic ray origin. *Physics Reports*, 154:1–75, October 1987.

E. L. Blanton, S. W. Randall, T. E. Clarke, C. L. Sarazin, B. R. McNamara, E. M. Douglass, and M. McDonald. A Very Deep Chandra Observation of A2052: Bubbles, Shocks, and Sloshing. *Astrophysical Journal*, 737:99, August 2011.

P. Blasi and S. Colafrancesco. Cosmic rays, radio halos and nonthermal X-ray emission in clusters of galaxies. *Astroparticle Physics*, 12:169–183, November 1999.

P. Blasi, S. Gabici, and G. Brunetti. Gamma Rays from Clusters of Galaxies. *International Journal of Modern Physics A*, 22:681–706, 2007.

H. Böhringer and N. Werner. X-ray spectroscopy of galaxy clusters: studying astrophysical processes in the largest celestial laboratories. *Astronomy and Astrophysics Reviews*, 18:127–196, February 2010.

A. Bonafede, G. Giovannini, L. Feretti, F. Govoni, and M. Murgia. Double relics in Abell 2345 and Abell 1240. Spectral index and polarization analysis. *Astronomy and Astrophysics*, 494:429–442, February 2009.

A. Bonafede, H. T. Intema, M. Brüggen, M. Girardi, M. Nonino, N. Kantharia, R. J. van Weeren, and H. J. A. Röttgering. Evidence for Particle Re-acceleration in the Radio Relic in the Galaxy Cluster PLCKG287.0+32.9. *Astrophysical Journal*, 785: 1, April 2014a.

A. Bonafede, H. T. Intema, M. Brüggen, H. R. Russell, G. Ogrean, K. Basu, M. Sommer, R. J. van Weeren, R. Cassano, A. C. Fabian, and H. J. A. Röttgering. A giant radio halo in the cool core cluster CL1821+643. *Monthly Notices of the Royal Astronomical Society*, 444:L44–L48, October 2014b.

W. Boschin, M. Girardi, R. Barrena, A. Biviano, L. Feretti, and M. Ramella. Internal dynamics of the radio-halo cluster A2219: A multi-wavelength analysis. *Astronomy and Astrophysics*, 416:839–851, March 2004.

W. Boschin, M. Girardi, R. Barrena, and M. Nonino. Abell 1758N from an optical point of view: new insights on a merging cluster with diffuse radio emission. *Astronomy and Astrophysics*, 540:A43, April 2012.

A. Botteon, F. Gastaldello, G. Brunetti, and D. Dallacasa. A shock at the radio relic position in Abell 115. *Monthly Notices of the Royal Astronomical Society*, 460: L84–L88, July 2016a.

A. Botteon, F. Gastaldello, G. Brunetti, and D. Dallacasa. A shock at the radio relic position in Abell 115. *ArXiv e-prints*, April 2016b.

M. Brienza, E. Mahony, R. Morganti, I. Prandoni, and L. Godfrey. Dying radio galaxies in the LOFAR Lockman Hole. *ArXiv e-prints*, March 2016.

D. S. Briggs. High Fidelity Interferometric Imaging: Robust Weighting and NNLS Deconvolution. In *American Astronomical Society Meeting Abstracts*, volume 27 of *Bulletin of the American Astronomical Society*, page 1444, December 1995.

S. Brown, J. Duesterhoeft, and L. Rudnick. Multiple Shock Structures in a Radio-selected Cluster of Galaxies. *Astrophysical Journal Letters*, 727:L25, January 2011a.

S. Brown, A. Emerick, L. Rudnick, and G. Brunetti. Probing the Off-state of Cluster Giant Radio Halos. *Astrophysical Journal Letters*, 740:L28, October 2011b.

M. Brüggen, A. Bykov, D. Ryu, and H. Röttgering. Magnetic Fields, Relativistic Particles, and Shock Waves in Cluster Outskirts. *Space Science Reviews*, 166:187–213, May 2012.

G. Brunetti. Particle Acceleration and Non-Thermal Emission from Galaxy Clusters. *Journal of Korean Astronomical Society*, 37:493–500, December 2004.

G. Brunetti. Constraining relativistic protons and magnetic fields in galaxy clusters through radio and γ-ray observations: the case of A2256. *Astronomy and Astrophysics*, 508:599–602, December 2009.

G. Brunetti and T. W. Jones. Cosmic Rays in Galaxy Clusters and Their Nonthermal Emission. *International Journal of Modern Physics D*, 23:1430007, March 2014.

G. Brunetti and A. Lazarian. Particle reacceleration by compressible turbulence in galaxy clusters: effects of a reduced mean free path. *Monthly Notices of the Royal Astronomical Society*, 412:817–824, April 2011.

G. Brunetti, G. Setti, L. Feretti, and G. Giovannini. Particle reacceleration in the Coma cluster: radio properties and hard X-ray emission. *Monthly Notices of the Royal Astronomical Society*, 320:365–378, January 2001.

G. Brunetti, P. Blasi, O. Reimer, L. Rudnick, A. Bonafede, and S. Brown. Probing the origin of giant radio haloes through radio and γ-ray data: the case of the Coma cluster. *Monthly Notices of the Royal Astronomical Society*, 426:956–968, October 2012.

S. Buitink, A. Corstanje, H. Falcke, J. R. Hörandel, T. Huege, et al. A large light-mass component of cosmic rays at 10^{17}-$10^{17.5}$ electronvolts from radio observations. *Nature*, 531:70–73, March 2016.

V. Calvi, M. Stiavelli, L. Bradley, A. Pizzella, and S. Kim. The Effect of Surface Brightness Dimming in the Selection of High-z Galaxies. *Astrophysical Journal*, 796:102, December 2014.

R. E. A. Canning, S. W. Allen, D. E. Applegate, P. L. Kelly, A. von der Linden, A. Mantz, E. Million, R. G. Morris, and H. R. Russell. A series of shocks and edges in Abell 2219. *ArXiv e-prints*, May 2015.

C. L. Carilli and G. B. Taylor. Cluster Magnetic Fields. *Annual Review of Astronomy and Astrophysics*, 40:319–348, 2002.

R. Cassano. The radio-X-ray luminosity correlation of radio halos at low radio frequency. Application of the turbulent re-acceleration model. *Astronomy and Astrophysics*, 517:A10, July 2010.

R. Cassano and G. Brunetti. Cluster Mergers and Non-Thermal Phenomena: A Statistical Magneto-Turbulent Model. *Journal of Korean Astronomical Society*, 37: 583–587, December 2004.

R. Cassano and G. Brunetti. Cluster mergers and non-thermal phenomena: a statistical magneto-turbulent model. *Monthly Notices of the Royal Astronomical Society*, 357:1313–1329, March 2005.

R. Cassano, S. Ettori, S. Giacintucci, G. Brunetti, M. Markevitch, T. Venturi, and M. Gitti. On the Connection Between Giant Radio Halos and Cluster Mergers. *Astrophysical Journal Letters*, 721:L82–L85, October 2010.

R. Cassano, S. Ettori, G. Brunetti, S. Giacintucci, G. W. Pratt, T. Venturi, R. Kale, K. Dolag, and M. Markevitch. Revisiting Scaling Relations for Giant Radio Halos in Galaxy Clusters. *Astrophysical Journal*, 777:141, November 2013.

E. Churazov, W. Forman, C. Jones, and H. Böhringer. XMM-Newton Observations of the Perseus Cluster. I. The Temperature and Surface Brightness Structure. *Astrophysical Journal*, 590:225–237, June 2003.

B. G. Clark. An efficient implementation of the algorithm 'CLEAN'. *Astronomy and Astrophysics*, 89:377, September 1980.

T. E. Clarke and T. A. Ensslin. Deep 1.4 GHz Very Large Array Observations of the Radio Halo and Relic in Abell 2256. *Astronomical Journal*, 131:2900–2912, June 2006.

T. E. Clarke, E. L. Blanton, and C. L. Sarazin. The Complex Cooling Core of A2029: Radio and X-Ray Interactions. *Astrophysical Journal*, 616:178–191, November 2004.

A. S. Cohen, W. M. Lane, W. D. Cotton, N. E. Kassim, T. J. W. Lazio, R. A. Perley, J. J. Condon, and W. C. Erickson. The VLA Low-Frequency Sky Survey. *Astronomical Journal*, 134:1245–1262, September 2007.

S. Colafrancesco and P. Blasi. Clusters of galaxies and the diffuse gamma-ray background. *Astroparticle Physics*, 9:227–246, October 1998.

J. J. Condon, W. D. Cotton, E. W. Greisen, Q. F. Yin, R. A. Perley, G. B. Taylor, and J. J. Broderick. The NRAO VLA Sky Survey. *Astronomical Journal*, 115: 1693–1716, May 1998.

T. J. Cornwell, K. Golap, and S. Bhatnagar. The Noncoplanar Baselines Effect in Radio Interferometry: The W-Projection Algorithm. *IEEE Journal of Selected Topics in Signal Processing*, 2:647–657, November 2008.

D. Dallacasa, G. Brunetti, S. Giacintucci, R. Cassano, T. Venturi, G. Macario, N. E. Kassim, W. Lane, and G. Setti. Deep 1.4 GHz Follow-up of the Steep Spectrum Radio Halo in A521. *Astrophysical Journal*, 699:1288–1292, July 2009.

L. P. David and J. Kempner. Chandra and XMM-Newton Observations of the Double Cluster A1758. *Astrophysical Journal*, 613:831–840, October 2004.

G. de Bruyn, G. Miley, R. Rengelink, Y. Tang, M. Bremer, H. Rottgering, R. Raimond, M. Bremer, and D. Fullagar. The Westerbork Northern Sky Survey (Leiden, 1998). *VizieR Online Data Catalog*, 8062:0, February 2000.

S. De Grandi and S. Molendi. Metallicity Gradients in X-Ray Clusters of Galaxies. *Astrophysical Journal*, 551:153–159, April 2001.

H. R. de Ruiter, P. Parma, C. Fanti, and R. Fanti. VLA observations of low luminosity radio galaxies. II - Sources with angular size larger than two arcminutes. III - The A-array observations. *Astronomy and Astrophysics Supplement Series*, 65:111–188, July 1986.

B. Dennison. Formation of radio halos in clusters of galaxies from cosmic-ray protons. *Astrophysical Journal Letters*, 239:L93–L96, August 1980.

K. Dolag and T. A. Enßlin. Radio halos of galaxy clusters from hadronic secondary electron injection in realistic magnetic field configurations. *Astronomy and Astrophysics*, 362:151–157, October 2000.

J. Donnert, K. Dolag, G. Brunetti, and R. Cassano. Rise and fall of radio haloes in simulated merging galaxy clusters. *Monthly Notices of the Royal Astronomical Society*, 429:3564–3569, March 2013.

A. Drabent, M. Hoeft, R. F. Pizzo, A. Bonafede, R. J. van Weeren, and U. Klein. Diffuse radio emission in the complex merging galaxy cluster Abell 2069. *Astronomy and Astrophysics*, 575:A8, March 2015.

F. Durret, T. F. Laganá, and M. Haider. The merging cluster Abell 1758 revisited: multi-wavelength observations and numerical simulations. *Astronomy and Astrophysics*, 529:A38, May 2011.

H. Ebeling, A. C. Edge, H. Bohringer, S. W. Allen, C. S. Crawford, A. C. Fabian, W. Voges, and J. P. Huchra. The ROSAT Brightest Cluster Sample - I. The compilation of the sample and the cluster log N-log S distribution. *Monthly Notices of the Royal Astronomical Society*, 301:881–914, December 1998.

M. Einasto, E. Tago, J. Jaaniste, J. Einasto, and H. Andernach. The supercluster-void network I. The supercluster catalogue and large-scale distribution. *Astronomy and Astrophysics Supplement Series*, 123:119–133, May 1997.

T. Enßlin, C. Pfrommer, F. Miniati, and K. Subramanian. Cosmic ray transport in galaxy clusters: implications for radio halos, gamma-ray signatures, and cool core heating. *Astronomy and Astrophysics*, 527:A99, March 2011.

T. A. Enßlin, P. L. Biermann, P. P. Kronberg, and X.-P. Wu. Cosmic-Ray Protons and Magnetic Fields in Clusters of Galaxies and Their Cosmological Consequences. *Astrophysical Journal*, 477:560–567, March 1997.

T. A. Enßlin, P. L. Biermann, U. Klein, and S. Kohle. Shock Waves of the Large-Scale Structure Formation in the Universe. *ArXiv Astrophysics e-prints*, May 1998.

S. M. Faber and A. Dressler. Radial velocities for galaxies in 11 clusters. *Astronomical Journal*, 82:187–192, March 1977.

A. C. Fabian. Cooling Flows in Clusters of Galaxies. *Annual Review of Astronomy and Astrophysics*, 32:277–318, 1994.

H. D. Falcke, M. P. van Haarlem, A. G. de Bruyn, R. Braun, H. J. A. Röttgering, B. Stappers, W. H. W. M. Boland, H. R. Butcher, E. J. de Geus, L. V. Koopmans, R. P. Fender, H. J. M. E. Kuijpers, G. K. Miley, R. T. Schilizzi, C. Vogt, R. A. M. J. Wijers, M. W. Wise, W. N. Brouw, J. P. Hamaker, J. E. Noordam, T. Oosterloo, L. Bähren, M. A. Brentjens, S. J. Wijnholds, J. D. Bregman, W. A. van Cappellen, A. W. Gunst, G. W. (. Kant, J. Reitsma, K. van der Schaaf, and C. M. de Vos. A very brief description of LOFAR the Low Frequency Array. *Highlights of Astronomy*, 14:386–387, August 2007.

B. L. Fanaroff and J. M. Riley. The morphology of extragalactic radio sources of high and low luminosity. *Monthly Notices of the Royal Astronomical Society*, 167: 31P–36P, May 1974.

C. Fanti, R. Fanti, H. R. de Ruiter, and P. Parma. VLA observations of low luminosity radio galaxies. IV - The B2 sample revisited. *Astronomy and Astrophysics Supplement Series*, 69:57–76, April 1987.

D. Farnsworth, L. Rudnick, S. Brown, and G. Brunetti. Discovery of Megaparsec-scale, Low Surface Brightness Nonthermal Emission in Merging Galaxy Clusters Using the Green Bank Telescope. *Astrophysical Journal*, 779:189, December 2013.

L. Feretti and G. Giovannini. Diffuse Cluster Radio Sources (Review). In R. D. Ekers, C. Fanti, and L. Padrielli, editors, *Extragalactic Radio Sources*, volume 175 of *IAU Symposium*, page 333, 1996.

L. Feretti and G. Giovannini. Clusters of Galaxies in the Radio: Relativistic Plasma and ICM/Radio Galaxy Interaction Processes. In M. Plionis, O. López-Cruz, and D. Hughes, editors, *A Pan-Chromatic View of Clusters of Galaxies and the Large-Scale Structure*, volume 740 of *Lecture Notes in Physics, Berlin Springer Verlag*, page 24, 2008.

L. Feretti, I. M. Gioia, G. Giovannini, L. Gregorini, and L. Padrielli. High resolution radio and X-ray observations of A115. *Astronomy and Astrophysics*, 139:50–54, October 1984.

L. Feretti, H. Boehringer, G. Giovannini, and D. Neumann. The radio and X-ray properties of Abell 2255. *Astronomy and Astrophysics*, 317:432–440, January 1997a.

L. Feretti, G. Giovannini, and H. Böhringer. The radio and X-ray properties of Abell 2319. *New Astronomy*, 2:501–515, December 1997b.

L. Feretti, R. Fusco-Femiano, G. Giovannini, and F. Govoni. The giant radio halo in Abell 2163. *Astronomy and Astrophysics*, 373:106–112, July 2001.

L. Feretti, G. Brunetti, G. Giovannini, N. Kassim, E. Orrú, and G. Setti. Properties and Spectral Behaviour of Cluster Radio Halos. *Journal of Korean Astronomical Society*, 37:315–322, December 2004a.

L. Feretti, E. Orrù, G. Brunetti, G. Giovannini, N. Kassim, and G. Setti. Spectral index maps of the radio halos in Abell 665 and Abell 2163. *Astronomy and Astrophysics*, 423:111–119, August 2004b.

L. Feretti, G. Giovannini, F. Govoni, and M. Murgia. Clusters of galaxies: observational properties of the diffuse radio emission. *Astronomy and Astrophysics Reviews*, 20:54, May 2012.

E. Fermi. On the Origin of the Cosmic Radiation. *Physical Review*, 75:1169–1174, April 1949.

A. Finoguenov, C. L. Sarazin, K. Nakazawa, D. R. Wik, and T. E. Clarke. XMM-Newton Observation of the Northwest Radio Relic Region in A3667. *Astrophysical Journal*, 715:1143–1151, June 2010.

W. Forman, J. Bechtold, W. Blair, R. Giacconi, L. van Speybroeck, and C. Jones. Einstein imaging observations of clusters with a bimodal mass distribution. *Astrophysical Journal Letters*, 243:L133–L136, February 1981.

W. Forman, C. Jones, M. Markevitch, A. Vikhlinin, and E. Churazov. High Angular Resolution Cluster Observations with Chandra: A New View. In L. Feretti, I. M. Gioia, and G. Giovannini, editors, *Merging Processes in Galaxy Clusters*, volume 272 of *Astrophysics and Space Science Library*, pages 109–132, June 2002.

W. R. Forman, E. Churazov, S. Heinz, S. Giacintucci, C. Jones, A. Bogdan, L. P David, R. P. Kraft, M. Murgia, M. L. Markevitch, S. W. Randall, R. J. Van Weeren, and A. Vikhlinin. 3C28 in Abell 115- A Radio Source With a Twist: Tracing Gas Vortices in a Merging Subcluster Core. In *American Astronomical Society Meeting Abstracts #224*, volume 224 of *American Astronomical Society Meeting Abstracts*, page 222.03, June 2014.

Y. Fujita, M. Takizawa, and C. L. Sarazin. Nonthermal Emissions from Particles Accelerated by Turbulence in Clusters of Galaxies. *Astrophysical Journal*, 584:190–202, February 2003.

Y. Fujita, T. Matsumoto, and K. Wada. Strong Turbulence in the Cool Cores of Galaxy Clusters: Can Tsunamis Solve the Cooling Flow Problem? *Astrophysical Journal Letters*, 612:L9–L12, September 2004.

Y. Fujita, K. Kohri, R. Yamazaki, and M. Kino. Nonthermal Emission Associated with Strong AGN Outbursts at the Centers of Galaxy Clusters. *Astrophysical Journal Letters*, 663:L61–L64, July 2007.

S. Gabici and P. Blasi. Nonthermal Radiation from Clusters of Galaxies: The Role of Merger Shocks in Particle Acceleration. *Astrophysical Journal*, 583:695–705, February 2003.

S. Giacintucci. Diffuse radio sources in colliding galaxy clusters . Low frequency follow up of the GMRT Radio Halo Survey. *Memorie della Societa Astronomica Italiana*, 82:541, 2011.

S. Giacintucci, T. Venturi, G. Macario, D. Dallacasa, G. Brunetti, M. Markevitch, R. Cassano, S. Bardelli, and R. Athreya. Shock acceleration as origin of the radio relic in A 521? *Astronomy and Astrophysics*, 486:347–358, August 2008.

S. Giacintucci, M. Markevitch, T. Venturi, T. E. Clarke, R. Cassano, and P. Mazzotta. New Detections of Radio Minihalos in Cool Cores of Galaxy Clusters. *Astrophysical Journal*, 781:9, January 2014.

V. L. Ginzburg and S. I. Syrovatskii. *The origin of cosmic rays.* 1969.

I. M. Gioia, T. Maccacaro, M. J. Geller, J. P. Huchra, J. Stocke, and J. E. Steiner. Abell 2069 - an X-ray cluster of galaxies with multiple subcondensations. *Astrophysical Journal Letters*, 255:L17–L21, April 1982.

G. Giovannini and L. Feretti. Halo and relic sources in clusters of galaxies. *New Astronomy*, 5:335–347, September 2000.

G. Giovannini, L. Feretti, and L. Gregorini. Radio observations of the first ranked galaxies in A98, A115, A160, A278 and A568. *Astronomy and Astrophysics Supplement Series*, 69:171–182, May 1987.

G. Giovannini, L. Feretti, T. Venturi, K.-T. Kim, and P. P. Kronberg. The halo radio source Coma C and the origin of halo sources. *Astrophysical Journal*, 406:399–406, April 1993.

G. Giovannini, M. Tordi, and L. Feretti. Radio halo and relic candidates from the NRAO VLA Sky Survey. *New Astronomy*, 4:141–155, March 1999.

G. Giovannini, L. Feretti, F. Govoni, M. Murgia, and R. Pizzo. New radio halos and relics in clusters of galaxies. *Astronomische Nachrichten*, 327:563, June 2006.

G. Giovannini, A. Bonafede, L. Feretti, F. Govoni, M. Murgia, F. Ferrari, and G. Monti. Radio halos in nearby ($z < 0.4$) clusters of galaxies. *Astronomy and Astrophysics*, 507:1257–1270, December 2009.

G. Giovannini, L. Feretti, M. Girardi, F. Govoni, M. Murgia, V. Vacca, and J. Bagchi. A giant radio halo in the low luminosity X-ray cluster Abell 523. *Astronomy and Astrophysics*, 530:L5, June 2011.

M. Girardi, S. Bardelli, R. Barrena, W. Boschin, F. Gastaldello, and M. Nonino. Internal dynamics of Abell 2254: a merging galaxy cluster with a clumpy, diffuse radio emission. *Astronomy and Astrophysics*, 536:A89, December 2011.

M. Gitti, G. Brunetti, and G. Setti. Modeling the interaction between ICM and relativistic plasma in cooling flows: The case of the Perseus cluster. *Astronomy and Astrophysics*, 386:456–463, May 2002.

M. Gitti, G. Brunetti, L. Feretti, and G. Setti. Particle acceleration in cooling flow clusters of galaxies: The case of Abell 2626. *Astronomy and Astrophysics*, 417:1–11, April 2004.

F. Govoni and L. Feretti. Magnetic Fields in Clusters of Galaxies. *International Journal of Modern Physics D*, 13:1549–1594, 2004.

F. Govoni, T. A. Enßlin, L. Feretti, and G. Giovannini. A comparison of radio and X-ray morphologies of four clusters of galaxies containing radio halos. *Astronomy and Astrophysics*, 369:441–449, April 2001a.

F. Govoni, L. Feretti, G. Giovannini, H. Böhringer, T. H. Reiprich, and M. Murgia. Radio and X-ray diffuse emission in six clusters of galaxies. *Astronomy and Astrophysics*, 376:803–819, September 2001b.

F. Govoni, M. Markevitch, A. Vikhlinin, L. van Speybroeck, L. Feretti, and G. Giovannini. Chandra Temperature Maps for Galaxy Clusters with Radio Halos. *Astrophysical Journal*, 605:695–708, April 2004.

F. Govoni, M. Murgia, L. Feretti, G. Giovannini, D. Dallacasa, and G. B. Taylor. A2255: The first detection of filamentary polarized emission in a radio halo. *Astronomy and Astrophysics*, 430:L5–L8, January 2005.

F. Govoni, M. Murgia, M. Markevitch, L. Feretti, G. Giovannini, G. B. Taylor, and E. Carretti. A search for diffuse radio emission in the relaxed, cool-core galaxy clusters A1068, A1413, A1650, A1835, A2029, and Ophiuchus. *Astronomy and Astrophysics*, 499:371–383, May 2009.

L. Gregorini and M. Bondi. High resolution observations of the narrow angle tail radio galaxy in Abell 115. *Astronomy and Astrophysics*, 225:333–340, November 1989.

K. Gutierrez and H. Krawczynski. The Off-Axis Galaxy Cluster Merger A115. *Astrophysical Journal*, 619:161–168, January 2005.

S. E. G. Hales, J. M. Riley, E. M. Waldram, P. J. Warner, and J. E. Baldwin. A final non-redundant catalogue for the 7C 151-MHz survey. *Monthly Notices of the Royal Astronomical Society*, 382:1639–1642, December 2007.

D. E. Harris and G. K. Miley. Westerbork observations of five fields centered on Abell clusters of galaxies. *Astronomy and Astrophysics Supplement Series*, 34:117–128, October 1978.

J. J. Harwood, M. J. Hardcastle, and J. H. Croston. Spectral ageing in the lobes of cluster-centre FR II radio galaxies. *Monthly Notices of the Royal Astronomical Society*, 454:3403–3422, December 2015.

S. Heinz, M. Brüggen, A. Young, and E. Levesque. The answer is blowing in the wind: simulating the interaction of jets with dynamic cluster atmospheres. *Monthly Notices of the Royal Astronomical Society*, 373:L65–L69, November 2006.

M. Hoeft, M. Brüggen, G. Yepes, S. Gottlöber, and A. Schwope. Diffuse radio emission from clusters in the MareNostrum Universe simulation. *Monthly Notices of the Royal Astronomical Society*, 391:1511–1526, December 2008.

J. A. Högbom. Aperture Synthesis with a Non-Regular Distribution of Interferometer Baselines. *Astronomy and Astrophysics Supplement Series*, 15:417, June 1974.

T. Hogge, C. L. Sarazin, and D. R. Wik. The Merger Dynamics of the Abell 2061 Cluster and the Origin of the Radio Relics and Halos. In *American Astronomical Society Meeting Abstracts #221*, volume 221 of *American Astronomical Society Meeting Abstracts*, page 243.04, January 2013.

H. Honda, M. Hirayama, H. Ezawa, K. Kikuchi, T. Ohashi, M. Watanabe, H. Kunieda, and K. Yamashita. Temperature Structure in Merging Coma Cluster of Galaxies. In K. Koyama, S. Kitamoto, and M. Itoh, editors, *The Hot Universe*, volume 188 of *IAU Symposium*, page 308, 1998.

H. T. Intema. SPAM: A data reduction recipe for high-resolution, low-frequency radio-interferometric observations. *ArXiv e-prints*, February 2014.

H. T. Intema, S. van der Tol, W. D. Cotton, A. S. Cohen, I. M. van Bemmel, and H. J. A. Röttgering. Ionospheric calibration of low frequency radio interferometric observations using the peeling scheme. I. Method description and first results. *Astronomy and Astrophysics*, 501:1185–1205, July 2009.

M. Jõeveer, J. Einasto, and M. Tago. The cell structure of the Universe. *Tartu Astrofüüs. Obs. Preprint, Nr. A-1, 45 p.*, 1, July 1977.

M. Jones, R. Saunders, P. Alexander, M. Birkinshaw, N. Dilon, K. Grainge, S. Hancock, A. Lasenby, D. Lefebvre, and G. Pooley. An image of the Sunyaev-Zel'dovich effect. *Nature*, 365:320–323, September 1993.

R. Kale, T. Venturi, S. Giacintucci, D. Dallacasa, R. Cassano, G. Brunetti, G. Macario, and R. Athreya. The Extended GMRT Radio Halo Survey. I. New upper limits on radio halos and mini-halos. *Astronomy and Astrophysics*, 557:A99, September 2013.

H. Kang and D. Ryu. Diffusive Shock Acceleration at Cosmological Shock Waves. *Astrophysical Journal*, 764:95, February 2013.

J. C. Kempner and C. L. Sarazin. Radio Halo and Relic Candidates from the Westerbork Northern Sky Survey. *Astrophysical Journal*, 548:639–651, February 2001.

K.-T. Kim, P. P. Kronberg, G. Giovannini, and T. Venturi. Discovery of intergalactic radio emission in the Coma-A1367 supercluster. *Nature*, 341:720–723, October 1989.

K. Knowles, H. T. Intema, A. J. Baker, V. Bharadwaj, J. R. Bond, C. Cress, N. Gupta, A. Hajian, M. Hilton, A. D. Hincks, R. Hlozek, J. P. Hughes, R. R. Lindner, T. A. Marriage, F. Menanteau, K. Moodley, M. D. Niemack, E. D. Reese, J. Sievers, C. Sifón, R. Srianand, and E. J. Wollack. A giant radio halo in a low-mass SZ-selected galaxy cluster: ACT-CL J0256.5+0006. *Monthly Notices of the Royal Astronomical Society*, 459:4240–4258, July 2016.

A. V. Kravtsov and S. Borgani. Formation of Galaxy Clusters. *Annual Review of Astronomy and Astrophysics*, 50:353–409, September 2012.

P.-H. Kuo, C.-Y. Hwang, and W.-H. Ip. The Evolution of Diffuse Radio Sources in Galaxy Clusters. *Astrophysical Journal*, 604:108–115, March 2004.

J. F. Le Borgne and R. Vilchez-Gomez. An Optical Identification of Radio Sources in the Field of the Cluster of Galaxies ABELL:2218. *Astronomy and Astrophysics*, 271:425, April 1993.

C. J. Lonsdale. Configuration Considerations for Low Frequency Arrays. In N. Kassim, M. Perez, W. Junor, and P. Henning, editors, *From Clark Lake to the Long Wavelength Array: Bill Erickson's Radio Science*, volume 345 of *Astronomical Society of the Pacific Conference Series*, page 399, December 2005.

M. E. Machacek, M. W. Bautz, C. Canizares, and G. P. Garmire. Chandra Observations of Galaxy Cluster A2218. *Astrophysical Journal*, 567:188–201, March 2002.

J. M. Malarecki, L. Staveley-Smith, L. Saripalli, R. Subrahmanyan, D. H. Jones, A. R. Duffy, and M. Rioja. Giant radio galaxies - I. Intergalactic barometers. *Monthly Notices of the Royal Astronomical Society*, 432:200–224, June 2013.

A. W. Mann and H. Ebeling. X-ray-optical classification of cluster mergers and the evolution of the cluster merger fraction. *Monthly Notices of the Royal Astronomical Society*, 420:2120–2138, March 2012.

F. Marini, S. Bardelli, E. Zucca, S. De Grandi, A. Cappi, S. Ettori, L. Moscardini, G. Tormen, and A. Diaferio. BeppoSAX temperature maps of galaxy clusters in the Corona Borealis supercluster: A2061, A2067 and A2124. *Monthly Notices of the Royal Astronomical Society*, 353:1219–1230, October 2004.

M. Markevitch. Temperature Structure of Four Hot Clusters Obtained with ASCA Data. *Astrophysical Journal Letters*, 465:L1, July 1996.

M. Markevitch and A. Vikhlinin. Shocks and cold fronts in galaxy clusters. *Physics Reports*, 443:1–53, May 2007.

M. Markevitch, T. J. Ponman, P. E. J. Nulsen, M. W. Bautz, D. J. Burke, L. P. David, D. Davis, R. H. Donnelly, W. R. Forman, C. Jones, J. Kaastra, E. Kellogg, D.-W. Kim, J. Kolodziejczak, P. Mazzotta, A. Pagliaro, S. Patel, L. Van Speybroeck, A. Vikhlinin, J. Vrtilek, M. Wise, and P. Zhao. Chandra Observation of Abell 2142: Survival of Dense Subcluster Cores in a Merger. *Astrophysical Journal*, 541: 542–549, October 2000.

M. Markevitch, A. H. Gonzalez, L. David, A. Vikhlinin, S. Murray, W. Forman, C. Jones, and W. Tucker. A Textbook Example of a Bow Shock in the Merging Galaxy Cluster 1E 0657-56. *Astrophysical Journal Letters*, 567:L27–L31, March 2002.

P. Mazzotta and S. Giacintucci. Do Radio Core-Halos and Cold Fronts in Non-Major-Merging Clusters Originate from the Same Gas Sloshing? *Astrophysical Journal Letters*, 675:L9–L12, March 2008.

G. K. Miley, G. C. Perola, P. C. van der Kruit, and H. van der Laan. Active Galaxies with Radio Trails in Clusters. *Nature*, 237:269–272, June 1972.

E. T. Million and S. W. Allen. Chandra measurements of non-thermal-like X-ray emission from massive, merging, radio halo clusters. *Monthly Notices of the Royal Astronomical Society*, 399:1307–1327, November 2009.

F. Miniati, T. W. Jones, H. Kang, and D. Ryu. Cosmic-Ray Electrons in Groups and Clusters of Galaxies: Primary and Secondary Populations from a Numerical Cosmological Simulation. *Astrophysical Journal*, 562:233–253, November 2001.

A. T. Moffet and M. Birkinshaw. A VLA survey of the three clusters of galaxies 0016 + 16, Abell 665, and Abell 2218. *Astronomical Journal*, 98:1148–1174, October 1989.

I. Mohammed, J. Liesenborgs, P. Saha, and L. L. R. Williams. Mass-galaxy offsets in Abell 3827, 2218 and 1689: intrinsic properties or line-of-sight substructures? *Monthly Notices of the Royal Astronomical Society*, 439:2651–2661, April 2014.

N. Mohan and D. Rafferty. PyBDSM: Python Blob Detection and Source Measurement. Astrophysics Source Code Library, February 2015.

S. Molendi, S. De Grandi, R. Fusco-Femiano, S. Colafrancesco, F. Fiore, R. Nesci, and F. Tamburelli. The BEPPOSAX View of the Hot Cluster Abell 2319. *Astrophysical Journal Letters*, 525:L73–L76, November 1999.

D. E. Morosan, P. T. Gallagher, P. Zucca, R. Fallows, E. P. Carley, et al. LOFAR tied-array imaging of Type III solar radio bursts. *Astronomy and Astrophysics*, 568: A67, August 2014.

M. Murgia, F. Govoni, M. Markevitch, L. Feretti, G. Giovannini, G. B. Taylor, and E. Carretti. Comparative analysis of the diffuse radio emission in the galaxy clusters A1835, A2029, and Ophiuchus. *Astronomy and Astrophysics*, 499:679–695, June 2009.

M. Murgia, P. Parma, K.-H. Mack, H. R. de Ruiter, R. Fanti, F. Govoni, A. Tarchi, S. Giacintucci, and M. Markevitch. Dying radio galaxies in clusters. *Astronomy and Astrophysics*, 526:A148, February 2011.

J. E. Noordam. LOFAR calibration challenges. In J. M. Oschmann, Jr., editor, *Ground-based Telescopes*, volume 5489 of *Proceedings of the SPIE*, pages 817–825, October 2004.

C. P. O'Dea and F. N. Owen. VLA observations of 57 sources in clusters of galaxies. *Astronomical Journal*, 90:927–953, June 1985.

W. R. Oegerle, J. M. Hill, and M. J. Fitchett. Observations of High Dispersion Clusters of Galaxies: Constraints on Cold Dark Matter. *Astronomical Journal*, 110:32, July 1995.

A. R. Offringa. AOFlagger RFI Software, October 2010. Astrophysics Source Code Library.

G. A. Ogrean, M. Brüggen, H. Röttgering, A. Simionescu, J. H. Croston, R. van Weeren, and M. Hoeft. XMM-Newton observations of the merging galaxy cluster CIZA J2242.8+5301. *Monthly Notices of the Royal Astronomical Society*, 429:2617–2633, March 2013.

T. B. O'Hara, J. J. Mohr, and M. A. Guerrero. A Chandra Study of the Effects of a Major Merger on the Structure of A2319. *Astrophysical Journal*, 604:604–613, April 2004.

T. B. O'Hara, J. J. Mohr, J. J. Bialek, and A. E. Evrard. Effects of Mergers and Core Structure on the Bulk Properties of Nearby Galaxy Clusters. *Astrophysical Journal*, 639:64–80, March 2006.

A. Okabe, editor. *Spatial tessellations : concepts and applications of voronoi diagrams*, 2000.

E. Orrú, M. Murgia, L. Feretti, F. Govoni, G. Brunetti, G. Giovannini, M. Girardi, and G. Setti. Low-frequency study of two clusters of galaxies: A2744 and A2219. *Astronomy and Astrophysics*, 467:943–954, June 2007.

E. Orrù, M. Murgia, L. Feretti, F. Govoni, G. Giovannini, W. Lane, N. Kassim, and R. Paladino. Low-frequency study of two giant radio galaxies: 3C 35 and 3C 223. *Astronomy and Astrophysics*, 515:A50, June 2010.

J. P. Ostriker and M. A. Hausman. Cannibalism among the galaxies - Dynamically produced evolution of cluster luminosity functions. *Astrophysical Journal Letters*, 217:L125–L129, November 1977.

F. Owen, G. Morrison, and W. Voges. Radio Halos in Luminous RASS Clusters. In H. Boehringer, L. Feretti, and P. Schuecker, editors, *Diffuse Thermal and Relativistic Plasma in Galaxy Clusters*, page 9, 1999.

F. N. Owen, J. O. Burns, L. Rudnick, and E. W. Greisen. VLA observations of head-tail radio sources. *Astrophysical Journal Letters*, 229:L59–L63, April 1979.

F. N. Owen, R. A. White, and J. O. Burns. A 20 centimeter VLA survey of Abell clusters of galaxies. II - Images and optical identifications. *Astrophysical Journal Supplement*, 80:501–529, June 1992.

M. S. Owers, P. E. J. Nulsen, W. J. Couch, and M. Markevitch. A High Fidelity Sample of Cold Front Clusters from the Chandra Archive. *Astrophysical Journal*, 704:1349–1370, October 2009.

M. S. Owers, P. E. J. Nulsen, W. J. Couch, C.-J. Ma, L. P. David, W. R. Forman, A. M. Hopkins, C. Jones, and R. J. van Weeren. A Merger Shock in A2034. *Astrophysical Journal*, 780:163, January 2014.

P. Parma, C. Fanti, R. Fanti, R. Morganti, and H. R. de Ruiter. VLA observations of low-luminosity radio galaxies. VI - Discussion of radio jets. *Astronomy and Astrophysics*, 181:244–264, July 1987.

P. Parma, M. Murgia, H. R. de Ruiter, R. Fanti, K.-H. Mack, and F. Govoni. In search of dying radio sources in the local universe. *Astronomy and Astrophysics*, 470:875–888, August 2007.

R. B. Partridge, R. A. Perley, N. Mandolesi, and F. Delpino. Preliminary VLA limits on the Sunyaev-Zel'dovich effect in Abell 2218. *Astrophysical Journal*, 317:112–120, June 1987.

R. Pello, J. F. Le Borgne, B. Sanahuja, G. Mathez, and B. Fort. The system of arcs in the cluster of galaxies Abell 2218 - Photometry, spectroscopy and geometry. *Astronomy and Astrophysics*, 266:6–14, December 1992.

R. Pello-Descayre, B. Sanahuja, G. Soucail, G. Mathez, and E. Ojero. Detection and photometry of a complex system in the center of the A 2218 cluster of galaxies. *Astronomy and Astrophysics*, 190:L11–L14, January 1988.

S. C. Perrenod and C. J. Lada. The Sunyaev-Zeldovich effect at 9 millimeters. *Astrophysical Journal Letters*, 234:L173–L175, December 1979.

V. Petrosian. On the Nonthermal Emission and Acceleration of Electrons in Coma and Other Clusters of Galaxies. *Astrophysical Journal*, 557:560–572, August 2001.

V. Petrosian and W. E. East. Heating and Acceleration of Intracluster Medium Electrons by Turbulence. *Astrophysical Journal*, 682:175-185, July 2008.

C. Pfrommer and T. A. Enßlin. Constraining the population of cosmic ray protons in cooling flow clusters with γ-ray and radio observations: Are radio mini-halos of hadronic origin? *Astronomy and Astrophysics*, 413:17–36, January 2004.

R. Piffaretti, M. Arnaud, G. W. Pratt, E. Pointecouteau, and J.-B. Melin. The MCXC: a meta-catalogue of x-ray detected clusters of galaxies. *Astronomy and Astrophysics*, 534:A109, October 2011.

M. Pilia, J. W. T. Hessels, B. W. Stappers, V. I. Kondratiev, and M. others Kramer. Wide-band, low-frequency pulse profiles of 100 radio pulsars with LOFAR. *Astronomy and Astrophysics*, 586:A92, February 2016.

A. Pinzke, S. P. Oh, and C. Pfrommer. Giant radio relics in galaxy clusters: reacceleration of fossil relativistic electrons? *Monthly Notices of the Royal Astronomical Society*, 435:1061–1082, October 2013.

A. Pinzke, S. P. Oh, and C. Pfrommer. Turbulence and Particle Acceleration in Giant Radio Halos: the Origin of Seed Electrons. *ArXiv e-prints*, March 2015.

R. F. Pizzo and A. G. de Bruyn. Radio spectral study of the cluster of galaxies Abell 2255. *Astronomy and Astrophysics*, 507:639–659, November 2009.

Planck Collaboration, P. A. R. Ade, N. Aghanim, C. Armitage-Caplan, M. Arnaud, M. Ashdown, F. Atrio-Barandela, J. Aumont, H. Aussel, C. Baccigalupi, and et al. Planck 2013 results. XXXII. The updated Planck catalogue of Sunyaev-Zeldovich sources. *Astronomy and Astrophysics*, 581:A14, September 2015.

Planck Collaboration, P. A. R. Ade, N. Aghanim, M. Arnaud, M. Ashdown, J. Aumont, C. Baccigalupi, A. J. Banday, R. B. Barreiro, J. G. Bartlett, and et al. Planck 2015 results. XIII. Cosmological parameters. *Astronomy and Astrophysics*, 594:A13, September 2016.

G. B. Poole, M. A. Fardal, A. Babul, I. G. McCarthy, T. Quinn, and J. Wadsley. The impact of mergers on relaxed X-ray clusters - I. Dynamical evolution and emergent transient structures. *Monthly Notices of the Royal Astronomical Society*, 373:881–905, December 2006.

G. B. Poole, A. Babul, I. G. McCarthy, A. J. R. Sanderson, and M. A. Fardal. The impact of mergers on relaxed X-ray clusters - III. Effects on compact cool cores. *Monthly Notices of the Royal Astronomical Society*, 391:1163–1175, December 2008.

M. Postman, M. J. Geller, and J. P. Huchra. The dynamics of the Corona Borealis supercluster. *Astronomical Journal*, 95:267–283, February 1988.

K. Rines and A. Diaferio. CIRS: Cluster Infall Regions in the Sloan Digital Sky Survey. I. Infall Patterns and Mass Profiles. *Astronomical Journal*, 132:1275–1297, September 2006.

E. Rizza, J. O. Burns, M. J. Ledlow, F. N. Owen, W. Voges, and M. Bliton. X-ray observations of distant Abell clusters. *Monthly Notices of the Royal Astronomical Society*, 301:328–342, December 1998.

M. Rossetti, F. Gastaldello, and S. Molendi. Temperature and abundance maps of merging galaxy clusters. In J.-P. Paillé, editor, *35th COSPAR Scientific Assembly*, volume 35 of *COSPAR Meeting*, page 2794, 2004.

H. J. A. Rottgering, M. H. Wieringa, R. W. Hunstead, and R. D. Ekers. The extended radio emission in the luminous X-ray cluster A3667. *Monthly Notices of the Royal Astronomical Society*, 290:577–584, September 1997.

L. Rudnick and J. A. Lemmerman. An Objective Survey of Mpc-scale Radio Emission in $0.03 < z < 0.3$ Bright X-ray Clusters. *Astrophysical Journal*, 697:1341–1357, June 2009.

H. Russel. Two shock fronts in the merging cluster Abell 2146. In *Galaxy Clusters: Observations, Physics and Cosmology*, page 25, July 2010.

H. R. Russell, R. J. van Weeren, A. C. Edge, B. R. McNamara, J. S. Sanders, A. C. Fabian, S. A. Baum, R. E. A. Canning, M. Donahue, and C. P. O'Dea. A merger mystery: no extended radio emission in the merging cluster Abell 2146. *Monthly Notices of the Royal Astronomical Society*, 417:L1–L5, October 2011.

D. Ryu, H. Kang, J. Cho, and S. Das. Turbulence and Magnetic Fields in the Large-Scale Structure of the Universe. *Science*, 320:909, May 2008.

J. S. Sanders, A. C. Fabian, and G. B. Taylor. Giant cavities, cooling and metallicity substructure in Abell 2204. *Monthly Notices of the Royal Astronomical Society*, 393: 71–82, February 2009.

J. S. Santos, P. Rosati, P. Tozzi, H. Böhringer, S. Ettori, and A. Bignamini. Searching for cool core clusters at high redshift. *Astronomy and Astrophysics*, 483:35–47, May 2008.

C. L. Sarazin. The Energy Spectrum of Primary Cosmic-Ray Electrons in Clusters of Galaxies and Inverse Compton Emission. *Astrophysical Journal*, 520:529–547, August 1999.

C. L. Sarazin. The Physics of Cluster Mergers. In L. Feretti, I. M. Gioia, and G. Giovannini, editors, *Merging Processes in Galaxy Clusters*, volume 272 of *Astrophysics and Space Science Library*, pages 1–38, June 2002.

C. L. Sarazin. Gas Dynamics in Clusters of Galaxies. In M. Plionis, O. López-Cruz, and D. Hughes, editors, *A Pan-Chromatic View of Clusters of Galaxies and the Large-Scale Structure*, volume 740 of *Lecture Notes in Physics, Berlin Springer Verlag*, page 24, 2008.

C. L. Sarazin. *X-Ray Emission from Clusters of Galaxies.* June 2009.

A. M. M. Scaife and G. H. Heald. A broad-band flux scale for low-frequency radio telescopes. *Monthly Notices of the Royal Astronomical Society*, 423:L30–L34, June 2012.

D. Schallwich. *Mikrowellenhintergrundsabsorption in Galaxienhaufen. Beobachtung des Syunyayev-Zeldovich-Effekts in A 2218.* 1982.

D. Schallwich and R. Wielebinski. A complex radio source in the center of Abell 2218. *Astronomy and Astrophysics*, 71:L15, January 1979.

P. Schneider. *Extragalactic Astronomy and Cosmology: An Introduction.* 2015.

F. R. Schwab. Relaxing the isoplanatism assumption in self-calibration; applications to low-frequency radio interferometry. *Astronomical Journal*, 89:1076–1081, July 1984.

A. Shulevski, R. Morganti, P. D. Barthel, J. J. Harwood, G. Brunetti, R. J. van Weeren, H. J. A. Röttgering, G. J. White, C. Horellou, M. Kunert-Bajraszewska, M. Jamrozy, K. T. Chyzy, E. Mahony, G. Miley, M. Brienza, L. Bîrzan, D. A. Rafferty, M. Brüggen, M. W. Wise, J. Conway, F. de Gasperin, and N. Vilchez. AGN duty cycle estimates for the ultra-steep spectrum radio relic VLSS J1431.8+1331. *Astronomy and Astrophysics*, 583:A89, November 2015.

T. A. Small, W. L. W. Sargent, and D. Hamilton. The Norris Survey of the Corona Borealis Supercluster. II. Galaxy Evolution with Redshift and Environment. *Astrophysical Journal*, 487:512–528, October 1997a.

T. A. Small, W. L. W. Sargent, and D. Hamilton. The Norris Survey of the Corona Borealis Supercluster. I. Observations and Catalog Construction. *Astrophysical Journal Supplement*, 111:1–71, 1997b.

T. A. Small, C.-P. Ma, W. L. W. Sargent, and D. Hamilton. The Norris Survey of the Corona Borealis Supercluster. III. Structure and Mass of the Supercluster. *Astrophysical Journal*, 492:45–56, January 1998.

C. Sotomayor-Beltran, C. Sobey, J. W. T. Hessels, G. de Bruyn, A. Noutsos, et al. Calibrating high-precision Faraday rotation measurements for LOFAR and the next generation of low-frequency radio telescopes. *Astronomy and Astrophysics*, 552:A58, April 2013.

V. Springel, S. D. M. White, A. Jenkins, C. S. Frenk, N. Yoshida, L. Gao, J. Navarro, R. Thacker, D. Croton, J. Helly, J. A. Peacock, S. Cole, P. Thomas, H. Couchman, A. Evrard, J. Colberg, and F. Pearce. Simulations of the formation, evolution and clustering of galaxies and quasars. *Nature*, 435:629–636, June 2005.

A. J. Stewart, R. P. Fender, J. W. Broderick, T. E. Hassall, T. Muñoz-Darias, et al. LOFAR MSSS: detection of a low-frequency radio transient in 400 h of monitoring of the North Celestial Pole. *Monthly Notices of the Royal Astronomical Society*, 456:2321–2342, March 2016.

E. Storm, T. E. Jeltema, and L. Rudnick. A radio and X-ray study of the merging cluster A2319. *Monthly Notices of the Royal Astronomical Society*, 448:2495–2503, April 2015.

M. F. Struble and H. J. Rood. A Compilation of Redshifts and Velocity Dispersions for ACO Clusters. *Astrophysical Journal Supplement*, 125:35–71, November 1999.

C. Sugawara, M. Takizawa, and K. Nakazawa. Suzaku Observation of the Radio Halo Cluster Abell 2319: Gas Dynamics and Hard X-Ray Properties. *Publications of the Astronomical Society of Japan*, 61:1293–, December 2009.

C. Tasse, S. van der Tol, J. van Zwieten, G. van Diepen, and S. Bhatnagar. Applying full polarization A-Projection to very wide field of view instruments: An imager for LOFAR. *Astronomy and Astrophysics*, 553:A105, May 2013.

G. B. Taylor, C. L. Carilli, and R. A. Perley, editors. *Synthesis Imaging in Radio Astronomy II*, volume 180 of *Astronomical Society of the Pacific Conference Series*, 1999.

M. Tsuboi, A. Miyazaki, T. Kasuga, H. Matsuo, and N. Kuno. Measurement of the Sunyaev-Zel'dovich Effect toward Abell 2218 at 36GHz. *Publications of the Astronomical Society of Japan*, 50:169–173, February 1998.

B. Uyaniker, W. Reich, R. Schlickeiser, and R. Wielebinski. Sunyaev-Zeldovich effect measured towards Abell cluster A 2218. *Astronomy and Astrophysics*, 325:516–522, September 1997.

V. Vacca, F. Govoni, M. Murgia, G. Giovannini, L. Feretti, M. Tugnoli, M. A. Verheijen, and G. B. Taylor. Discovery of diffuse radio emission in the galaxy cluster A1689. *Astronomy and Astrophysics*, 535:A82, November 2011.

S. . van der Tol, B. D. Jeffs, and A.-J. . van der Veen. Self-Calibration for the LOFAR Radio Astronomical Array. *IEEE Transactions on Signal Processing*, 55:4497–4510, September 2007.

M. P. van Haarlem, M. W. Wise, A. W. Gunst, G. Heald, J. P. McKean, et al. LOFAR: The LOw-Frequency ARray. *Astronomy and Astrophysics*, 556:A2, August 2013.

R. J. van Weeren, H. J. A. Röttgering, M. Brüggen, and M. Hoeft. Particle Acceleration on Megaparsec Scales in a Merging Galaxy Cluster. *Science*, 330: 347, October 2010.

R. J. van Weeren, M. Brüggen, H. J. A. Röttgering, M. Hoeft, S. E. Nuza, and H. T. Intema. Radio continuum observations of new radio halos and relics from the NVSS and WENSS surveys. Relic orientations, cluster X-ray luminosity, and redshift distributions. *Astronomy and Astrophysics*, 533:A35, September 2011.

R. J. van Weeren, H. J. A. Röttgering, H. T. Intema, L. Rudnick, M. Brüggen, M. Hoeft, and J. B. R. Oonk. The "toothbrush-relic": evidence for a coherent linear 2-Mpc scale shock wave in a massive merging galaxy cluster? *Astronomy and Astrophysics*, 546:A124, October 2012.

R. J. van Weeren, G. Brunetti, M. Brüggen, F. Andrade-Santos, G. A. Ogrean, W. L. Williams, H. J. A. Röttgering, W. A. Dawson, W. R. Forman, F. de Gasperin, M. J. Hardcastle, C. Jones, G. K. Miley, D. A. Rafferty, L. Rudnick, J. Sabater, C. L. Sarazin, T. W. Shimwell, A. Bonafede, P. N. Best, L. Bîrzan, R. Cassano, K. T. Chyży, J. H. Croston, T. J. Dijkema, T. Enßlin, C. Ferrari, G. Heald, M. Hoeft, C. Horellou, M. J. Jarvis, R. P. Kraft, M. Mevius, H. T. Intema, S. S. Murray, E. Orrú, R. Pizzo, S. S. Sridhar, A. Simionescu, A. Stroe, S. van der Tol, and G. J. White. LOFAR, VLA, and Chandra Observations of the Toothbrush Galaxy Cluster. *Astrophysical Journal*, 818:204, February 2016a.

R. J. van Weeren, W. L. Williams, M. J. Hardcastle, T. W. Shimwell, D. A. Rafferty, J. Sabater, G. Heald, S. S. Sridhar, T. J. Dijkema, G. Brunetti, M. Brüggen, F. Andrade-Santos, G. A. Ogrean, H. J. A. Röttgering, W. A. Dawson, W. R. Forman, F. de Gasperin, C. Jones, G. K. Miley, L. Rudnick, C. L. Sarazin, A. Bonafede, P. N. Best, L. Bîrzan, R. Cassano, K. T. Chyży, J. H. Croston, T. Enßlin, C. Ferrari, M. Hoeft, C. Horellou, M. J. Jarvis, R. P. Kraft, M. Mevius, H. T. Intema, S. S. Murray, E. Orrú, R. Pizzo, A. Simionescu, A. Stroe, S. van der Tol, and G. J. White. LOFAR Facet Calibration. *Astrophysical Journal Supplement*, 223:2, March 2016b.

F. Vazza and M. Brüggen. Do radio relics challenge diffusive shock acceleration? *Monthly Notices of the Royal Astronomical Society*, 437:2291–2296, January 2014.

T. Venturi. Observational properties of diffuse radio sources in galaxy clusters . Current knowledge and open questions. *Memorie della Societa Astronomica Italiana*, 82:499, 2011.

A. Vikhlinin, M. Markevitch, and S. S. Murray. A Moving Cold Front in the Intergalactic Medium of A3667. *Astrophysical Journal*, 551:160–171, April 2001.

G. M. Voit. Tracing cosmic evolution with clusters of galaxies. *Reviews of Modern Physics*, 77:207–258, April 2005.

H. J. Völk, F. A. Aharonian, and D. Breitschwerdt. The Nonthermal Energy Content and Gamma-Ray Emission of Starburst Galaxies and Clusters of Galaxies. *Space Science Reviews*, 75:279–297, January 1996.

W. L. Williams, R. J. van Weeren, H. J. A. Röttgering, P. Best, T. J. Dijkema, F. de Gasperin, M. J. Hardcastle, G. Heald, I. Prandoni, J. Sabater, T. W. Shimwell, C. Tasse, I. M. van Bemmel, M. Brüggen, G. Brunetti, J. E. Conway, T. Enßlin, D. Engels, H. Falcke, C. Ferrari, M. Haverkorn, N. Jackson, M. J. Jarvis, A. D. Kapińska, E. K. Mahony, G. K. Miley, L. K. Morabito, R. Morganti, E. Orrú,

E. Retana-Montenegro, S. S. Sridhar, M. C. Toribio, G. J. White, M. W. Wise, and J. T. L. Zwart. LOFAR 150-MHz observations of the Boötes field: Catalogue and Source Counts. *Monthly Notices of the Royal Astronomical Society*, May 2016.

T. L. Wilson, K. Rohlfs, and S. Hüttemeister. *Tools of Radio Astronomy.* 2013.

E. L. Wright. A Cosmology Calculator for the World Wide Web. *Publications of the Astronomical Society of the Pacific*, 118:1711–1715, December 2006.

P.-F. Yan, Q.-R. Yuan, L. Zhang, and X. Zhou. Multicolor Photometry of the Merging Galaxy Cluster A2319: Dynamics and Star Formation Properties. *Astronomical Journal*, 147:106, May 2014.

Z. S. Yuan, J. L. Han, and Z. L. Wen. The Scaling Relations and the Fundamental Plane for Radio Halos and Relics of Galaxy Clusters. *Astrophysical Journal*, 813: 77, November 2015.

F. Zandanel and S. Ando. Constraints on diffuse gamma-ray emission from structure formation processes in the Coma cluster. *Monthly Notices of the Royal Astronomical Society*, 440:663–671, May 2014.

F. Zandanel, C. Pfrommer, and F. Prada. On the physics of radio haloes in galaxy clusters: scaling relations and luminosity functions. *Monthly Notices of the Royal Astronomical Society*, 438:124–144, February 2014.

S. Zaroubi, A. G. de Bruyn, G. Harker, R. M. Thomas, P. Labropolous, V. Jelić, L. V. E. Koopmans, M. A. Brentjens, G. Bernardi, B. Ciardi, S. Daiboo, S. Kazemi, O. Martinez-Rubi, G. Mellema, A. R. Offringa, V. N. Pandey, J. Schaye, V. Veligatla, H. Vedantham, and S. Yatawatta. Imaging neutral hydrogen on large scales during the Epoch of Reionization with LOFAR. *Monthly Notices of the Royal Astronomical Society*, 425:2964–2973, October 2012.

J. A. ZuHone, M. Markevitch, and D. Lee. Sloshing of the Magnetized Cool Gas in the Cores of Galaxy Clusters. *Astrophysical Journal*, 743:16, December 2011.

J. A. ZuHone, M. Markevitch, G. Brunetti, and S. Giacintucci. Turbulence and Radio Mini-halos in the Sloshing Cores of Galaxy Clusters. *Astrophysical Journal*, 762:78, January 2013.

J. A. ZuHone, G. Brunetti, S. Giacintucci, and M. Markevitch. Testing Secondary Models for the Origin of Radio Mini-Halos in Galaxy Clusters. *Astrophysical Journal*, 801:146, March 2015.

Appendix A

LOFAR station layouts

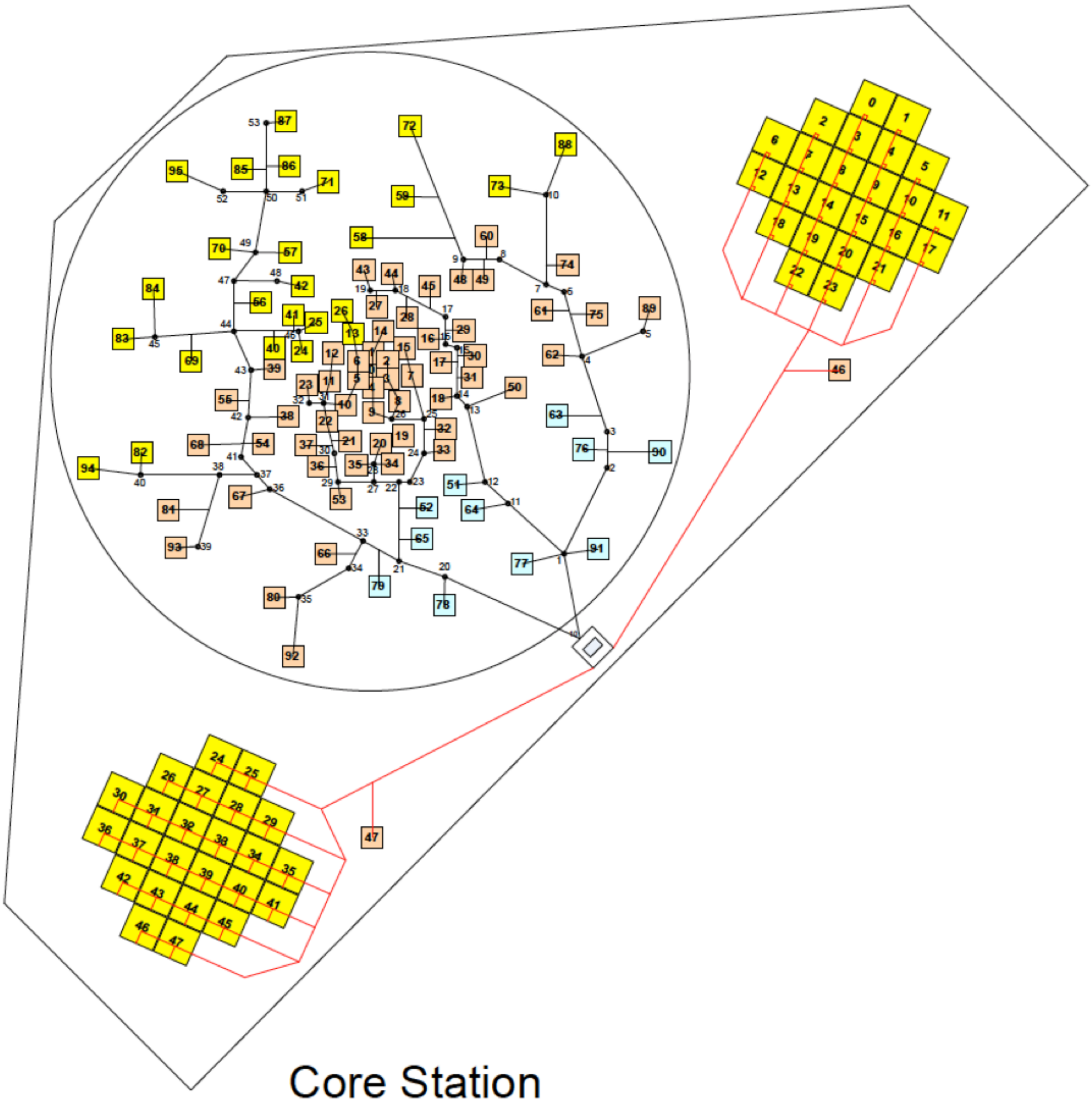

Core Station

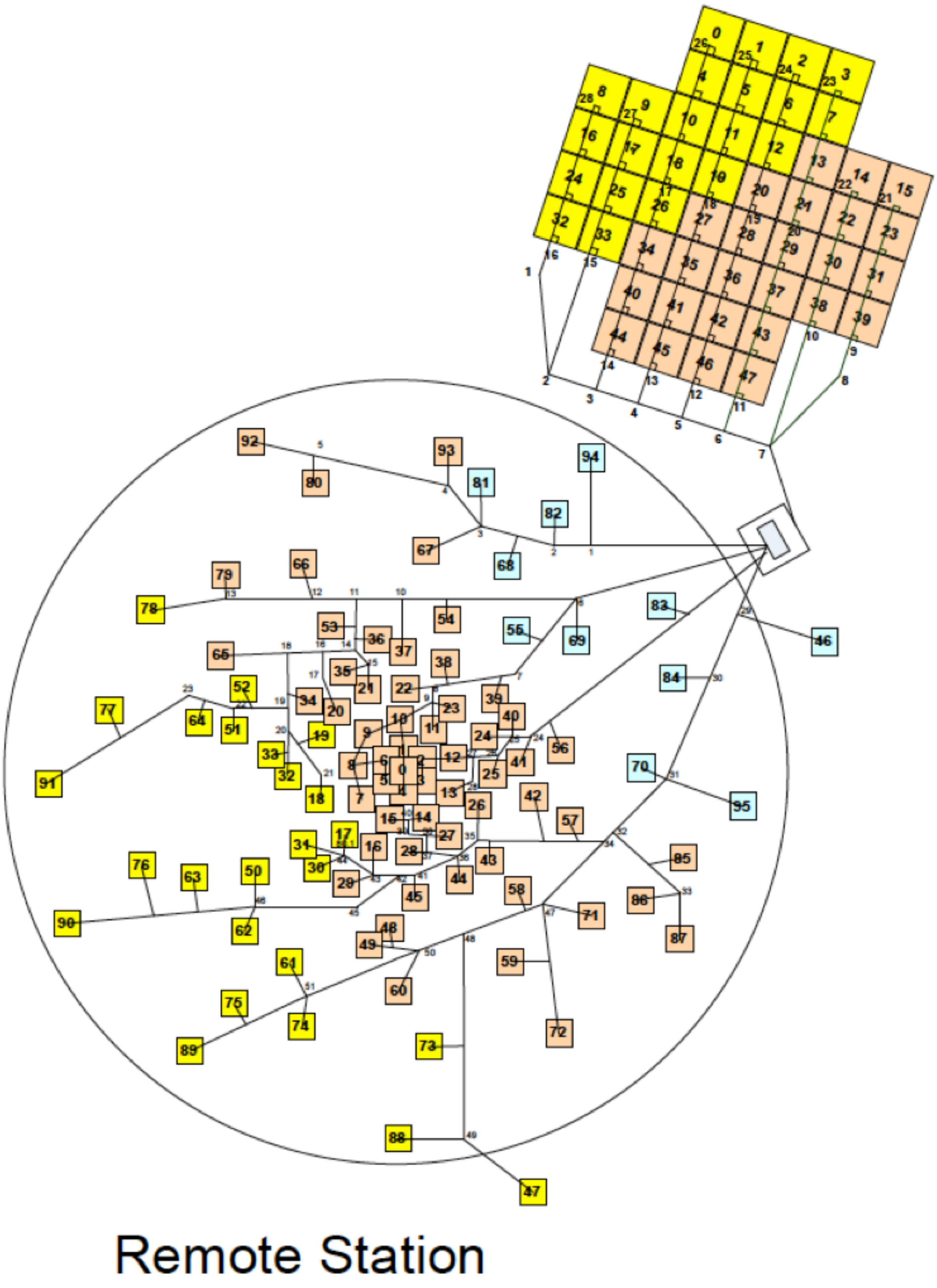
Remote Station

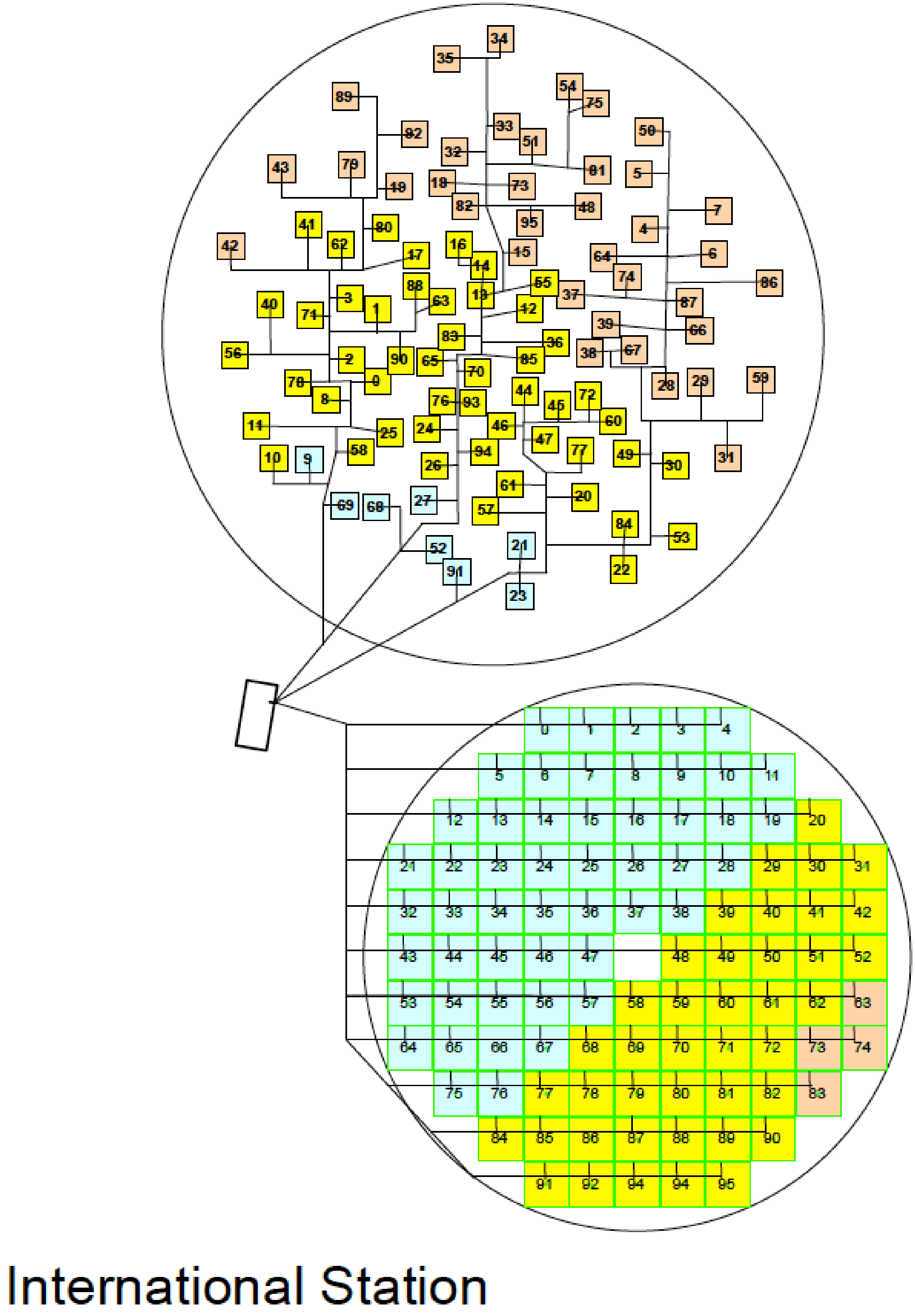
International Station

Appendix B

Calibration matrices

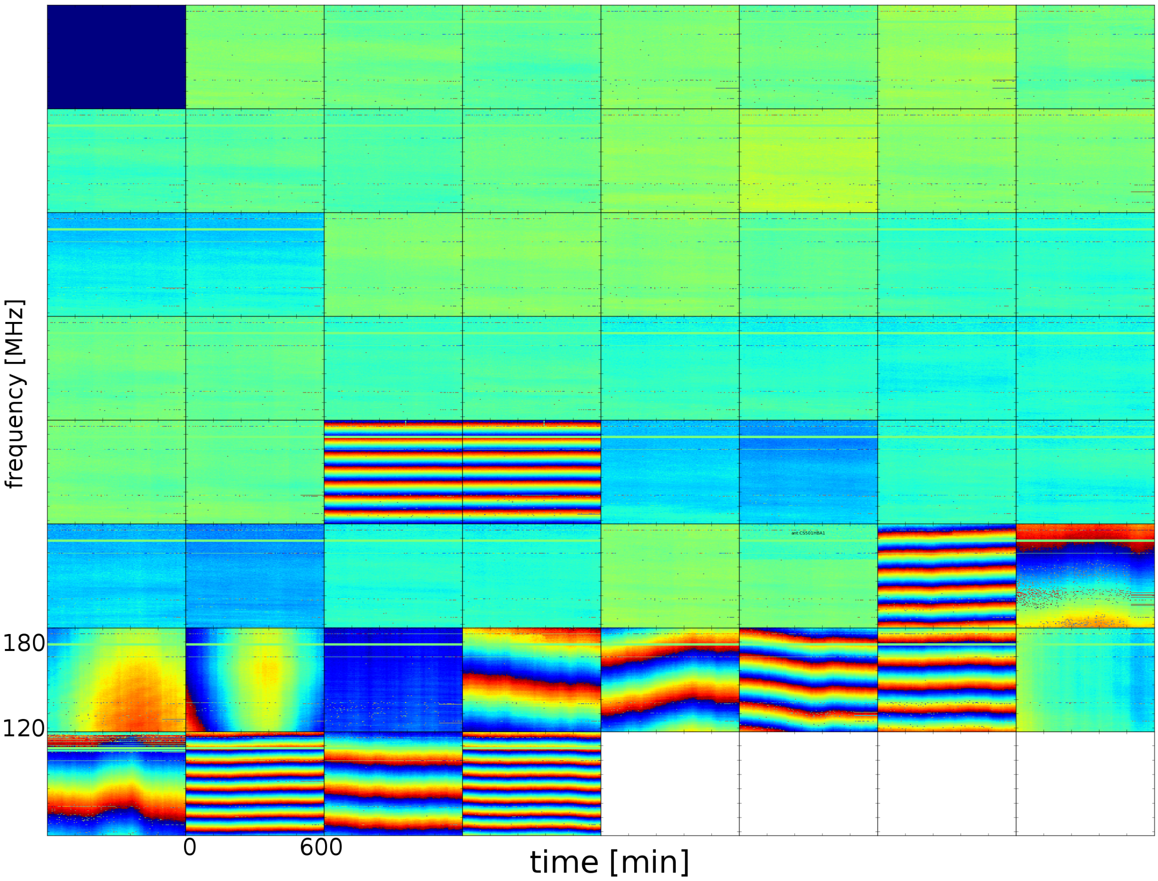

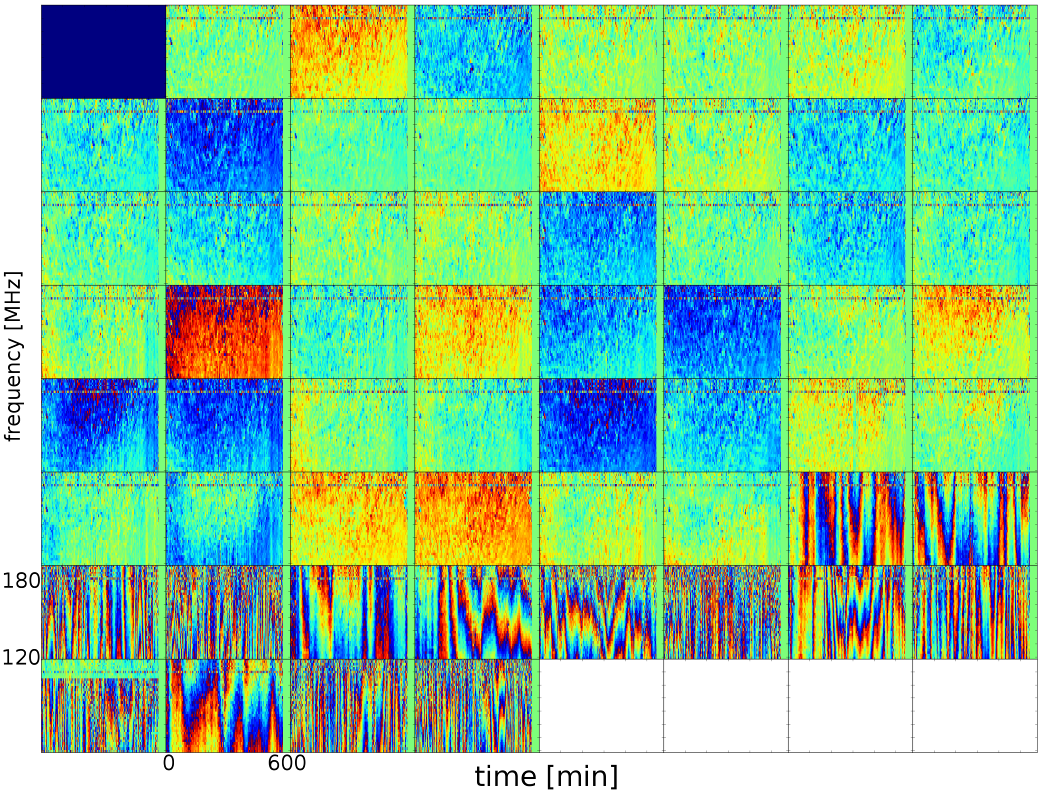

CS001 HBA0	CS001 HBA1	CS002 HBA0	CS002 HBA1	CS003 HBA0	CS003 HBA1	CS004 HBA0	CS004 HBA1
CS005 HBA0	CS005 HBA1	CS006 HBA0	CS006 HBA1	CS007 HBA0	CS007 HBA1	CS011 HBA0	CS011 HBA1
CS017 HBA0	CS017 HBA1	CS021 HBA0	CS021 HBA1	CS024 HBA0	CS024 HBA1	CS026 HBA0	CS026 HBA1
CS028 HBA0	CS028 HBA1	CS030 HBA0	CS030 HBA1	CS031 HBA0	CS031 HBA1	CS032 HBA0	CS032 HBA1
CS101 HBA0	CS101 HBA1	CS103 HBA0	CS103 HBA1	CS201 HBA0	CS201 HBA1	CS301 HBA0	CS301 HBA1
CS302 HBA0	CS302 HBA1	CS401 HBA0	CS401 HBA1	CS501 HBA0	CS501 HBA1	RS106 HBA	RS205 HBA
RS208 HBA	RS210 HBA	RS305 HBA	RS306 HBA	RS307 HBA	RS310 HBA	RS406 HBA	RS407 HBA
RS409 HBA	RS503 HBA	RS508 HBA	RS509 HBA				

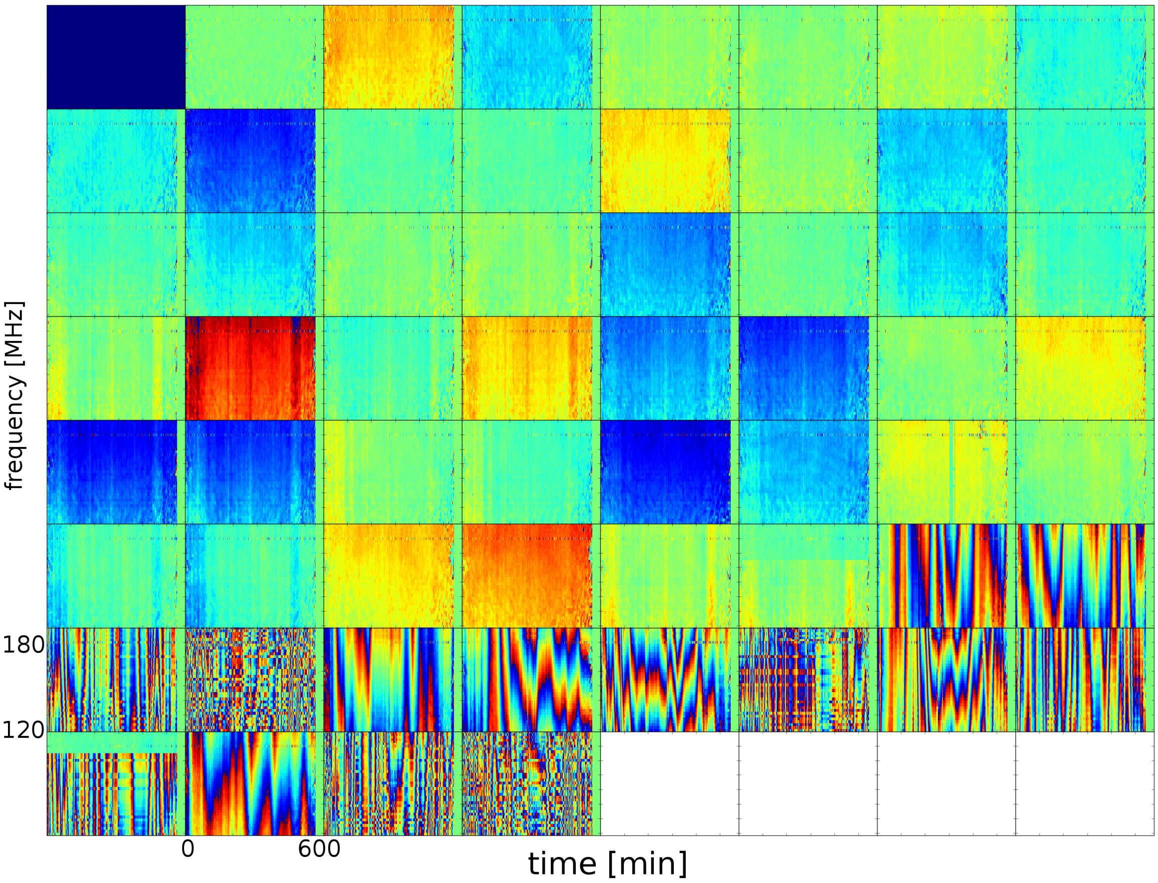

CS001 HBA0	CS001 HBA1	CS002 HBA0	CS002 HBA1	CS003 HBA0	CS003 HBA1	CS004 HBA0	CS004 HBA1
CS005 HBA0	CS005 HBA1	CS006 HBA0	CS006 HBA1	CS007 HBA0	CS007 HBA1	CS011 HBA0	CS011 HBA1
CS017 HBA0	CS017 HBA1	CS021 HBA0	CS021 HBA1	CS024 HBA0	CS024 HBA1	CS026 HBA0	CS026 HBA1
CS028 HBA0	CS028 HBA1	CS030 HBA0	CS030 HBA1	CS031 HBA0	CS031 HBA1	CS032 HBA0	CS032 HBA1
CS101 HBA0	CS101 HBA1	CS103 HBA0	CS103 HBA1	CS201 HBA0	CS201 HBA1	CS301 HBA0	CS301 HBA1
CS302 HBA0	CS302 HBA1	CS401 HBA0	CS401 HBA1	CS501 HBA0	CS501 HBA1	RS106 HBA	RS205 HBA
RS208 HBA	RS210 HBA	RS305 HBA	RS306 HBA	RS307 HBA	RS310 HBA	RS406 HBA	RS407 HBA
RS409 HBA	RS503 HBA	RS508 HBA	RS509 HBA				

Acronyms

ΛCDM Cold Dark Matter. 18

ACIS Advanced CCD Imaging Spectrometer. 20, 47, 99

AGN active galactic nuclei. 2, 5, 12–15, 75, 91, 93, 95–97, 100

BCG brightest cluster galaxy. 5, 48, 50, 55, 57, 67, 71, 73, 87, 91, 93

CALDB Chandra Calibration Database. 42

CASA Common Astronomy Software Applications. 33, 34, 61

CIAO Chandra Interactive Analysis of Observations. 42

CIRS Cluster Infall Regions in the SDSS. 63

CMB cosmic microwave background. 6, 9, 18

COBALT Correlator and Beamforming Application platform for the Lofar Telescope. 29

DSA diffusive shock acceleration. 3, 13, 14, 16, 50, 78

EGRHS Extended GMRT Radio Halo Survey. 8

EoR Epoch of Reionization. 29

factor Facet Calibration for LOFAR. 39, 42

FIRST Faint Images of the Radio Sky at Twenty-Centimeters. 34, 68, 69, 81

FoV field of view. 20, 22, 24, 30, 35–39, 76, 99

FWHM full width at half maximum. 32, 39, 43, 49, 73, 79, 84, 89, 95

GBT Green Bank Telescope. 19, 54, 60, 62, 68, 74, 75, 80, 81

GMRT Giant Metrewave Telescope. 1, 19, 20, 25, 27, 28, 31, 33, 34, 52, 69, 71–75, 87, 91, 96, 97, 99

GSM global sky model. 37, 38

HBA High Band Antennas. 19, 27, 28, 30, 31, 37, 38, 40, 42, 76–79, 82, 84, 88, 91, 95–97, 99, 100

IC Inverse Compton. 6, 9, 14

ICM intracluster medium. 1–7, 9, 10, 13–16, 20, 42, 48, 49, 52, 53, 57, 60, 70, 81, 84, 85, 91, 93, 95, 99, 100, 138

LBA Low Band Antennas. 27–31

LLS largest linear size. 9, 49, 50, 52, 56, 57, 59, 60, 63, 65, 72, 73, 79, 81, 93, 100

LOFAR Low Frequency Array. 7, 19, 20, 27–29, 31, 33–37, 39, 40, 42, 76–79, 81, 82, 84, 88, 91, 95–97, 99, 100

LoS line-of-sight. 9, 35, 48

LoSoTo LOFAR solutions tool. 38

MHD magnetohydrodynamic. 15, 16

NVSS NRAO VLA Sky Survey. 12, 38, 59, 62, 67–69, 74, 80, 81

prefactor LOFAR prefacet calibration pipeline. 38

PSF point spread function. 23, 42

PSPC Position Sensitive Proportional Counter. 80

PSS Digitized Palomar Sky Survey. 68

PyBDSM Python Blob Detection and Source Measurement. 38

RFI radio-frequency interference. 20, 27, 29, 33

RM Rotation Measure. 5

rms root mean square. 34, 48, 74

SDSS Sloan Digital Sky Survey. 63, 70, 82, 91

SKA Square Kilometre Array. 27

SNR signal-to-noise ratio. 34

SZ Sunyaev–Zel'dovich. 55

TEC total electron content. 35, 37, 41

VLA Very Large Array. 1, 8, 34, 48, 50, 56, 57, 59–62, 77

VLBI Very Long Baseline Interferometry. 28

VLSS VLA Low-Frequency Sky Survey. 38, 69

WENSS Westerbork Northern Sky Survey. 38, 50, 54

WSRT Westerbork Synthesis Radio Telescope. 19, 20, 24–27, 31, 33, 34, 45–49, 52, 54, 57, 58, 60–65, 67–69, 71–73, 75, 78, 79, 82, 87, 91, 96, 97, 99, 100

List of Symbols

$*$	convolution, page 23.
$+$	addition, page 14.
$-$	subtraction, page 14.
$=$	is equal to, page 5.
α	spectral index, page 6.
α_{inj}	injection spectral index, page 14.
α_{int}	integrated spectral index, page 14.
$\approx$	approximately, page 6.
$\bar{\cdot}$	complex conjugation, page 23.
β	$\frac{v}{c}$, page 5.
β_{cloud}	cloud velocity, page 13.
$\mathcal{B}$	dirty beam, page 23.
$\mathcal{F}$	Fourier transform, page 22.
$\cdot$	scalar multiplication, page 10.
$\cos$	cosine of, page 20.
ΔI	total error of all flux density measurements, page 34.
Δ_j	distance between the X-ray centroid and the X-ray peak of the jth aperture, page 88.
η	pitch angle between the magnetic field of the ICM and the cosmic ray particle's velocity, page 5.
$\div$	ratio, page 6.
$\frac{dP}{d\nu}$	synchrotron spectrum of a single cosmic ray electron, page 84.
$\frac{P_3}{P_0}$	power ratio, page 88.
γ	Lorentz factor, page 5.
$\gtrsim$	similar greater than, page 14.
$\int$	integral, page 35.
λ	wavelength, page 22.
$\langle\cdot\rangle$	average, page 87.
$\langle\Delta\rangle$	mean distance between the X-ray centroid and the X-ray peak of all apertures, page 88.
$\langle I_{153\,\text{MHz}}\rangle$	averaged flux density at 153 MHz, page 85.
$\langle I_{\text{X}}\rangle$	averaged X-ray flux density, page 85.
$\langle J_{\text{B}}\rangle$	averaged radio emissivity for the mini-halo candidate HB, page 93.
$\langle J_{\text{HA}}\rangle$	averaged radio emissivity for the radio halo HA, page 87.
$\lessapprox$	approximately less than, page 75.
$\lesssim$	similar less than, page 4.
$\ll$	signicifantly less, page 33.

$\mathcal{M}$	Mach number, page 10.
ν	frequency, page 5.
ν_0	frequency in the observer's frame, page 17.
ω_c	critical angular frequency, page 5.
∂	partial derivative, page 35.
ϕ_ion	ionospheric phase rotation, page 35.
Π	degree of linear polarization of synchrotron emission, page 6.
π^0	neutral pion, page 14.
$\pi^\pm$	charged pion, page 14.
$\pm$	plus-minus, page 18.
$\propto$	proportional to, page 4.
ρ_c	critical density, page 18.
$\rightarrow$	reaction, page 14.
σ_rms	rms level of a radio map, page 34.
$\sim$	similar to, page 4.
$\simeq$	similar/equal to, page 87.
$\sin$	sine of, page 5.
$\sqrt{\cdot}$	square root, page 34.
τ	delay, page 36.
τ_clock	clock delay, page 36.
τ_g	geometric delay, page 20.
τ_ion	ionospheric delay, page 35.
τ_i	instrumental delay, page 21.
Θ	angular resolution limit, page 23.
θ	angle between the direction of the receiving signal of an infinitely distant radio source and the normal to the baseline vector, page 20.
θ_max	largest scale an interferometer is sensitive to, page 23.
$\tilde{d}$	transverse size, page 17.
$\tilde{V}_{jk}$	measured visibility, page 33.
$\times$	multiplication, page 30.
ε_0	vacuum permittivity, page 35.
ε_CRe	cosmic-ray electron energy density, page 84.
ε_th	thermal energy density, page 84.
ε_B	magnetic field energy density, page 84.
φ	angle relative to the galaxy cluster's centroid, page 88.
ϑ	measured angular size of an astronomical object, page 17.
$\vec{B}$	magnetic field, page 5.
$\vec{b}$	baseline vector, page 20.
$\vec{s_0}$	phase reference center, page 21.
$\vec{s}$	direction of receiving signal of an infinitely distant radio source, page 20.
$\vec{v}$	velocity of a cosmic ray particle, page 5.
$^\circ$	degrees, page 24.
$''$	arcseconds, page 27.

$'$	arcminutes, page 24.
A_j	primary beam, page 22.
$a_\mathbf{A}$	X-ray semimajor axis of Abell 2069A, page 95.
a_j and b_j	moments of a two-dimensional projected mass distribution, page 88.
B	*uv*-coverage, page 23.
b	exponent of the X-ray to radio surface brightness comparison, page 85.
$b_\mathbf{A}$	X-ray semiminor axis of Abell 2069A, page 95.
b_min	length of the shortest baseline, page 23.
C	concentration parameter, page 88.
c	speed of light, page 5.
c_sound	upstream sound speed, page 10.
D	size of the aperture, page 23.
d	differential of a function, page 5.
D_A	angular size distance, page 18.
D_L	luminosity distance, page 17.
f_inst	average amplitude instability, page 34.
f_scale	flux density scale uncertainty, page 34.
f_subtr	subtraction uncertainty, page 34.
H	hour angle, page 23.
H_0	Hubble constant, page 18.
I	sky brightness distribution, page 21.
I_0	radio peak flux density, page 87.
$I_{153\,\mathrm{MHz}}$	integrated flux density at 153 MHz, page 96.
$I_{322\,\mathrm{MHz}}$	integrated flux density at 322 MHz, page 96.
$I_{346\,\mathrm{MHz}}$	integrated flux density at 346 MHz, page 96.
$I_{608\,\mathrm{MHz}}$	integrated flux density at 608 MHz, page 96.
I_subtr	amount of subtracted flux density, page 34.
J	volume-averaged radio emissivity, page 87.
j_radio	radio emissivity, page 84.
j_X	X-ray volume emissivity, page 4.
J_{jk}	net effect of all modifications of the radio signal, page 33.
j,k	antenna indices, page 22.
k_B	Boltzmann constant, page 84.
L	bolometric luminosity, page 17.
l	length, page 35.
L_{500}	X-ray luminosity integrated up to the radius of 500 times the critical density, page 18.
L_ν	spectral luminosity in the galaxy cluster's frame, page 17.
$L_{\mathrm{X},\mathbf{A}}$	Integrated X-ray luminosity of Abell 2069A, page 95.
$L_{\mathrm{X},\mathbf{B}}$	Integrated X-ray luminosity of Abell 2069B, page 95.
L_X	X-ray luminosity, page 4.
l,m,n	direction cosines, page 22.
m	mass of a cosmic ray particle, page 5.
$M_\odot$	solar mass $= 2 \cdot 10^{30}$ kg, page 3.

m_{e^-}	electron mass, page 35.
N	number of apertures, page 88.
n	number density of cosmic ray electrons, page 5.
N_k	number of frequency channels, page 29.
N_n	number of integration time steps, page 29.
N_{a}	number of stations, page 29.
N_{beams}	number of beams, page 34.
n_{e^-}	electron number density, page 35.
n_{ICM}	particle number density of the ICM, page 4.
N_{pol}	number of polarizations, page 29.
N_V	number of visibilities, page 29.
P	total emitted power, page 6.
p	index of the cosmic ray electron population, page 5.
$P_{1.4}$	radio power at 1.4 GHz, page 75.
P_{IC}	total Inverse Compton power, page 6.
p_{inj}	injection energy spectrum index, page 13.
P_j	two-dimensional projected mass distribution, page 88.
q	elementary charge, page 5.
r	radius, page 88.
$r\left(\tau_{\mathrm{g}}\right)$	response of a two-element interferometer, page 20.
$r_{\mathbf{B}}$	X-ray radius of Abell 2069B, page 95.
R_{ap}	aperture radius, page 88.
r_e	e-folding radius, page 87.
S	X-ray surface brightness, page 88.
$S_{0,\nu}$	spectral flux density in the observer's frame, page 17.
S_0	measured bolometric flux density in the observer's frame, page 17.
S_ν	spectral flux density, page 6.
t	time, page 20.
t_{cool}	radiative coling time, page 4.
T_{e^-}	electron temperature, page 84.
T_{X}	X-ray temperature, page 67.
U_{CMB}	energy density of the CMB, page 6.
u_{min}	u-component of the shortest baseline, page 23.
u,v,w	coordinate system for the baselines of an interferometer, page 22.
v_{shock}	speed of the shock front, page 10.
V_{jk}	visibility, page 21.
W	weighting function, page 32.
w	centroid shift, page 88.
z	redshift, page 4.
%	per cent, page 4.
Ω_Λ	fraction of the total energy density in the Universe in Dark Energy, page 18.
Ω_{m}	fraction of the total energy density in the Universe in matter, page 18.
p^+	proton, page 14.

Index

Ehrenwörtliche Erklärung

Ich erkläre hiermit ehrenwörtlich, dass ich die vorliegende Arbeit selbstständig verfasst und ohne unzulässige Hilfe Dritter oder Benutzung anderer als der angegebenen Hilfsmittel angefertigt habe. Jedwede wörtlich oder sinngemäß übernommenen Ausführungen, Daten und Konzepte sind ausnahmslos unter Angabe der Quellen als solche kenntlich gemacht.

Bei der Auswahl und Auswertung folgenden Materials haben mir die nachstehend aufgeführten Personen in der jeweils beschriebenen Weise unentgeltlich geholfen:

1. Dr. Matthias Hoeft – Betreuung der vorliegenden Arbeit
2. Dr. Roberto Pizzo und Prof. Dr. Uli Klein – Zurverfügungstellung der Daten des WSRT 346 MHz Legacy Surveys
3. Prof. Dr. Marcus Brüggen und Dr. Gianfranco Brunetti – Zurverfügungstellung der Daten der LOFAR HBA Beobachtung von Abell 2069
4. Stefan Fröhlich, Dr. Andreas Horneffer und Dr. David Rafferty – Unterstützung bei der Nutzung der LOFAR-Software zur Kalibration der Daten

Weitere Personen waren an der inhaltlich-materiellen Erstellung der vorliegenden Arbeit nicht beteiligt. Insbesondere habe ich hierfür nicht die entgeltliche Hilfe von Vermittlungs- beziehungsweise Beratungsdiensten (Promotionsberater oder andere Personen) in Anspruch genommen. Niemand hat von mir unmittelbar oder mittelbar geldwerte Leistungen für Arbeiten erhalten, die im Zusammenhang mit dem Inhalt der vorgelegten Dissertation stehen.

Diese Arbeit ist weder im In- noch im Ausland in gleicher noch in ähnlicher Fassung Bestandteil einer anderen Studien- oder Prüfungsleistung.

Die geltende Promotionsordnung der Physikalisch-Astronomischen Fakultät der Friedrich-Schiller-Universität Jena ist mir bekannt.

Ich versichere ehrenwörtlich, dass ich nach bestem Wissen die reine Wahrheit gesagt und nichts verschwiegen habe.

Tautenburg, den 21. Dezember 2016

Alexander Drabent

Lebenslauf

Persönliche Daten:

Name:	Drabent
Vorname:	Alexander
Geburtsdatum:	02. November 1986
Geburtsort:	Leinefelde
Staatsangehörigkeit:	deutsch

Schulausbildung:

1993 – 1997	Staatliche Grundschule II „Albert Schweitzer“, Leinefelde
1997 – 2005	Staatliches Gymnasium „Gottfried-Wilhelm-Leibniz“, Leinefelde
Juni 2005	Abschluss: Allgemeine Hochschulreife (Abitur)

Wehr- oder Ersatzdienstzeiten:

Oktober 2005 – Juni 2006	Zivildienst, „Eichsfeld Klinikum“ Haus St. Vincenz, Heilbad Heiligenstadt

Hochschulstudium:

Oktober 2006 – März 2012	Friedrich-Schiller-Universität Jena Studienrichtung: Physik-Diplom Titel der Diplomarbeit: „Analyse von Flares mit Hilfe von CoRoT-Lichtkurven“ Betreuer: Prof. Dr. Artie Hatzes
Januar 2012	Abschluss: Physik-Diplom
seit April 2012	Doktorand an der Friedrich-Schiller-Universität Jena Titel der Dissertation: „Diffuse Radio Emission at Low Frequencies in Merging Galaxy Clusters“ Betreuer: Prof. Dr. Artie Hatzes

Beruflicher Werdegang:

seit Februar 2012	wissenschaftlicher Mitarbeiter an der Thüringer Landessternwarte Tautenburg

Tautenburg, den 21. Dezember 2016

Alexander Drabent

Publications

[1] **Drabent, A.** and E. W. Guenther. The role of flares for terrestrial planets. In *EPSC-DPS Joint Meeting 2011*, page 433, October 2011

[2] J. Moldon, A. Deller, O. Wucknitz, N. Jackson, **Drabent, A.**, T. D. Carozzi, J. E. Conway, E. Varenius, A. D. Kapinska, J. McKean, L. Morabito, and P. Zarka. The LOFAR long baseline snapshot calibrator survey. In *Proceedings of the 12th European VLBI Network Symposium and Users Meeting (EVN 2014). 7-10 October 2014. Cagliari, Italy*, page 97, 2014

[3] J. Moldón, A. T. Deller, O. Wucknitz, N. Jackson, **Drabent, A.**, T. Carozzi, J. Conway, A. D. Kapińska, J. P. McKean, L. Morabito, E. Varenius, P. Zarka, J. Anderson, A. Asgekar, I. M. Avruch, M. E. Bell, M. J. Bentum, G. Bernardi, P. Best, L. Bîrzan, J. Bregman, F. Breitling, J. W. Broderick, M. Brüggen, H. R. Butcher, D. Carbone, B. Ciardi, F. de Gasperin, E. de Geus, S. Duscha, J. Eislöffel, D. Engels, H. Falcke, R. A. Fallows, R. Fender, C. Ferrari, W. Frieswijk, M. A. Garrett, J. Grießmeier, A. W. Gunst, J. P. Hamaker, T. E. Hassall, G. Heald, M. Hoeft, E. Juette, A. Karastergiou, V. I. Kondratiev, M. Kramer, M. Kuniyoshi, G. Kuper, P. Maat, G. Mann, S. Markoff, R. McFadden, D. McKay-Bukowski, R. Morganti, H. Munk, M. J. Norden, A. R. Offringa, E. Orru, H. Paas, M. Pandey-Pommier, R. Pizzo, A. G. Polatidis, W. Reich, H. Röttgering, A. Rowlinson, A. M. M. Scaife, D. Schwarz, J. Sluman, O. Smirnov, B. W. Stappers, M. Steinmetz, M. Tagger, Y. Tang, C. Tasse, S. Thoudam, M. C. Toribio, R. Vermeulen, C. Vocks, R. J. van Weeren, S. White, M. W. Wise, S. Yatawatta, and A. Zensus. The LOFAR long baseline snapshot calibrator survey. *Astronomy and Astrophysics*, 574:A73, February 2015

[4] **Drabent, A.**, M. Hoeft, R. F. Pizzo, A. Bonafede, R. J. van Weeren, and U. Klein. Diffuse radio emission in the complex merging galaxy cluster Abell 2069. *Astronomy and Astrophysics*, 575:A8, March 2015

[5] C. Dumba, M. Hoeft, **Drabent, A.**, and A. Bonafede. Extended Diffuse Radio Emission in Abell 115. In *The Many Facets of Extragalactic Radio Surveys: Towards New Scientific Challenges*, page 48, October 2015

[6] N. Jackson, A. Tagore, A. Deller, J. Moldón, E. Varenius, L. Morabito, O. Wucknitz, T. Carozzi, J. Conway, **Drabent, A.**, A. Kapinska, E. Orrù, M. Brentjens, R. Blaauw, G. Kuper, J. Sluman, J. Schaap, N. Vermaas, M. Iacobelli, L. Cerrigone, A. Shulevski, S. ter Veen, R. Fallows, R. Pizzo, M. Sipior, J. Anderson,

I. M. Avruch, M. E. Bell, I. van Bemmel, M. J. Bentum, P. Best, A. Bonafede, F. Breitling, J. W. Broderick, W. N. Brouw, M. Brüggen, B. Ciardi, A. Corstanje, F. de Gasperin, E. de Geus, J. Eislöffel, D. Engels, H. Falcke, M. A. Garrett, J. M. Grießmeier, A. W. Gunst, M. P. van Haarlem, G. Heald, M. Hoeft, J. Hörandel, A. Horneffer, H. Intema, E. Juette, M. Kuniyoshi, J. van Leeuwen, G. M. Loose, P. Maat, R. McFadden, D. McKay-Bukowski, J. P. McKean, D. D. Mulcahy, H. Munk, M. Pandey-Pommier, A. G. Polatidis, W. Reich, H. J. A. Röttgering, A. Rowlinson, A. M. M. Scaife, D. J. Schwarz, M. Steinmetz, J. Swinbank, S. Thoudam, M. C. Toribio, R. Vermeulen, C. Vocks, R. J. van Weeren, M. W. Wise, S. Yatawatta, and P. Zarka. LBCS: The LOFAR Long-Baseline Calibrator Survey. *Astronomy and Astrophysics*, 595:A86, November 2016

[7] T. W. Shimwell, H. J. A. Röttgering, P. N. Best, W. L. Williams, T. J. Dijkema, F. de Gasperin, M. J. Hardcastle, G. H. Heald, D. N. Hoang, A. Horneffer, H. Intema, E. K. Mahony, S. Mandal, A. P. Mechev, L. Morabito, J. B. R. Oonk, D. Rafferty, E. Retana-Montenegro, J. Sabater, C. Tasse, R. J. van Weeren, M. Brüggen, G. Brunetti, K. T. Chyży, J. E. Conway, M. Haverkorn, N. Jackson, M. J. Jarvis, J. P. McKean, G. K. Miley, R. Morganti, G. J. White, M. W. Wise, I. M. van Bemmel, R. Beck, M. Brienza, A. Bonafede, G. Calistro Rivera, R. Cassano, A. O. Clarke, D. Cseh, A. Deller, **Drabent, A.**, W. van Driel, D. Engels, H. Falcke, C. Ferrari, S. Fröhlich, M. A. Garrett, J. J. Harwood, V. Heesen, M. Hoeft, C. Horellou, F. P. Israel, A. D. Kapińska, M. Kunert-Bajraszewska, D. J. McKay, N. R. Mohan, E. Orrú, R. F. Pizzo, I. Prandoni, D. J. Schwarz, A. Shulevski, M. Sipior, D. J. B. Smith, S. S. Sridhar, M. Steinmetz, A. Stroe, E. Varenius, P. P. van der Werf, J. A. Zensus, and J. T. L. Zwart. The LOFAR Two-metre Sky Survey - I. Survey Description and Preliminary Data Release. *ArXiv e-prints*, November 2016

[8] C. P. Coughlan, R. E. Ainsworth, J. Eislöffel, M. Hoeft, **Drabent, A.**, A. M. M. Scaife, T. P. Ray, M. E. Bell, J. W. Broderick, S. Corbel, J.-M. Greißmeier, A. J. van der Horst, J. van Leeuwen, S. Markoff, M. Pietka, A. J. Stewart, R. A. M. J. Wijers, and P. Zarka. A LOFAR detection of the low mass young star T Tau at 149 MHz. *ArXiv e-prints*, November 2016

Talks

2013

- Clock/TEC separation on long baselines. *Imaging the Low Frequency Sky with LOFAR*, Leiden (The Netherlands), January 2013

- Clock/TEC separation on long baselines. *LOFAR Magnetism KSP meeting*, Sant'Antioco (Sardinia), May 2013

- WSRT 350 MHz Legacy Survey: Clusters. *Annual Meeting of the DFG Research Unit 1254*, Rügheim, September 2013

2014

- Diffuse radio emission in the complex merging galaxy cluster Abell 2069. *Annual Meeting of the DFG Research Unit 1254*, Forschungszentrum Jülich, November 2014

- Status and efforts for calibrating and using long baselines. *Annual Meeting of the DFG Research Unit 1254*, Forschungszentrum Jülich, November 2014

- Diffuse radio emission in the complex merging galaxy cluster Abell 2069. *Instituts-Kolloquium*, Thüringer Landessternwarte Tautenburg, September 2014

2015

- Investigating diffuse radio emission with LOFAR: The complex merging galaxy cluster Abell 2069. *LOFAR Community Science Workshop*, Assen (The Netherlands), June 2015

- Investigating diffuse radio emission with LOFAR: The complex merging galaxy cluster Abell 2069. *Annual Meeting of the DFG Research Unit 1254*, Schloss Ringberg, July 2015

- Investigating diffuse radio emission with LOFAR: The complex merging galaxy cluster Abell 2069. *LOFAR Surveys KSP Meeting*, Leiden (The Netherlands), September 2015

2016

- Investigating diffuse radio emission with LOFAR: The complex merging galaxy cluster Abell 2069. *Clusters Meeting 2016*, Hamburg-Bergedorf, March 2015
- Investigating diffuse radio emission with LOFAR: The complex merging galaxy cluster Abell 2069. *LOFAR Community Science Workshop*, Zandvoort aan Zee (The Netherlands), April 2016
- The LOFAR view on the merging galaxy cluster Abell 2069. *LOFAR Surveys KSP Meeting*, Bologna (Italy), September 2016
- The LOFAR view on the merging galaxy cluster Abell 2069. *Annual Meeting of the DFG Research Unit 1254*, Berlin-Dahlem, September 2016
- Status and efforts for calibrating LOFAR LBA. *GLOW Annual Assembly 2016*, Leibniz-Institut für Astrophysik Potsdam, December 2016